2019

# Modeling Electrospun Fibrous Materials

Sina Hassanpouryousefi
*Virginia Commonwealth University*

# Modeling Electrospun Fibrous Materials

A dissertation submitted in partial fulfillment of the requirements for the degree of Doctor of Philosophy at Virginia Commonwealth University

By

Sina Hassanpouryousefi

M.Sc. Mechanical Engineering, Iran University of Science and Technology, Tehran, Iran, 2015

Director: Hooman V. Tafreshi

Professor, Department of Mechanical and Nuclear Engineering

Virginia Commonwealth University

Richmond, Virginia

December, 2019

## Dedication

I would like to dedicate this work to my mother, Mahtab and my Father, Alireza and to my beautiful sister Sara who through the thick and thin, have been there for me. Their encouragement and drive is what has made me who I am. I could not have come this far without their unconditional support.

## Acknowledgment

I wish to express my sincere thanks to Prof. Hooman V. Tafreshi, my advisor, for his continuous support, valuable guidance and encouragement throughout the course of my research. I would not have been able to finish this work without his support and unfailing faith in me.

I would like to extend my feeling of gratitude to the other members of my Ph.D. committee, Prof. Gary C. Tepper, Prof. Daren Chen, Prof. Christina Tang and Prof. Rebecca Segal for their insightful questions, valuable suggestions and comments which have helped strengthen my work.

I am thankful to my friends and my labmates for making my life in VCU and Richmond memorable. I will always be grateful to Shahla Pishdad and my relatives for their support in US.

I would like to express my gratitude to my family for their endless support. I am thankful to my parents (Mahtab and Alireza), and my sibling (Sara) and my close friends for always supporting me and encouraging me to follow my dreams.

I would also like to thank the Nonwovens Institute at NC State University and VCU School of Engineering for financial support.

# Table of Contents

## List of Figures

# Abstract


Modeling Electrospun Fibrous Materials

By Sina Hassanpouryousefi, Ph.D.

A dissertation submitted in partial fulfillment of the requirements for the degree of Doctor of Philosophy at Virginia Commonwealth University.

Virginia Commonwealth University, 2019

Director: Hooman V. Tafreshi

Professor, Department of Mechanical and Nuclear Engineering

Electrospinning has been the focus of countless studies for the past decades for applications, including but not limited to, filtration, tissue engineering, and catalysis. Electrospinning is a one-step process for producing nano- and/or micro-fibrous materials with diameters ranging typically from 50 to 5000 nm. The simulation algorithm presented here is based on a novel mass-spring-damper (MSD) approach devised to incorporate the mechanical properties of the fibers in predicting the formation and morphology of the electrospun fibers as they travel from the needle toward the collector, and as they deposit on the substrate. This work is the first to develop a physics-based (in contrast to the previously-developed geometry-based) computational model to generate 3-D virtual geometries that realistically resemble the microstructure of an electrospun

fibrous material with embedded particles, and to report on the filtration performance of the resulting composite media.

In addition, this work presents a detailed analysis on the effects of electrospinning conditions on the microstructural properties (i.e. fiber diameter, thickness, and porosity) of polystyrene and polycaprolactone fibrous materials. For instance, it was observed that porosity of a PS electrospun material increases with increasing the needle-to-collector distance, or reducing the concentration of PS solution. The computational tool developed in this work allows one to study the effects of electrospinning parameters such as voltage, needle-to-collector distance (NCD), or polymer concentration, on thickness and porosity of the resulting fibrous materials. Using our MSD formulations, a new approach is also developed to model formation and growth of dust-cakes comprised of non-overlapping non-spherical particles, for the first time. This new simulation approach can be used to study the morphology of a dust-cake and how it impacts, for instance, the filtration efficiency of a dust-loaded filter, among many other applications.

# Chapter 1. Introduction

## 1.1 Background Information

Electrospinning has been acknowledged as the most versatile and effective technique to fabricate fibers and beads with controllable morphologies, structures and functional components. Interestingly, it is an easy to setup process and hard to predict known as electrospinning. The process of electrospinning produces continuous fibers from the submicron diameter down to the nanometer diameter. It has been the focus of countless experimental and computational studies for the past decades for applications, including but not limited to, tissue engineering [1,2], filtration [3-6], catalysis [7], superhydrophobic surfaces [8-10], drug delivery system [11,12], sensors [13,14]. Characterizing the electrospun product is difficult as the materials is thin and compliant and its crucially important for product designing and development. Here, we have focused on creating 3-D nonwoven structures and predicting the electrospinning process as function of its process [15,16]. In the following subsections the background information about electrospinning process, bead formation, and mat generation of fibrous materials were presented.

## 1.2 Electrospinning: General Overview

Electrospinning is a simple and low-cost method for producing electrospun mats. It is a one-step process for producing submicron fibers [15,16]. Electrospun membranes have some important properties, including a large specific surface area, light weight, small pore size, and high porosity [17]. So, they have great potential applications, such as in air or water filters [18,19], sensors [13,14,20], scaffolds [21], separation membranes [22-24], and protective textiles [25]. Diameter

of the fibers produced via electrospinning typically range from 50 to 5000 nm (one or two orders of magnitude smaller than those of traditional textile fibers [26, 27]). In a typical electrospinning process, a liquid jet (a single thread of fiber/filament) is ejected from the surface of a charged polymer solution (or melt) and then driven by the electrical forces towards a collector (the high voltage differences) [15, 28-31]. The technique is based on the electrostatic force that acts on the polymeric solution. The recent work started to study the effect of alternating (AC) electric field on static and dynamic properties of other liquids [32]. The charged polymer jet flow travels linearly for a short distance before starting bending, which leads to form the increasing instabilities circular loop that is called the whipping process [33-36]. However, during the electrospinning process the liquid jet shows unstable behavior. This behavior causes the random formation of nanofibers. It involves stretching a polymer fluid under a strong electric field into fine filaments, and subsequently solidifying them to form dry or semidry fibers, which finally deposit on the electrode collector forming a nonwoven fiber mat in the most cases [37]. When the jet flow reaches collector, fibers start to deposit on the collector and after while it forms an electrospun mat with a final diameter significantly reduced from the initial one [38]. The diameter of the spiral trajectories is in the range of a few microns up to a few centimeters. The important reason of the instabilities in the filament are the effects of electrostatic repulsions of the charges in the filament and the columbic forces caused by the electric field [28-31, 37]. The electric charges in the filament may be degenerated in the ambient air due to humidity or air motion or other factors during the electrospinning process. However, depending on the polymer structure and the process conditions, it is also possible that some charges remain in the fibers after the fibers are deposited on the collector. These remain charges neglected in fiber droplet detachment simulations [39,40].

Theron et al. 2004 reported the experimental work on the electrospinning process in which the influence of different process parameters on the electric current and volume and surface charge density in the different solutions of polyethylene oxide (PEO), polyacrylic acid (PAA), polyvinyl alcohol (PVA), polyurethane (PU) and polycaprolactone (PCL) jet was measured [41]. Also Theron et al. 2005 described the results of the experimental investigation and modeling of multiple jets during the electrospinning of polymer solutions [42]. It has been demonstrated experimentally and with the help of numerical simulations that the mutual Columbic interactions influence the paths of individual electrified jets in electrospinning.

The fiber's bending instabilities during the electrospinning process produced the straight and curly fibers in the resulting electrospun mat. The bending instabilities occurring during electrospinning were studied and mathematically modeled by Reneker et al. 2000 by viscoelastic point masses connected together. The viscoelasticity of the spinning polymer and solvent evaporation effects on jet flow movement were discussed in the Maxwell model [33, 34]. The most common linear viscoelastic models are the Maxwell model, in which springs and dampers are connected in series (the springs and dampers resemble the material's elasticity and viscosity), which is more suited for a fiber in the liquid/melt state. This model considers the total forces are taken into on each bead consists of a viscoelastic force, an electric force, a Coulomb force and a surface tension force. As well as this, the effect of evaporation during spinning is considered. Although, it may not accurately design and control the electrospinning process because of difficulty in measuring model variables.

Based on the model originally introduced by Reneker and Yarin [33], Lauricella et al. developed JETSPIN code to simulate the electrospinning process of nanofibers with delivering a discrete element model [43]. Dynamic mesh refinement was applied to address the low resolution problems in discrete elements methods [44]. The air drag force added to Newton's equation to study its effect on bending instabilities of jet path [45]. Effects of particles and external rotating electric field on the whipping instabilities studied to have a better control on the morphology of the resulting electrospun fiber [46, 47]. In their work, the reason of reduction in jet flow radius is stretching process, they have a consequent decrease of the filament radius as a result of the volume conservation. They didn't consider the effect of evaporation and mass reduction on charge, elasticity and diameter of jet flow as presented in [34, 48]. Borzacchiello et al. 2016 described the fluid rheology using Giesekus model to predict the polymer properties accurately [49]. Simko et al. 2016 developed the mathematical model to describe the electrospinning process of poly(ethylene oxide) PEO and predict the deposition direction of electrospun nanofibers as a function of flow rate, viscosity, relaxation time and electrical potential [50]. Gadkari 2018 considered the jet as a charged continuum to study the polymer relaxation time to obtain bead free uniform fibers [51]. In this model, the jet travels in a straight line from the needle tip to the collector plate and this work can't predict whipping. Pontrelli et al. 2014 develop an analytical bead-spring model to investigate the role of non-linear rheology on the dynamics of electrified jets in the early stage of the electrospinning process [52]. The elongation of the charged jet filament is significantly reduced in the presence of a non-zero yield stress. Lauricella et al. 2015 investigated the effects of dissipative air drag on the dynamics of electrified jets in the initial stage of the electrospinning process [53]. The main idea is to use a Brownian noise to model air drag effects on the uniaxial elongation of the jets.

The described mathematical model in [33,34] of electrospinning process helps to predict the deposition direction of electrospun nanofibers as a function of flow rate, viscosity, relaxation time and electrical potential. Thompson et al. 2007 determined the effects of 13 material and operating parameters on electrospun fiber diameters by varying the parameter values in an electrospinning theoretical model [48]. The important parameters in the morphology of electrospun polymer fibers are concentration, applied voltage, and solvent properties. Higher concentrations of the polymer solution form thicker fibers and fewer beads. The fiber morphology under different solvent mixture ratios and solvent mixtures has also been studied [54]. Therefore, the current work is devised to obtain the jet flow properties like deposition velocity and fiber diameter at the moment it touches collector in the consideration of solvent evaporation. In our work, we presented instabilities of jet flow to simulate the realistic jet flow and the jet flow properties to use in mat generation code.

### 1.3 Bead Formation

The fabricated mats have been widely applied in various applications, including in tissue engineering and filtration industry [3, 55-62]. Mats that are fabricated by electrospinning have various morphologies that include pure fibers and beaded fibers [63,64]. Changing the morphology from pure fiber to beaded fibers has involved altering and controlling the polymer concentration in the precursor solution, which does affect the produced electrospun mat [38, 63-65]. The viscoelasticity of the solution, charge density carried by the jet, and the surface tension of the solution are the key factors that influence the formation of the beaded fibers. Several theoretical models have been used to explain the formation of beads on a string structure in viscoelastic filaments [66, 67].

Electrospun mats often have beads in regular arrangements [68, 69]. Specifications of electrospun fibers, such as morphology and size can be controlled by electrospinning condition including polymer concentration, applied voltage, polymer flow rate, and needle tip-to-collector distance [70, 71]. A number of publications have been reported on the effect of electrospinning conditions on the resulting fiber morphology. However, comprehensive studies on the development of various morphologies of electrospun mat and introducing different conditions have rarely been reported. Interestingly, apart from fibers with a broad range of diameters and made of different polymeric materials, the electrospinning method allows one also, for specific experimental conditions, to obtain other polymer structures like the beaded (microsphere on mat) morphology [68, 69, 72-74]. It is well known that polymer concentration is one of the most important parameters in the fabrication and morphology of nanofibers in electrospinning process. When the polymer concentration is low, many microspheres appeared in electrospun products, and the process became electrospraying.

The morphology of electrospun polymer ranges from particles (electrospray [75-77]) to pure fibers (electrospinning), depending on various conditions. Electrospinning and electrospraying processes were tested as tools for the production of nonwoven nanocomposite fabric from a polymer material with nanoparticles deposited on a fiber surface or collector [78,79].

### 1.4 Mat Generation: General Overview

To date, there is no accurate method for measuring the thickness, and consequently the porosity of a nanofiber mat (see e.g., [80]). Characterizing the morphological structure of the electrospun mat

accurately is important, when such layers are applied to filters, barrier fabrics, and fluid absorbent media as well as many others [1-14]. Obviously, one cannot know the performance of a nanofiber mat without knowing its properties such as thickness and porosity. The morphological structure models have been widely applied to simulate the application process, such as in the prediction of the specific permeability [81], filtration efficiency [82], and thermal conductivity [83]. Simulations of electrospun mat in the application process have focused on filtration [84,85]. Most of electrospun models focus on the electrospinning processes, such as the distribution of charges in liquid-jet models [86], the stability of the jet model [33,34], and the multiple-jet model [35,42]. However, little literature is available on the modeling of the morphological structure of electrospun mats. Samaha et al. [87] developed a novel experimental method to estimate the thickness and gas volume fraction of superhydrophobic coatings that known as buoyancy method. The buoyancy method is a new technique that allows one to estimate the thickness of a non-wetting porous material by submerging it. However, for mats that are not superhydrophobic, one has to find another way or to use another fluid instead of water. Zundel et al. 2017 presented a discrete random network modelling approach specific to electrospun networks [88]. Feng et al. 2017 proposed a model for the morphological structure of electrospun membranes, it was different from the random distribution of fibers in a nonwoven [89]. The 3-D structure of nonwovens produced with number of layers, and each layer is made up of a network of random fibers. The model can be divided into two categories: two-dimensional (2-D) simulation and three-dimensional (3-D) simulation. For 2-D simulation, Monte Carlo simulation is a widely used method [90,91], and the fiber orientation follows free path randomness (m randomness), which is suitable for generating a nonwoven with continuous fibers [92,93]. 3-D simulations are often based on 2-D simulations. In a recent study by Choong et al. 2015 [94] used a laser scanning microscopy with fluorescent markers to collect

3-D digitized images of electrospun fiber mars, and they reconstructed a 3-D structure of an electrospun mat. In these models, only partial areas of the mat where the fibers could be viewed in a random distribution were observed, but the distribution of the fibers in the whole mat was not researched. Recently our group has developed a viscoelasticity model (mass-spring-damper model) to simulate 3-D structure of electrospun material and thereby predict their thickness [95,96]. In this model, fibers implemented as arrays of beads connected with springs and dampers, and is therefore capable of realistically simulate curvature of the fibers at fiber–fiber crossovers without allowing the fibers to penetrate into one another–a major advantage over the previous fiber-mat generation methods [97-104]. Also this mass-spring-damper simulation could be used in fiber-droplet detachment simulation [105, 106] as a most realistic simulation of fiber to validate the detachment experiment results [107,108].

The proposed mass-spring-damper (MSD) method has the capability to simulate 3-D structure of the pure fibers (electrospinning) to spherical (electrospraying) and non-spherical particles (dust packing [109,110]), depending on various conditions. Therefore, an additional level of structural complexity can be introduced into the structure by the production of small pure monodisperse particles when a colloidal suspension of solid nanoparticles or a solution of a material is sprayed [111,112]. The produced structure is porous, with the nanoparticles deposited on them increasing the total surface area when the microsphere is deposited [79]. Simultaneous electrospinning and electrospraying (SEE) may be used to incorporate functional nanoparticles on the surface of the nanofibers within the membrane. SEE method leads to self-dispersion of nanoparticles in nanofiber membrane and the nanoparticles can attach to the surface of nanofibers [78,79].

### 1.5 Overall Objectives of This Thesis

Main objective of this dissertation is to develop a computational model to characterize the fibrous structure resulted from electrospinning. The main contribution of this work is to understand the mechanical properties of filter media and electrospun mat that can be obtained through electrospinning process. Computational models are developed to predict the mechanical properties of 3-D porous structure as a function of production parameters and several experiments are performed to validate computational results. Another objective is to study the dust formation of non-spherical particles for first time.

First, the electrospinning process for different polymer is investigated to predict the jet flow movement and changes. Most of the previous studies on electrospinning process were focused on predicting the trajectory of the electrospinning jet flow. Less attention was paid to the effect of electrospinning condition and polymer properties on the deposited fiber's properties (like fiber diameter and deposition velocity). An experimental study helps us to validate or simulations better understanding of electrospinnig and produced electrospun mat to characterize. This information is crucially important for simulate the fibrous structure. The ultimate goal of the present work is to develop a computer program for predicting the electrospinning process and its filter media used in fluid-air or fluid-fluid separation, filtration.

Despite the widespread applications of electrospun fibers, accurate thickness measurement of an electrospun fiber mat is still difficult as the materials is thin and compliant. Chapter 2 discusses a modeling approach to help better understand this problem. This work presents an algorithm that includes straight fibers in morphology simulation is developed for the first time, to create virtual

3-D fibrous structures that resemble the micro-geometry of an electrospun fiber mat (see Chapter 2). The algorithm is based on treating a fiber as an array of beads interconnected with springs and dampers, and is particularly designed to simulate the bending of the fibers at fiber-fiber crossovers (important for predicting the thickness and porosity of a nanofiber mat). An in-house C++ computer program is developed for this algorithm and is used to study the effects of fiber mechanical properties on the thickness and porosity of electrospun mats. An additional Python computer program is developed to simulate fiber formation in electrospinning, and more importantly, obtain the deposited fiber properties as an input of mat generation C++ code. It also worth mentioning that two different experimental methods have been considered to calibrate our simulation results in our thickness measurements for polystyrene mats (hydrophobic mats), the buoyancy method and micrometer measurements. The uniqueness of this work lies on its ability to obtain relationships between the thickness (and porosity) of electrospun mat and the properties of its constituting fibers and its electrospinning process. The electrospun mat properties were shown to depend on deposited fiber, which varies depending on polymer properties and electrospinning conditions.

Chapter 3 presents a detailed investigation on the 3-D structure of electrospun mat that are made of curly fibers and the mechanical properties of simulated mat as a function of electrospinning process. These effects are predicted computationally via numerical simulation and validated with electrospinning experiments. Special attention is paid to formation of curly fibers in polycaprolactone (PCL) electrospinning and its fiber fiber-fiber bending and deflection which the viscoelastic properties of fibers were obtained based on experimental data reported literature for the single-fiber properties. This work also discusses the effects of electrospinning variables on the

size and velocity of the deposited fibers of PCL and its effects on the mechanical properties of fibrous nonwoven structure like thickness and porosity and presents a mathematical expression to predict the fate of that polymer.

The fibrous structure in the presents of spacer particle is discussed in Chapter 4. 3-D structure of fibrous structure comprised of number of fibers and particles are studied in terms of their portion and size to characterize the simulated structure and its filtration efficiency. The effects of microparticles properties on the simulated structure are investigated via numerical simulation. More specifically, the work presented here is the first to report the effects of spacer particles with different diameters or basis weights on the thickness and solid volume fraction of spacer-embedded fibrous media. Our numerical simulations conducted using our in house C++ computer program. Interestingly, our results indicate that adding spacer particles to a fibrous filter can lower its collection efficiency and pressure drop, but the reduction in the pressure drop will be at a higher rate resulting in better filters, i.e., filters with better quality factors.

The idea of simulating the dust growth comprised of non-spherical particles is presented in Chapter 5. A computational simulation of different shape presented to effectively characterize the morphology of dust growth for different properties and shape. More specifically, this study proposed a new approach for mass-spring-damper method (MSD) to model 3-D non-spherical particles. Different shapes with 3 different aspect ratio are modelled to investigate the effects of particle shape, size and packing on porosity and thickness of packed dust. This was accomplished by using the developed our C++ computer program. The simulation results prove this point that the symmetric particles (like sphere, cube and short fibers) with the small size and aspect ratio

have the highest solid volume fraction (packing density) for a constant basis weight in comparison with other non-spherical long leg particle. Finally, the overall conclusions of this thesis are presented in chapter 6.

# Chapter 2. Effects of Electrospinning Conditions on Microstructural Properties of Polystyrene Fibrous Materials

## 2.1 Introduction

Electrospinning is a popular method for producing fine fibers ranging from about 0.05 μm to about 10 μm in diameter, and it has been the focus of countless studies for the past decades for applications, including but not limited to, tissue engineering [1,2], filtration [3-6], catalysis [7], self-cleaning [112-114], drug delivery [12,13], and sensor manufacturing [14,15]. While it is quite easy to setup an electrospinning unit, it is very difficult to predict the outcomes of an electrospinning experiment in terms of fiber diameter, mat thickness, or mat porosity. This is due mainly to the complicated physics of fiber formation in electrospinning, and also the minuteness of the resulting fibers [38,39,80,115,116]. For instance, there is no accurate method of measuring the thickness, and consequently the porosity, of an electrospun fiber mat. This is because such mats are generally very thin, and at the same time, very soft (tend to deform during measurement) (see e.g., [80,116]). Regarding this concern, our group has recently developed a mass-spring-damper (MSD) model to simulate the morphology of electrospun materials and thereby predict their thickness and porosity [95]. This model treats the fibers as arrays of beads connected to one another with springs and dampers, and is therefore capable of realistically modeling the mechanical interactions between the fibers during mat formation. More importantly, our MSD model can realistically simulate curvature of the fibers at fiber–fiber crossovers without allowing the fibers to penetrate into one another—a major advantage over the previous fiber-mat generation methods [88,89,97-104,117-122]. Obviously, for the fiber-to-fiber interactions to be accurate, the

MSD model requires material-dependent values for the stiffness of the springs and dampers that are used to simulate the rigidity of the fibers. Such fiber-level information is not always available, and therefore as will be discussed later in this chapter, we calibrated our MSD model using experimental data obtained from electrospinning polystyrene (PS) mats. In addition, our MSD mat generation algorithm requires fiber diameter and fiber deposition velocity as inputs. These factors are both process- and polymer-dependent parameters, i.e., they vary with electrospinning parameters such as voltage, needle-to-collector distance (NCD), and solution concentration among many others. To overcome this limitation and improve the usability of the MSD model as a design or characterization tool for electrospinning, we have coupled the electrospinning filament formation model of Refs. 33 and 34 with our MSD model in the current study. The pioneering mathematical formulations developed Refs. 33 and 34 allows one to simulate the formation of a filament in an electrospinning process starting from the needle all the way to the collector. This allows us to obtain the necessary input values for the MSD mat generation model, and thereby relate the properties of an electrospun mat to the electrospinning conditions, for the first time.

The remainder of this chapter is organized as follows. Section 2.2 presents a brief overview of our experimental setup for producing electrospun PS mats. A condensed summary of the electrospinning model of Refs. 33 and 34 is then given in Section 2.3 followed by our mat generation model in Section 2.4. The computational and experimental results obtained for electrospinning PS are presented and discussed in Section 2.5. Conclusions drawn from our study are given in Section 2.6.

## 2.2 Experiment

PS pellets (average molecular weight 350,000 purchased from Aldrich, MO) were dissolved in a THF (HPLC grade) or Toluene (ACS grade) mixture with Acetone (ACS grade) with a 70 to 30 weight fraction (solvents were purchased from Fisher Scientific, Fair Lawn, NJ). Solutions were stirred at room temperature overnight until they were macroscopically homogeneous and then stored at 4°C. The PS concentration was typically between 21 and 30 percent by weight. The PS solution was electrospun using a conventional set-up (see Figure 2.1). Briefly, PS solution was pumped (New Era Pump System, Inc., Farmingdale, NY) through a 22-gauge (inner diameter = 0.508 mm) stainless steel needle (Jensen Global, Santa Barbra, CA) at a constant rate while applying a constant voltage (Matsusada High Precision Inc., Shiga, Japan). The mats were produced with a NCD of about 10 cm, with an applied voltage of 11 kV, and with a solution flow rate of 0.5 mL/hr.

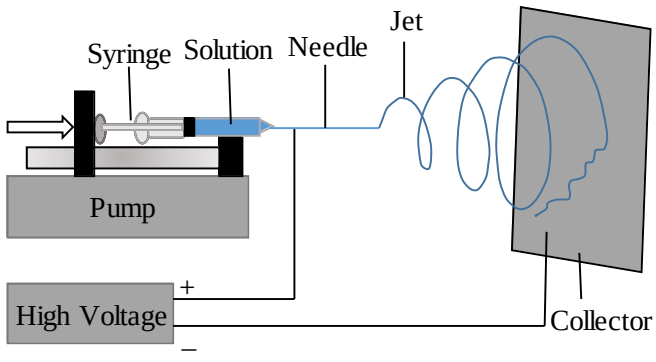


**Figure 2.1**: Electrospinning setup.

In order to measure the fiber diameter, small sections of about $5\text{mm} \times 5\text{mm}$ were cut from the central portions of the deposited non-woven structure on the substrate for the SEM analysis. Figure 2.2 presents the SEM images of 30 wt% Polystyrene mats from the top view (left) and side view

(right). It can be seen that the fibers were almost straight having circular cross section with a small bending between fiber-fiber cross overs. Average diameter of the fibers was obtained through imaging the resulting mats using a scanning electron microscope (averaged over more than 50 fibers per image) as shown in Figure 2.2. Inset shows the percentage distribution of fiber diameter for the sample presented in Figure 2.2.

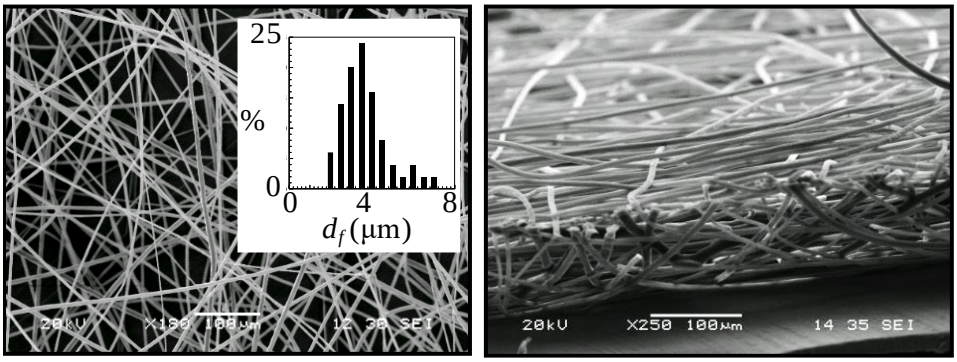


**Figure 2.2**: Selected scanning electron micrographs of a) A Polystyrene mat obtained by 30 min electrospinning (30wt%, 11kV, 10cm distance, 0.4ml/hr). b) The side view of Polystyrene mat. Fiber diameter distribution of electrospun Polystyrene for 22wt% PS/THF.

### 2.2.1 Thickness Measurement Using a Micrometer and via Buoyancy Method

In order to estimate the thickness of the mats, $75mm \times 25mm$ samples were cut from the central region of the mats and used for thickness measurement. The thickness can be measured using two different techniques, micrometer and buoyancy method. The sample mats, on the aluminum foil, were then sandwiched between two glass slides, and the overall thickness of the entire setup was measured by averaging the local thicknesses obtained in different locations using an accurate micrometer from Mitutoyo. The mat thickness was then obtained by subtracting the thickness of the known (or easy-to-measure) parts from the assembly. We also measured the thickness of the mats using an in-house buoyancy technique that takes advantage of the hydrophobicity of the PS

mats (see Figure 2.3) [87]. In this method, the difference between the weights of a submerged glass slide with and without the PS mat $\Delta f_b$ (i.e., the weight of the water displaced by the air entrapped inside the submerged mat) was used to estimate the thickness of the mat using the following simple equation.

$$t = \frac{1}{a_s}\left(\frac{\Delta f_b}{\rho_w g}\right) \tag{2.1}$$

In this equation, $a_s$ is mat's surface area, $\rho_w$ is density of DI water used in the experiment, and $g$ is the gravitational acceleration.

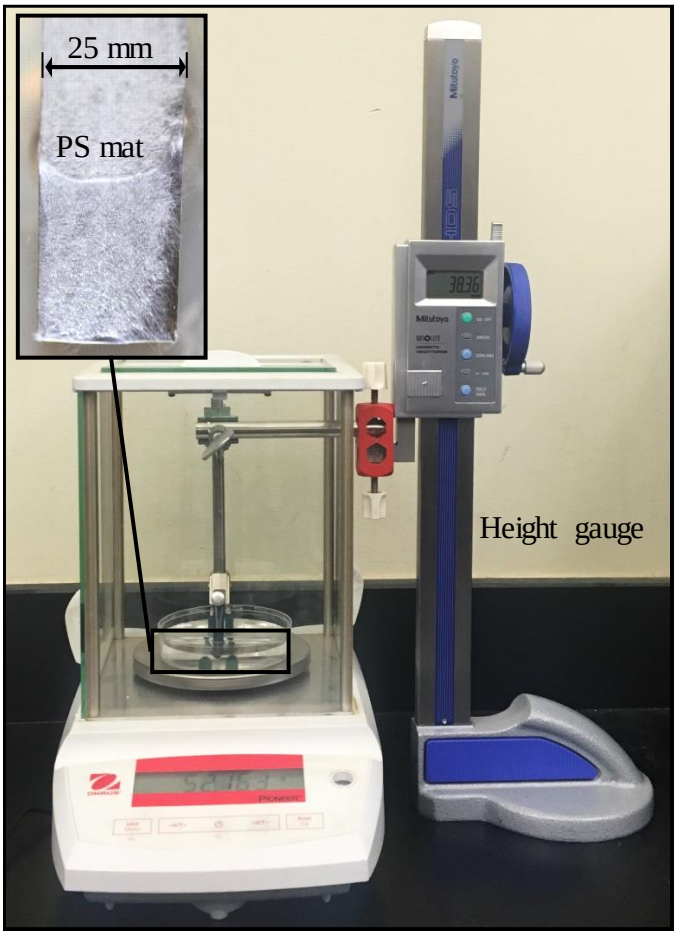


**Figure 2.3**: Setup used to estimate effective thickness and gas volume fraction of superhydrophobic coatings: photograph of actual setup, the image in the box presents a layer of air that is entrapped in the submerged portion of the Polystyrene mat.

### 2.3 Numerical Simulation

Our steps in simulating electrospun PS mats are as follows. Adopting the model of Refs. 33 and 34, we first simulate the formation of a single filament as it exits the needle and flies in air to reach the collector (Section 2.3.1). We then use the calculated filament diameter and filament deposition velocity to generate 3-D virtual fibrous structures that resemble the morphology of electrospun PS mats (Section 2.3.2). The resulting combined simulation approach allows one to study how electrospinning parameters (e.g., voltage) affects mats properties (e.g., porosity).

#### 2.3.1 Simulation of Filament Electrospinning

The electrospinning model considered in this section was developed in Refs. 33 and 34 and also used in many subsequent investigations [43,47,50]. Using the Maxwell viscoelastic model in this work, the polymer jet (i.e., filament) is treated as an array of beads with a mass of $m_i$ separated by a distance $l_i = |\vec{r}_i - \vec{r}_{i-1}|$ interconnected by springs and dampers (viscoelastic elements) in a series (Figure 2.4). Neglecting the gravitational force, the viscoelastic forces acting on bead $i$ by its neighbors (bead $i-1$ and bead $i+1$) are given as

$$\overrightarrow{f_i^{ve}} = \frac{\pi d_{i+1}^2 \sigma_{i+1}}{4 l_{i+1}} (\vec{r}_{i+1} - \vec{r}_i) - \frac{\pi d_i^2 \sigma_i}{4 l_i} (\vec{r}_i - \vec{r}_{i-1}) \tag{2.2}$$

where $d_i$ is the filament diameter at the location of bead $i$, defined by $\vec{r}_i = (x_i, y_i, z_i)$. Sigma is the normal stress acting on the filament cross-section at the location of bead $i$, with its rate of change with time given as

$$\frac{d\sigma_i}{dt} = \frac{G}{l_i}\frac{dl_i}{dt} - \theta\sigma_i \tag{2.3}$$

where $G$ is the elastic modulus and $\theta = \frac{\mu}{G}$ is the relaxation time of the polymer jet.

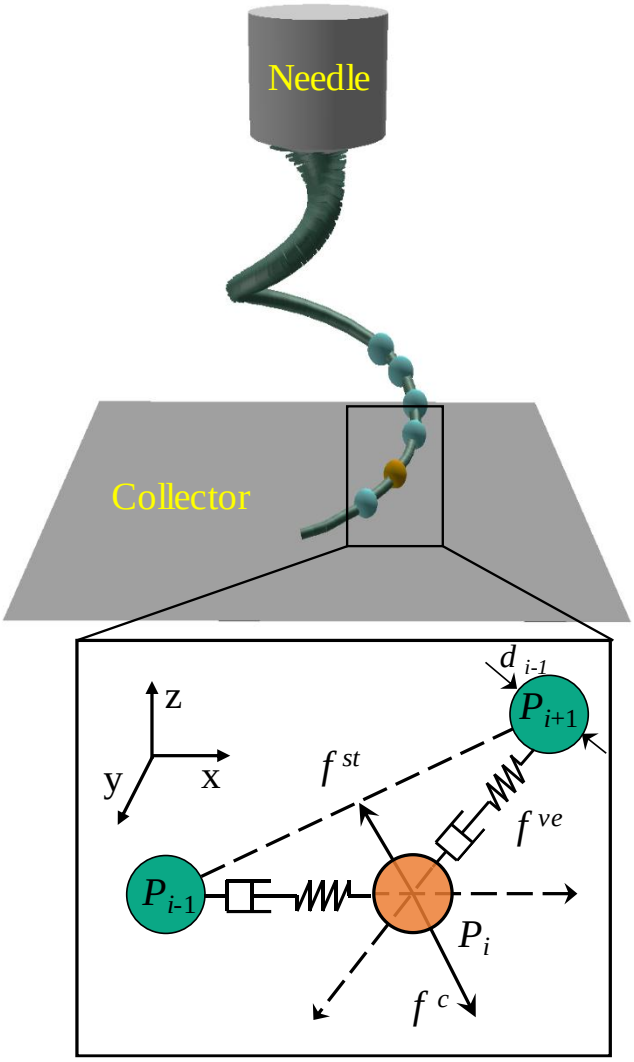


**Figure 2.4**: Diagram of the electrospinning model. The three dimensional discrete mass-spring-damper model representation of a jet flow of [33,34] We represent the Maxwell viscoelastic force, $f^{ve}$, the surface tension force, $f^{st}$, pointing the center of curvature to restore the rectilinear shape, and the Coulomb repulsive term, $f^{c}$, which is the sum over all the repulsive interactions between the beads. The external electric potential, $V_0$, is indicated by the big arrow in figure, while the upper cone represents the nozzle.

The other force acting on bead $i$ is the surface tension force $\overrightarrow{f_i^{st}}$ which provides resistance against bending of jet's centerline as it travels toward the collector,

$$\overrightarrow{f_i^{st}} = \alpha k_i \pi \left(\frac{d_i + d_{i-1}}{4}\right)^2 \frac{(\overrightarrow{x_i} + \overrightarrow{y_i})}{(x_i^2 + y_i^2)^{1/2}} \tag{2.4}$$

where $\alpha$ is the surface tension of the polymer, $k_i$ is the curvature of the jet in the x–y plane, and $x_i$ and $y_i$ are the $x$ and $y$ coordinates of bead $i$. The polymer jet stretches as it travels from the needle to the collector due to an external potential $V_0$ leading to an electric attraction force $\overrightarrow{f_i^{el}}$ acting on the beads as

$$\overrightarrow{f_i^{el}} = -e_i \frac{V_o}{H} k \tag{2.5}$$

where $H$ is the NCD, $e_i$ is the charge on bead $i$, and $k$ is the unit vector in the z-direction. The Columbic force acting on bead $i$ by other charged beads in the jet $\overrightarrow{f_i^{C}}$ is given by

$$\overrightarrow{f_i^{C}} = \sum_{\substack{j=1 \\ j \neq i}}^{n} \frac{{e_i}^2}{R_{ij}^3} (\vec{r}_i - \vec{r}_j) \tag{2.6}$$

where $R_{ij}$ is the distance between bead $i$ and any other bead $j$ in the jet.

Applying Newton's second law to each bead in the polymer jet, one obtains a system of coupled ordinary differential equations, i.e.,

$$\frac{d}{dt}\begin{bmatrix} v_i \\ \vec{r}_i \end{bmatrix} = \begin{bmatrix} \vec{f}_i^{\Sigma}/m_i \\ v_i \end{bmatrix} \tag{2.7}$$

where $\vec{f}_i^{\Sigma} = \overrightarrow{f_i^{ve}} + \overrightarrow{f_i^{st}} + \overrightarrow{f_i^{el}} + \overrightarrow{f_i^{C}}$ and $\vec{r}_i$ is the position vector of bead $i$. $m_i$ represents the mass of bead $i$ which decreases along the jet as the of solvent evaporates. Solving Equation 2.7

numerically results in the instantaneous position and velocity of the beads constituting the filament during their travel from the needle to the collector.

Following the work of Refs. 33 and 34, we calculate the rate of solvent evaporation from the filament using a Sherwood number correlation that relates the convective mass transfer coefficient $h_m$ to Reynolds $Re = \frac{\rho_s V_i l_i}{\eta_a}$ and Schmidt $Sc = \frac{\eta_a}{\rho_s D_a}$ numbers written for the traveling filament (treated as a cylinder moving in air in a direction parallel to its axis) [34],

$$Sh = \frac{h_m d_i}{D_a} = 0.495 Re^{\frac{1}{3}} Sc^{\frac{1}{2}} \tag{2.8}$$

where $D_a$ is diffusion coefficient for solvent vapor in air.

Obtaining $h_m$ from Equation 2.8, the rate of change of solution mass due to evaporation can be calculated as,

$$\frac{\partial m_i}{\partial t} = -\pi \rho_s h_m \left[c_{e,eq} - c_{s\infty}\right] d_i l_i \tag{2.9}$$

where $\rho_s$ is the density of the polymer solution, $d_i$ is the jet diameter,$l_i$ is the distances between bead $i$ and bead $i$+1 (the length of the filament segment), $c_{s,eq}$ is solvent vapor concentration at saturation (ambient temperature), and $c_{s,\infty}$ is solvent vapor concentration in far field. Combining Equations 2.8 and 2.9, one can predict the rate of change of jet volume due to evaporation, i.e.,

$$\frac{\partial V_i}{\partial t} = -0.495 \pi D_a Re^{\frac{1}{3}} Sc^{\frac{1}{2}} \left[c_{e,eq} - c_{s\infty}\right] l_i \tag{2.10}$$

where $V_i$ is the filament segment volume which is a function of the area of jet multiplied by the segment length $l_i$. Solving the 1st order ordinary differential equation given in Equation 2.10, one can obtain the diameter of the filament as it travels from the needle toward the collector over time.

As mentioned earlier in Section 2.2, the fibers are made from a solution of PS (1060 kg/m$^3$) in a mixture of Toluene and Acetone (7:3 w/w). The polymer-specific input parameters used in the filament formation simulations are given in Table 2.1, and they include mass, charge density, and relaxation time $\theta$. The relaxation time for a typical PS solution is reported to be in the range of 8 to 11 ms [123]. Here, we assumed a relaxation time of $\theta$ =10 ms to be consistent with that used in the work of Refs. 33 and 34.

Table 2.1: Input parameters for PS jet flow simulations.

| $a_0$ (cm) | $e$ ($g^{1/2}cm^{3/2}/s$) | $\alpha$ ($kg/s^2$) | $m$ (kg) | $V_0$ (kV) | $q$ (mL/h) | $G$ ($g/cm\ s^2$) | $H$ (cm) |
|---|---|---|---|---|---|---|---|
| $15\times10^{-3}$ | 8.48 | 0.7 | $0.283\times10^{-8}$ | 11 | 0.5 | $3\times10^{9}$ | 10 |

The filament simulation starts with two beads with their initial conditions considered as input. The instantaneous position and velocity of these beads are then calculated by solving Equation 2.7 via an in-house Python code. In each time step, the algorithm checks for the distance between the last bead and the needle. If the last bead has travelled more than $0.0005H$ (0.05% of the NCD), the algorithm then adds a new bead at a distance of $0.00025H$ from the needle. The code also checks the *z*-coordinate of the first bead at every time step to stop the simulation when it reaches the collector.

### 2.3.2 Simulation of Filament Electrospun Mats

In generating an electrospun mat, we assume the mat to be made of hundreds (or thousands) of individual fibers deposited horizontally on top of one another. Note that we only simulate a small portion (less than 1 mm by 1 mm) of an actually large (about 150 mm by 150 mm) mat due to computational limitations. In addition, we consider the fibers to be solid (unlike the polymer jet of Section 2.3.1). The fibers are again treated as arrays of beads interconnected by springs and dampers but in parallel arrangement (the Kelvin–Voigt model suitable for solid fibers) as shown in Figure 2.5 [95]. From a free body diagram showing the force acting on bead $i$ by the beads to which it is connected, one obtains (Figure 2.5),

$$\vec{f}_i^{\Sigma} = \vec{f}_{i,i-2}^{s} + \vec{f}_{i,i-1}^{s} + \vec{f}_{i,i+1}^{s} + \vec{f}_{i,i+2}^{s} + \vec{f}_{i,i-2}^{d} + \vec{f}_{i,i-1}^{d} + \vec{f}_{i,i+1}^{d} + \vec{f}_{i,i+2}^{d} + \vec{f}_i^{C} \tag{2.11}$$

In this equation, $\vec{f}^{s}$ and $\vec{f}^{d}$ represent spring and damper forces, respectively, i.e.,

$$\vec{f}_{i,i+1}^{s} = -k_s(\|\vec{p}_i - \vec{p}_{i+1}\| - l_r)\frac{(\vec{p}_i - \vec{p}_{i+1})}{\|\vec{p}_i - \vec{p}_{i+1}\|} \tag{2.12}$$

$$\vec{f}_{i,i+1}^{d} = -k_d(\vec{u}_i - \vec{u}_{i+1}) \tag{2.13}$$

The last term on the right-hand side of Equation 2.11 is the electrostatic force applied on each bead by the field, and it can be described using Equation 2.6. The dynamics of fibers depositing on top of one another (and bending at the fiber–fiber crossovers) can be simulated through solving a system of coupled differential equations similar to the one given in Equation 2.7.

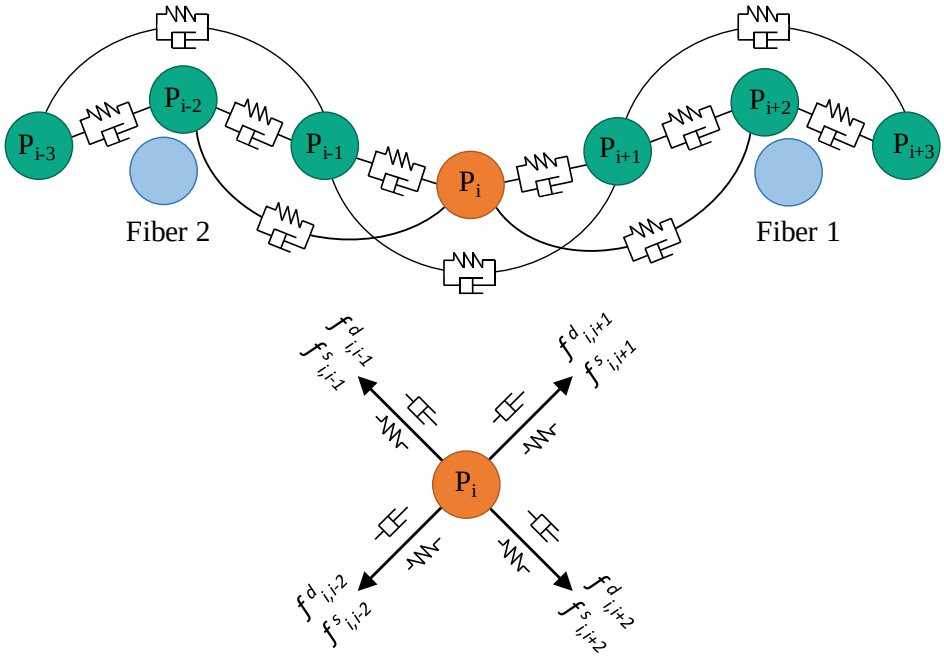


**Figure 2.5**: Schematic representation of a fiber comprised of point masses, springs, and dampers (our MSD model [95]) and the free body diagram showing the forces acting on a bead.

Accurate simulation of the bending fibers at fiber-fiber crossovers is an important yet challenging task that can directly affect the thickness and porosity of a fibrous mat. The extent of bending that occurs at the fiber crossovers depends strongly on the viscoelastic properties of the fibers as well as the electrostatic and aerodynamic fields during fiber deposition and solidification processes. In the absence of detailed quantitative information with regards to these factors, it is practically impossible to predict the morphology of an electrospun fiber mat. As such, the simulation algorithm developed in the current work is aimed to only shed some light on this complicated problem by studying the viscoelasticity properties from experiments.

### 2.3.3 Combined Algorithms

In this section, we present a procedure to simulate the formation of electrospun fiber-mats starting from the needle. The aforementioned equations from Section 2.3.1 are programed in a Python code to simulate the formation of filaments during electrospinning. The simulation starts by introducing two beads with the initial conditions needed to create the first filament segment (segments are represented with imaginary beads having a constant diameter equal to that of the local diameter of the filament). Beads enter the simulation domain vertically from the needle with given initial properties (zero initial radial velocity and stress, but an initial perturbation to the $x$ and $y$ positions of the beads). The next step in filament formation modeling is to calculate the rate of solvent evaporation which can directly affect filament diameter, and then to update the charge and viscoelastic properties of the filament. The distance between two beads, which presents the stretching of filaments, depends strongly on the material of the polymers as well as the electrostatic and aerodynamic fields during spinning and vaporization. During filament formation, diameter of the jet becomes smaller due to stretching. Moreover, conservation of charges in the jet elements helps to obtain the charges on the beads.

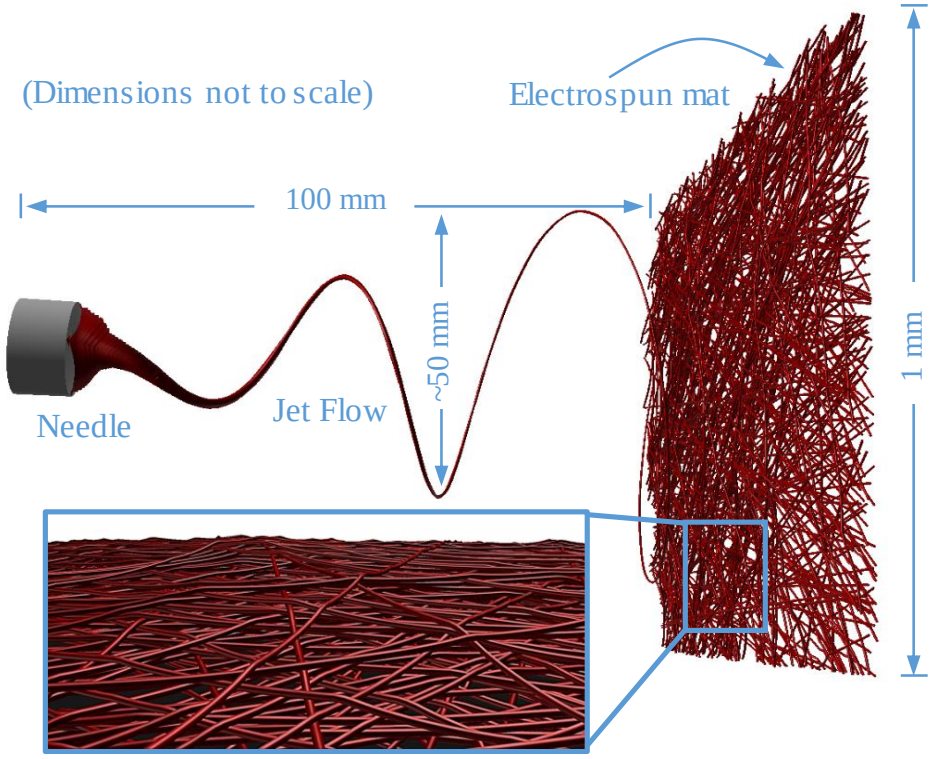


**Figure 2.6**: Our combined filament formation and mat generation algorithms.

Detailed quantitative information with regards to these factors is necessary to predict the trajectory of the filament in air. The conservation of momentum was written for each bead, which resulted in a system of coupled ordinary differential equations (Equation 2.7) to be solved using a Runge–Kutta 4$^{th}$ order (RK-4) method with a time step of 0.05 μs. This results in the position and velocity of the beads as function of time during the integration time (see Figure 2.6). In each time step, the algorithm checks whether or not a collision has occurred between the beads and if the first bead has reached the collector at $z = 0$ (criterion to stop the simulation). The velocity and diameter of the first bead are taken as the deposition velocity and fiber diameter in the mat generation algorithm. In the mat generation simulation, fibers enter the simulation domain horizontally and with an initial vertical velocity (deposition velocity). Once deposited (and deformed), the fibers are assumed to be rigid. Fiber interpenetration is avoided by checking the distance between the

beads at each time step to make sure that no beads can come closer to one another by a distance less than a fiber diameter (see the magnified image in Figure 2.6). Our collision detection algorithm searches for a collision between the beads of a new fiber and those of the deposited fibers. A similar procedure, as explained earlier in this subsection, is repeated to deposit a certain number of fibers (determined based on the desired weight per square meter) [95]. The thickness of the virtual mats is estimated by averaging the z-coordinates of a few representative beads near the top surface. The length of the fibers in the mat is obtained by calculating the distance between adjacent beads along the length of each fiber. The solid volume fraction of the mat is then obtained knowing the total number of deposited fibers (and their volumes) and the macroscopic dimensions (i.e., volume) of the mat.

### 2.4 Results and Discussion

We start by presenting an example of our filament trajectory predictions obtained for a PS filament spun under an electrostatic field of $V_0 = 11\ kV$ across a NCD of $H = 10\ cm$. As can be seen in Figure 2.7, the filament follows a spiral trajectory as it travels from the needle toward the collector. Note that the diameter of the spiral trajectory on the collector is about 6 to 7 cm, and this explains why the fibers appear to be relatively straight in the 700 μm × 500 μm SEM images taken from the actual mats (e.g., Figure 2.2). This also serves as a justification for considering straight fibers in simulating electrospun mats in this chapter.

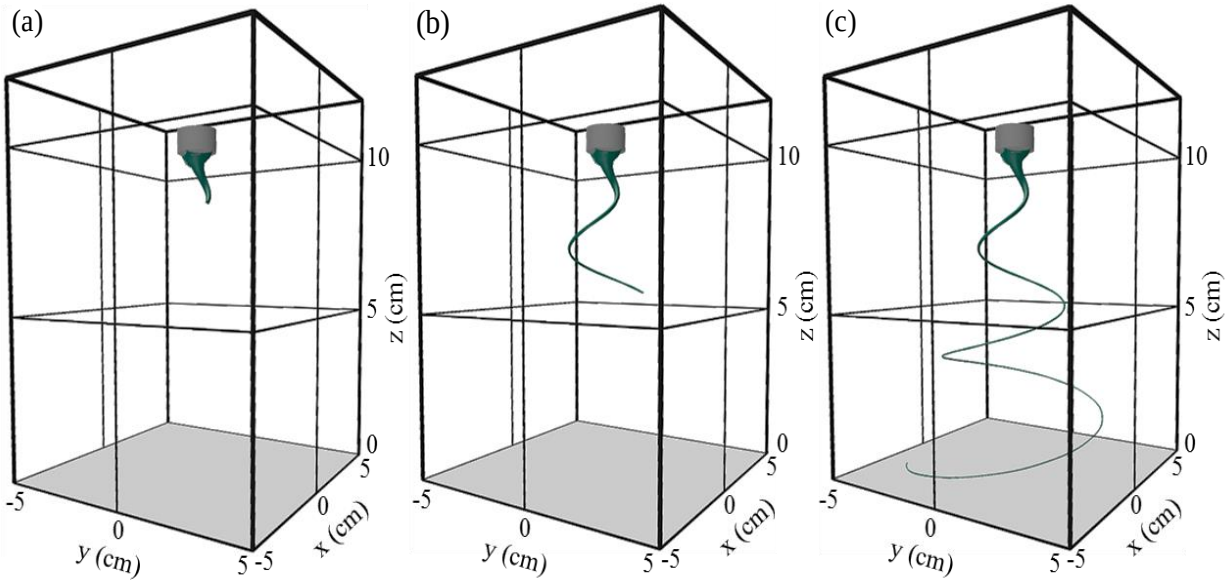


**Figure 2.7**: An example of filament trajectory simulations in 3-D is given in 3 different times (1ms, 2ms, and ~5ms).

Figure 2.8a shows the effects of PS concertation on filament final diameter (i.e., fiber diameter in the mat) obtained from the simulations. These results are also compared with their experimental counterparts measured from SEM images. We believe that the agreement between the experimental and computational results is reasonably good, given the complexity of the electrospinning process and the simplifying assumptions considered in developing the model. This figure shows that fiber diameter increases from about 2 μm to about 6 μm with increasing polymer concentration from 20% to 30% (due perhaps to the increase of the solution viscosity working against filament stretching). The results shown in Figure 2.8a are in qualitative agreement with the experimental observations reported in Refs. [48,124-126]. Figure 2.8b shows filament diameter versus NCD. It can be seen that filament diameter decreases from about 110 μm near the needle down to about 4 μm near the collector due to solvent evaporation and mechanical stretching. Input parameters used for this simulation are given in the figure. The results shown in Figure 2.8b are in

qualitative agreement with the work of Ref. 48 who also used the electrospinning model of Refs. 33 and 34 to study the effects of polymer properties and electrospinning conditions on filament diameter. The filament diameter decreases rapidly over a distance of less than a centimeter flow the needle. This is because the jet is more fluid (more stretchable) near the needle but it becomes more viscous later during its flight toward the collector due to solvent evaporation [48].

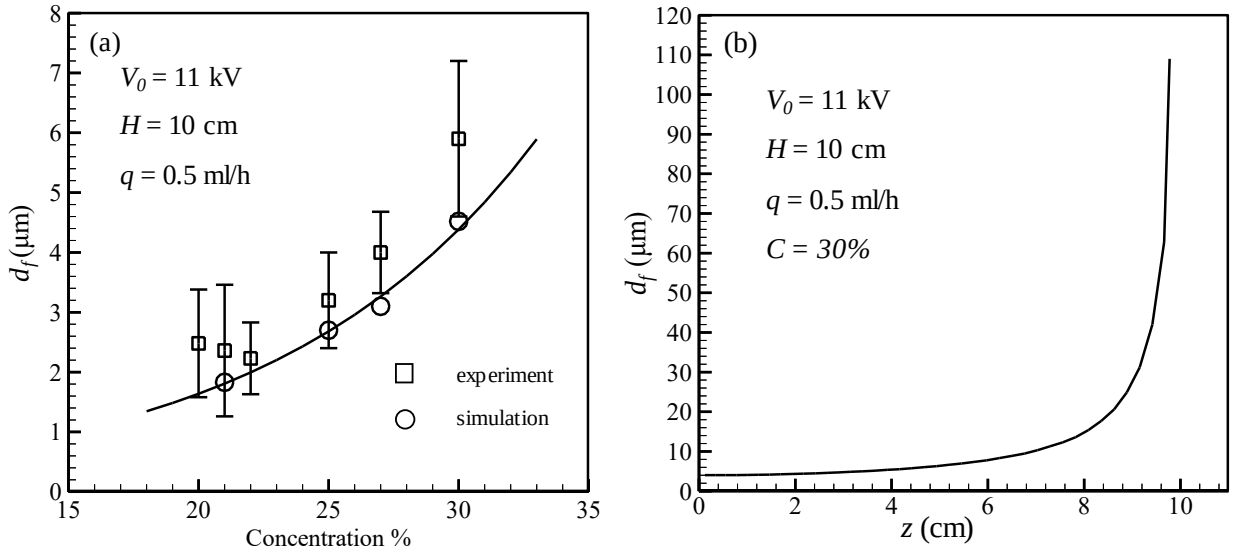


**Figure 2.8**: Average fiber diameter is shown versus PS concentration in (a) for electrospun mats produced at a flow rate of 0.5 ml/h with a voltage of 11 kV with a NCD of 10 cm. Predictions from our numerical simulations are added to this figure for comparison. Jet local diameter (beads diameter) is given in (b). See Table 2.1 for simulation parameters.

Figure 2.9 shows the axial (in the z-direction) and the radial velocity of the beads along the length of the filament. It can be seen that axial velocity is almost constant while the radial velocity monotonically increases with distance (filament velocity is a function of electric field, NCD, and polymer properties) [33]. The resultant bead velocity at the moment of contact with collector is marked with a red circle in Figure 2.9, and it is about 20 m/s for the case simulated. This velocity is used in our mat generation code as the filament deposition velocity.

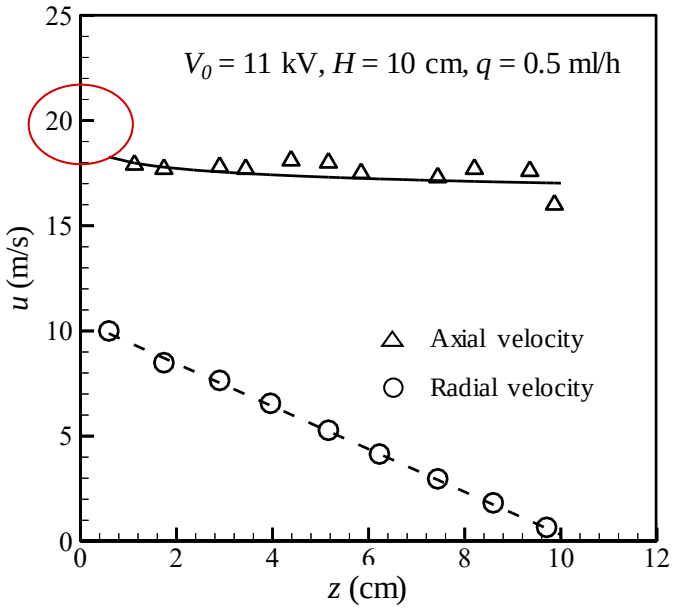


**Figure 2.9**: Predictions from our numerical simulations for jet local velocity (beads velocity) for a Polystyrene parameters shown in Table 2.1.

As mentioned earlier in the Introduction, for the fiber-to-fiber interactions to be accurate, the MSD model needs to be calibrated using material-dependent values for the stiffness of the springs and dampers used in modeling each individual fiber. In the absence of such fiber-level information, we calibrated our MSD model using thickness data obtained from electrospinning PS mats. To obtain a relationship between fiber diameter and mat thickness experimentally, a series of electrospun PS mats was produced under different spinning conditions. The thickness of these mats was then measured using the aforementioned buoyancy and micrometer methods. The thickness data were non-dimensionalized using fiber density and mat's basis weight (weight per square meter) as shown in Figure 2.10a. We fitted these data with a linear curve, for the lack of a better justifiable alternative, i.e.,

$$\tau = a_0 d_f + a_1 \tag{2.14}$$

where $\tau = t\rho/W_b$ is dimensionless thickness and $d_f$ is fiber diameter. In this equation, $a_0$and $a_1$ are the curve fit coefficients, and they are found to be $a_0 = -1.98\frac{1}{\mu m}$ and $a_1 = 25.15$, for data from micrometer measurements, and $a_0 = -1.55\frac{1}{\mu m}$ and $a_1 = 25.85$ for the data from the buoyancy method. Given the errors associated with the measurement techniques, we averaged the curve fitting coefficients to obtain a single equation for dimensionless thickness, as

$$\tau = -1.75d_f + 25 \tag{2.15}$$

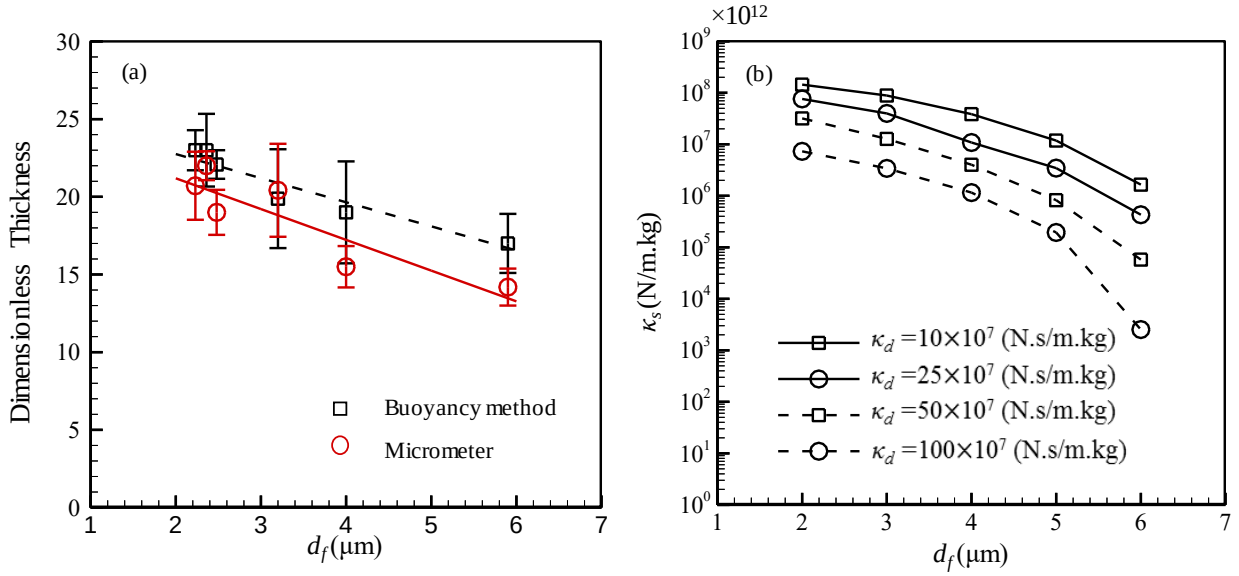


**Figure 2.10**: Dimensionless thickness obtained from the buoyancy method and micrometer measurements are compared with one another in (a). The dashed line used to show the Buoyancy method results. PS concentration was varied from 20% to 30% but flow rate, voltage, and NCD were fixed at 0.5 ml/h, 11 kV, and 10 cm, respectively. Possible spring coefficients to generate a virtual PS mat with a dimensionless thickness matching that from experiment is given in (b) for different fiber diameters and damping constants.

Using this empirical correlation, one can estimate the thickness of the electrospun PS mats for the range of fiber diameters shown in Figure 2.10a. More importantly, this correlation has been used

in this study to calibrate our PS mat generation algorithm. For the calibration process, we found the spring and damping coefficients that could be used to generate virtual mats with average dimensionless thickness values matching those obtained from Equation 2.15 for a fiber diameter in the range of 2 to 6 μm. More specifically, Figure 2.10b shows spring constants that can be used to generate a mat with an average dimensionless thickness matching that from Equation 2.15 for any fiber diameter from 2 to 6 μm using an arbitrary damping constant in the range of $10^8 < \kappa_d < 10^9 N.s/m.kg$. It is interesting to note that larger spring constants are obtained for thinner fibers. This is because increasing the diameter of the fiber, decreases the number of beads required to represent that fiber in the mat generation algorithm (fibers are made of beads with a diameter equal to that of the fiber). This in turn, decreases the number of springs and dampers needed to connect the beads to one another, and consequently, increases the rigidity of the fiber [95]. Information given in Figure 2.10b are used to produce a third-order correlation for spring constant $\kappa_s$ as a function of fiber diameter, as given below.

$$\kappa_s = \beta_0 + \beta_1 d_f + \beta_2 {d_f}^2 + \beta_3 {d_f}^3 \qquad (2.16)$$

In this equation, $\beta_0 = \lambda_{00}{\kappa_d}^{\lambda_{01}}$, $\beta_1 = \lambda_{10}{\kappa_d}^{\lambda_{11}}$, $\beta_2 = \lambda_{20}{\kappa_d}^{\lambda_{21}}$, and $\beta_3 = \lambda_{30}{\kappa_d}^{\lambda_{31}}$, where $\lambda_{00} = -7 \times 10^{10}$, $\lambda_{01} = -1.92$, $\lambda_{10} = 4 \times 10^{11}$, $\lambda_{11} = -1.74$, $\lambda_{20} = -3 \times 10^{12}$, $\lambda_{21} = -1.78$, $\lambda_{30} = 3 \times 10^{12}$ and $\lambda_{31} = -1.70$. The damping constants are in the range of $10^8$ to $10^9 N.s/m.kg$.

With the calibrated code, one can produce virtual PS mats with different average fiber diameters and use them to estimate the thickness (or porosity) of an actual PS mat. In addition, such mats can be used in virtual design of fibrous media for various applications such as droplet-air or droplet-liquid separation (e.g., Refs. 120 and 127), functional coatings [10,11,88,128,129] or superhydrophobic layers [130,131] among many other applications. Note that our mat generation

algorithm is calibrated using a fixed, but yet quite common, set of electrospinning parameters (e.g., $V_0 = 11\ kV$ and $H = 10\ cm$). The proposed spring and damping coefficients therefore become less accurate when the electrospinning conditions are significantly different from those considered here.

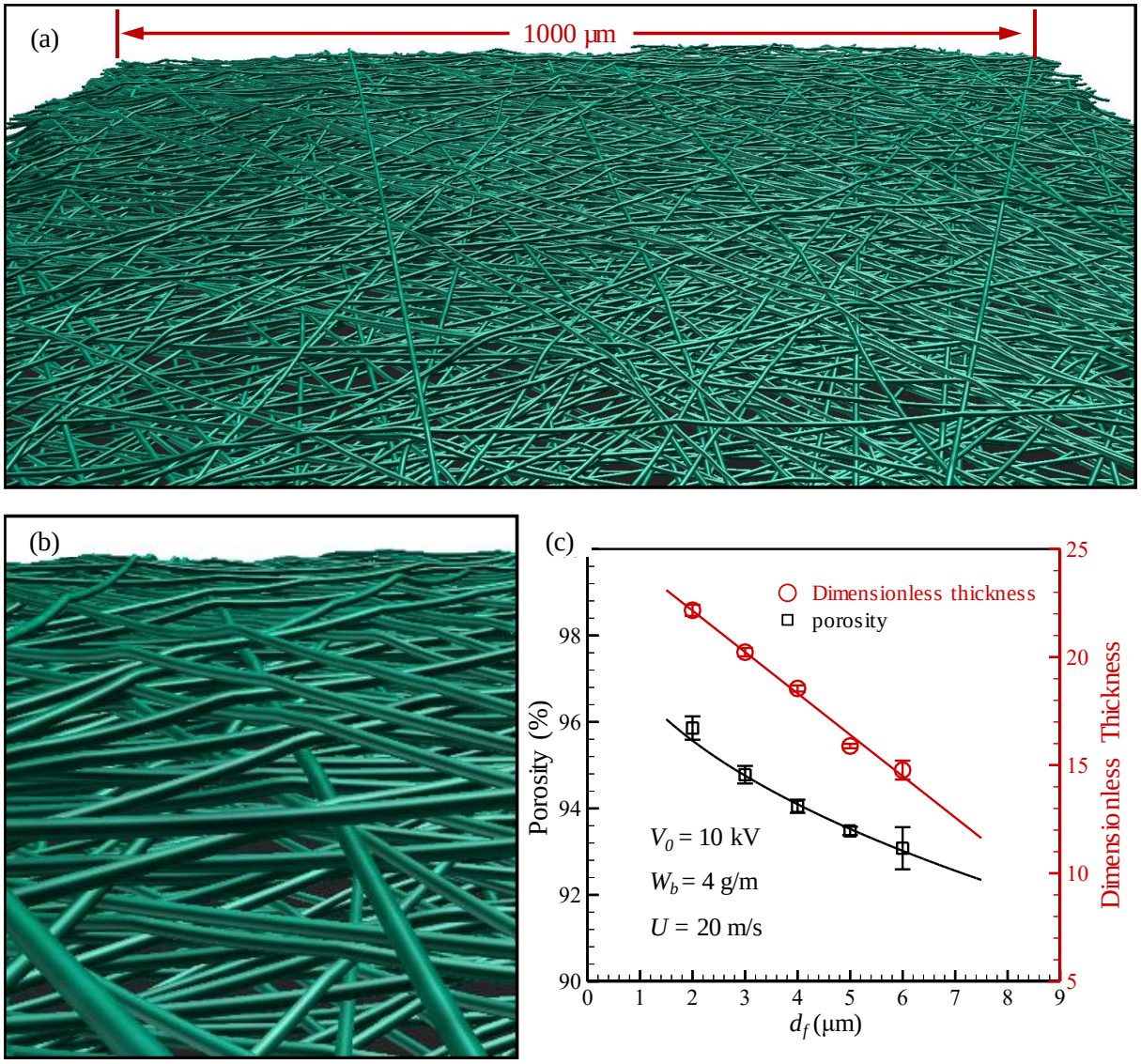


**Figure 2.11**: A sample virtual PS mat made of fibers with a diameter of 3 μm and having a basis weight of 4 g/m$^2$ is shown in (a) along with a magnified image showing bending of the fibers at cross-overs in (b). Predictions of our calibrated code for the effects of fiber diameter on porosity and dimensionless thickness are given in (c).

Figure 2.11a shows an example of the PS mats produced using our calibrated mat generation code. The mat has a basis weight of $4\ g/m^2$ and it is comprised of fibers with a diameter of $d_f = 3\ \mu m$ deposited with a velocity of 20 m/s. The average thickness and average porosity for these mats were found to be about $78.4\ \mu m$ and 94.7%, respectively. The magnified image in Figure 2.11b shows the bending of the fibers at crossovers. Figure 2.11c shows porosity and dimensionless thickness versus fiber diameter for PS mats having a constant basis weight of $4\ g/m^2$. It can be seen that mats made up of thicker fibers (identical basis weights) have lower porosity and thickness values [95].

To demonstrate how the computational tool developed in this study can be used in predicting the outcome of an electrospinning process, we present the effects of electrospinning parameters (e.g., voltage or NCD) on thickness of the resulting virtual mats. To generate these results, we first ran the filament formation code to quantify the effects of electrospinning parameters on filament diameter and filament deposition velocity. We then used this information in the mat generation code to create 3-D fibrous structures and obtain their average thickness or porosity. Effects of DC voltage on filament diameter depends on the type of polymer used in the spinning process. Fiber diameter has been reported to increase with increasing voltage for certain polymers [124,126,133-136], but to decrease for some other polymers [116,125,137,138]. Our simulations for PS indicate that increasing DC voltage from 10 kV to 25 kV increases the filament diameter and deposition velocity by about 250% and 30%, respectively (Figure 2.12a). We believe this is because increasing the voltage increases the velocity of the PS jet (shortens the time of travel as can be seen in the inset figure) leaving insufficient time for evaporation to further reduce the filament diameter (increasing the voltage increases the attraction force on the filament acc. to Equation 2.5).

The results shown in Figure 2.12a are in qualitative agreement with the experimental results reported in Ref. 48. Contrary to the results shown in Figure 2.12a, increasing the NCD from 5 cm to 15 cm seems to decrease the filament diameter and deposition velocity by about 300% and 25%, respectively, as can be seen in Figure 2.12b. The decreased velocity (i.e., increased time of travel as shown in the inset) allows more time for the filament to reduce its diameter through solvent evaporation. This is in agreement with the reported observations in the literature that increasing NCD results in a decrease in fiber diameter and also an increase in mat thickness (which is in agreement with our simulation results in Figure 2.13b) [125,126,135,138,139].

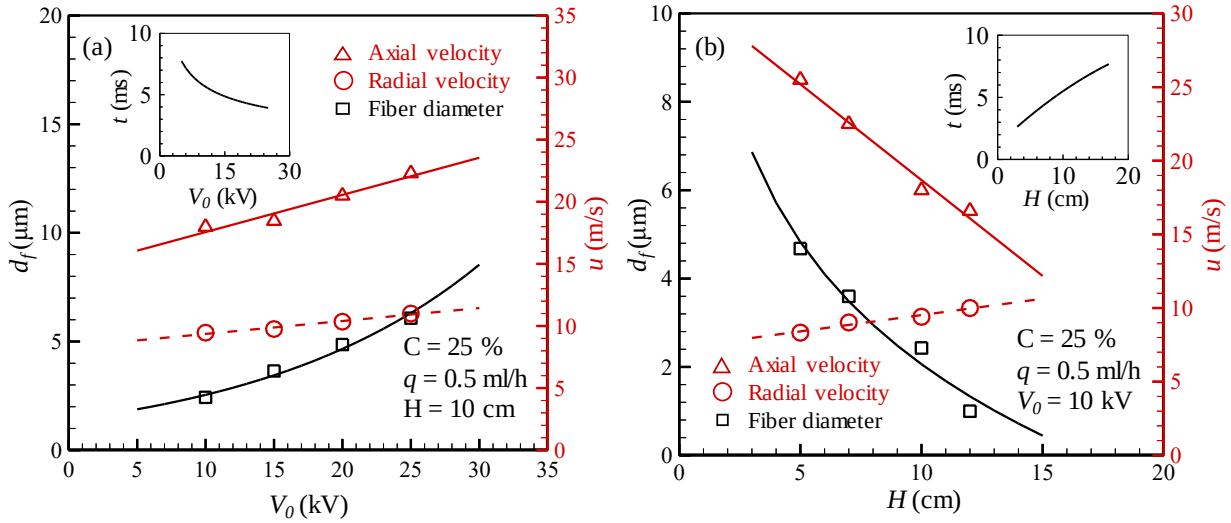


**Figure 2.12**: Fiber diameter and fiber deposition velocity obtained from simulating PS filaments are shown in (a) and (b) versus DC voltage and NCD, respectively. The inset figures show the time of flight.

Figures 2.13a and 2.13b present the effects of DC voltage and NCD on porosity and dimensionless thickness of resulting PS mats. It can be seen that mat porosity and thickness tend to decrease with voltage but to increase with NCD.

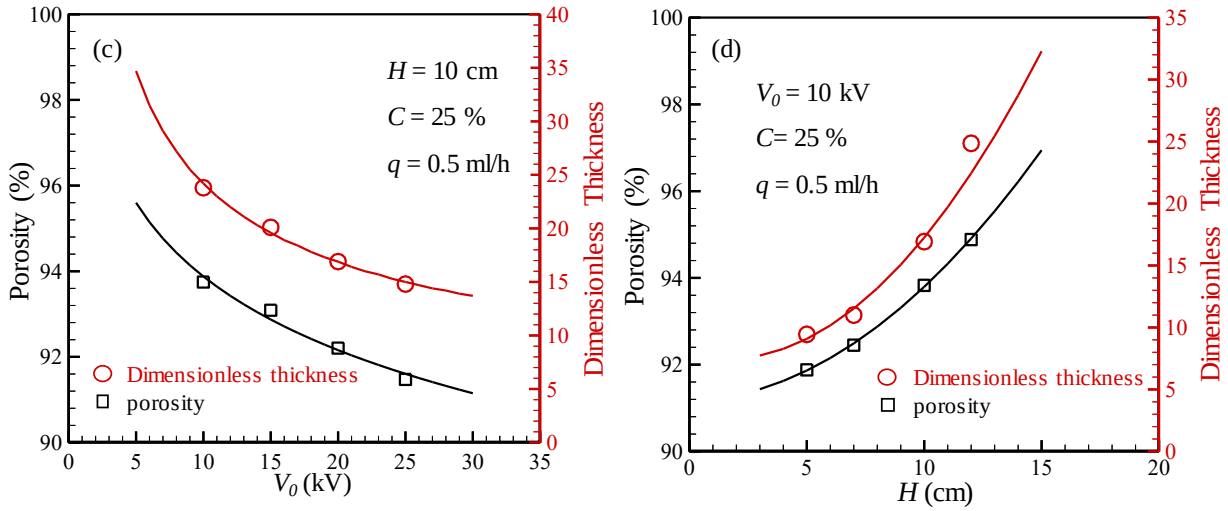


**Figure 2.13**: Porosity and dimensionless thickness are shown in (c) and (d) for the virtual electrospun mats obtained fibers produced in (a) and (b), respectively.

The decrease of mat thickness with increasing voltage is believed to be due to the increase of the fiber diameter with voltage (Figure 2.12a). The increase in fiber diameter in turn decreases mat's dimensionless thickness (Figure 2.11c). Likewise, the mat dimensionless thickness increases as the fiber diameter decreases with increasing NCD (Figure 2.12b).

For completeness of the study and additional verification, we have compared the predictions of our model with those reported in Ref. 48. Figure 2.14 presents dimensionless filament diameter versus NCD and DC, and to make the comparison possible, the filament diameter is normalized using that obtained for a reference case of $H^{ref} = 10$ cm and $V_0^{ref} = 10$ kV. The agreement between the model predictions is reasonable, given the fact that the polymer used in our work (i.e., PS) is different from the one considered in Ref. 48.

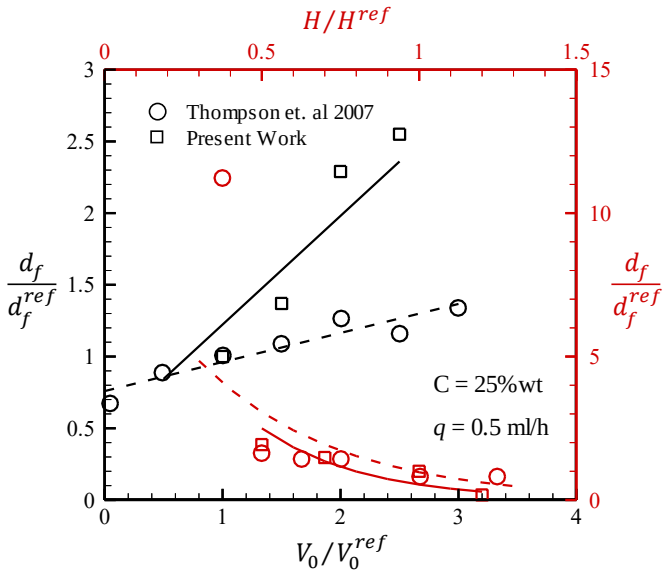


**Figure 2.14**: Fiber diameter obtained from simulating PS filaments are shown versus DC voltage and NCD, respectively, for present work and Thompson et al. 2008 [48].

## 2.5 Conclusions

Interested in quantifying the impact of varying different electrospinning parameters on the morphology of the resulting fibrous materials, we combined the electrospinning model of Yarin and Reneker and their co-workers [33,34] with our structure generation algorithm (see Ref. 95). PS mats from different PS solution concentrations were also produced and used to 1) validate the filament simulation code (see Figure 2.10b), and 2) calibrate the structure generation algorithm (see Figure 2.11). The calibrated simulations were then used to quantify the role of voltage and NCD in electrospinning fibrous mats. Our results indicate that increasing the voltage or decreasing the NCD increases the diameter of the resulting fibers but decreases the dimensionless thickness and porosity of the fiber-mats (see Figure 2.13).

A unique attribute of the computational tool developed in this work is the ability to create 3-D fibrous structures comprised of non-penetrating fibers with fiber curvatures realistically obtained from a physics-based mathematical model for the first time. Such virtual structures can be used as a platform for additional studies in a variety of applications requiring an accurate representation of surface morphology (e.g., self-cleaning coatings) or internal structure of the fibrous media (e.g., separation/filtration media).

# Chapter 3. Empirical Model to Simulate Morphology of Electrospun Polycaprolactone Mats

## 3.1 Introduction

Electrospinning is a low-capital-cost method of producing micro- or nano-fibers for applications like tissue engineering, particle filtration, membrane desalination, catalysis, self-cleaning, drug delivery, and sensing among many others [1,3,11,12,14,25,80,87,140,141]. A major challenge in fiber electrospinning is the lack of control over fiber orientation or position in the resulting electrospun mats. This makes very difficult to design and produce an electrospun mat with a desired porosity of pore size. It is also quite difficult to accurately measure the thickness, porosity, or surface roughness of electrospun fibrous mats as they are often very thin and soft [87]. Structural simulation can generally be of great help in such conditions, but unfortunately, the complex nature of electrospinning process makes it very difficult to develop an accurate model to describe and predict the outcome of an electrospinning experiment. Yarin and Reneker were the first to develop a mathematical model to simulate the trajectory of an electrospun filament as it leaves the needle until it reaches the collector [33,35,36]. Their model incorporates the contribution of solution flow rate, solution viscosity, relaxation time, and electrical potential in fiber attenuation. The work of Ref. [33,35] was later used to develop subsequent numerical models to include the effects of air drag force or the effects embedded nanoparticles on filament trajectory during electrospinning [43,46,47,50]. Our group also used the work of Ref. [33-35] to simulate formation of a Polystyrene (PS) filament in an electrospinning setup, and use resulting information in an in-house mass-

spring-damper (MSD) model to study the effects of electrospinning conditions (e.g., voltage or needle-to-collector distance) on mat thickness or porosity [15]. In the current work, we improved our MSD algorithm by allowing the fibers to have an in-plane curvature (needed for simulating mats consisting of curly fibers) and also used single-fiber mechanical properties for calibration. The current chapter presents simulation of electrospun PCL fiber-mats as an example of fibrous mats made up of curly fibers. In the current chapter, we also discuss challenges involved in modeling a mat comprised of randomly-distributed curly fibers.

The remainder of this chapter is structured as follows. We discuss our experimental and numerical procedures in Section 3.2 and 3.3, respectively. In Section 3.4 (Results and Discussion), we first obtain fibers' deposition diameters (and velocities) and compare them with their counterpart observed experimentally. We then present a calibration study devised to obtain representative spring and damping constants for our MSD model using experimental data reported for PCL nanofibers. With this information gathered, we generate a series of virtual fibrous geometries comprised of curly fibers and discuss their properties relative to those obtained experimentally. This is followed by our conclusions in Section 3.5.

### 3.2 Experiment

As the main objective of the work presented here was to simulate fibrous mats with curly fibers, we considered Polycaprolactone (PCL) as a suitable polymer for our experiment. The other advantage of using PCL in our study is the availability of experimental data about their mechanical properties (single-fiber data). The PCL was purchased from Aldrich, MO, USA, and it was

reported to have an average molecular weight of 80,000 g/mol. To make a PCL solution suitable for electrospinning, PCL pallets were dissolved in Acetone (ACS grade) mixture with methanol (ACS grade) with a 3 to 1 weight fraction ratio. A conventional electrospinning setup consisting of a syringe pump (New Era Pump System, Inc., Farmingdale, NY) with a 22-gauge stainless steel needle (Jensen Global, Santa Barbra, CA) and a DC power supply (Matsusada High Precision Inc., Shiga, Japan) was used in the experiment, as can be seen in Figure 3.1. We considered a needle-to-collector distance (NCD) of 15 cm, a voltage of 14 kV, and a flow rate of 1 mL/hr. The fibers were deposited on Aluminum foils, and imaged using an SEM microscope (JEOL LV-5610, Peabody, MA). The SEM images were then used to measure the diameter of the spun fibers in the mats (see Figure 3.1) using the ImageJ software, and to obtain a fiber diameter distribution for each mat (75 measurement per SEM image, 3 SEM images per sample).

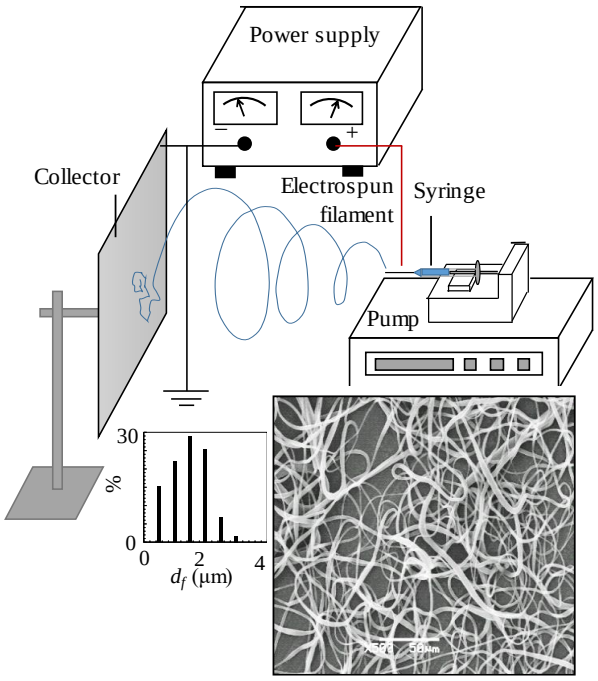


**Figure 3.1:** Our electrospinning setup is shown along with an SEM example and a fiber diameter distribution obtained from the spun PCL mats.

In order to measure the thickness of nanofiber mats, a sample of about 7.5 cm × 2.5 cm in dimensions were cut from the central portion of the mats (deposited on Al foils) and placed between two glass slides using a double-sided tape. The mat thickness was estimated by subtracting the thickness of all other components (two glass slides, aluminum foil, and tapes), measured using a micrometer (Mitutoyo), from the thickness of the entire assembly (See Figure 3.2). Such measurements were conducted on multiple locations across the sample and careful attention was paid to minimize deformation or compression of the samples (though inevitable) during the measurements.

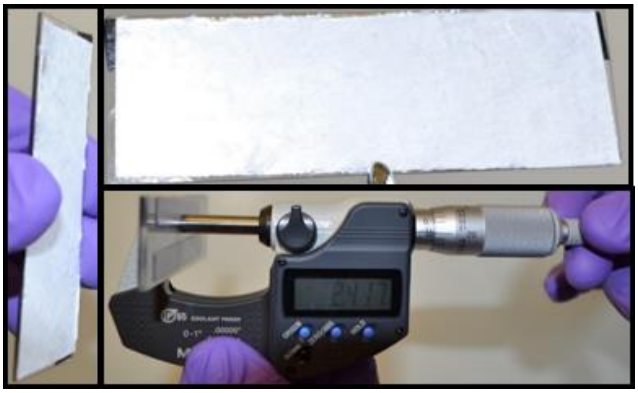

**Figure 3.2**: Using Micrometer to Measure the Thickness.

### 3.3 Numerical Simulation

Our electrospun mat simulations are comprised of two separate steps: 1) fiber formation, and 2) mat generation. For the fiber formation step, we simulate the formation of a PCL filament from the needle via a Python implementation of the model of [33,34]. This was done to obtain the diameter and velocity of the spun fibers at the moment of deposition onto the collector. This information is then used in our MSD mat-generation code to create a 3-D fibrous mat made up of hundreds of such individual fibers deposited on top of one another.

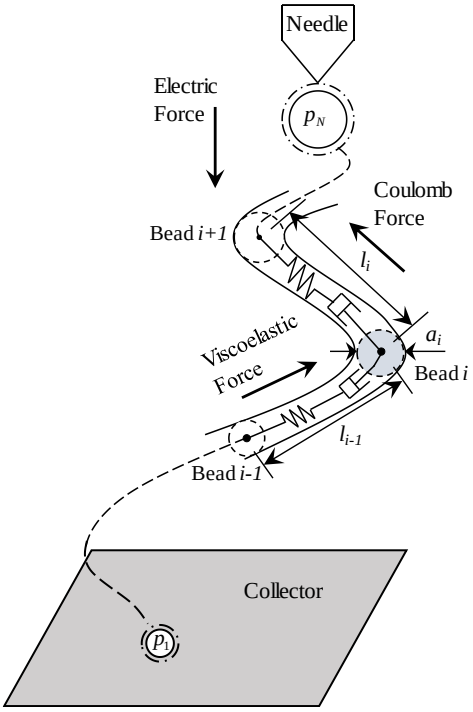


**Figure 3.3:** The fiber electrospinning model of [33,34] is shown. The viscoelastic force $f_{ve}$ and the surface tension force $f_{st}$ point to the fiber's center of curvature to restore the rectilinear shape. The Columbic force $f_c$ sums all the repulsive interactions between the beads. The imposed external electric potential $V_0$ is shown with a vertical arrow.

The algorithm of [33,34] uses the Maxwell viscoelastic concept to model a fiber as it leaves the needle. It treats the spun fiber as an array of beads with volatile (time-dependent) masses interconnected by springs and dampers (viscoelastic elements) in series (see Figure 3.3). The model includes the mechanical (viscoelastic and surface tension) forces as well as the electrical (Columbic and electrostatic) forces (see Figure 3.3). Solving a system of couple ODEs each representing Newton's 2nd law written for a bead in the fiber results in the instantaneous position and velocity of the beads constituting the filament during their needle-to-collector travel. The model of [33,34] also includes the evaporation of the solvent during the fiber formation which is important in obtaining accurate estimate for the final diameter and velocity of the fiber before

reaching the collector. The fiber formation simulations start with two beads initially (to make the first filament segment). Throughout the simulation time, beads will continuously be ejected from the needle (a bead is ejected as soon as the distance between the last bead and the needle becomes greater than 0.05% of the NCD) and tracked until the first bead reaches the collector at $z = 0$, where the simulation stops. The mathematical equations for the fiber formation steps are not presented here for the sake of brevity, but they can be found in [33-35] or our recent work on modeling electrospun Polystyrene [15]. Table 3.1 provides the input values needed to use this model to simulate PCL fibers.

Table 3.1: Input parameters for PCL electrospinning simulation.

| Model input | Value |
|---|---|
| Density $\rho$ | 1.145 kg/m$^3$ |
| Fiber diameter at the nozzle $a_0$ | $15\times10^{-3}$ cm |
| Charge density $e$ | 8.48 g$^{1/2}$cm$^{3/2}$/s |
| Surface tension $\alpha$ | 35 g/s$^2$ |
| Applied voltage $V_0$ | 14 kV |
| Flow rate $q$ | 1 ml/h |
| Elastic modulus $G$ | $12\times10^6$ g/cm s$^2$ |
| Relaxation time $\theta$ | 15 ms |
| Needle to collector distance $H$ | 15 cm |

Our MSD mat-generation algorithm creates realistic 3-D fibrous structures via a sequential deposition of fibers on top of one another [15,95]. The model is based on treating the fibers as an array of beads connected to one another with springs and dampers arranged according to the

Kelvin-Voigt model [15,95,96]. Writing Newton's 2nd law for each bead in the fiber, we obtain (see Figure 3.4a),

$$\vec{f}_i^{\Sigma} = \vec{f}^{s}_{i,i-2} + \vec{f}^{s}_{i,i-1} + \vec{f}^{s}_{i,i+1} + \vec{f}^{s}_{i,i+2} + \vec{f}^{d}_{i,i-2} + \vec{f}^{d}_{i,i-1} + \vec{f}^{d}_{i,i+1} + \vec{f}^{d}_{i,i+2} + \vec{f}_i^{C} \quad (3.1)$$

where $\vec{f}^{s}_{i,i+1}$ and $\vec{f}^{d}_{i,i+1}$are the forces due to springs and dampers on bead ith. The outputs (deposition velocity and fiber diameter) from the fiber formation simulation are used as inputs to the mat generation code. The instantaneous position and velocity of the beads in a fiber can be obtained by numerically (Runge–Kutta 4th order) solving the system of coupled ODEs that results from writing Equation 3.1 for every bead in the fiber. The uniqueness of this model is that it is capable of simulating the curvature of the fibers at the fiber–fiber crossovers without allowing the fibers to penetrate into one another, which is a major advantage over the previous fiber-mat generation methods [97-104,117-120,142].

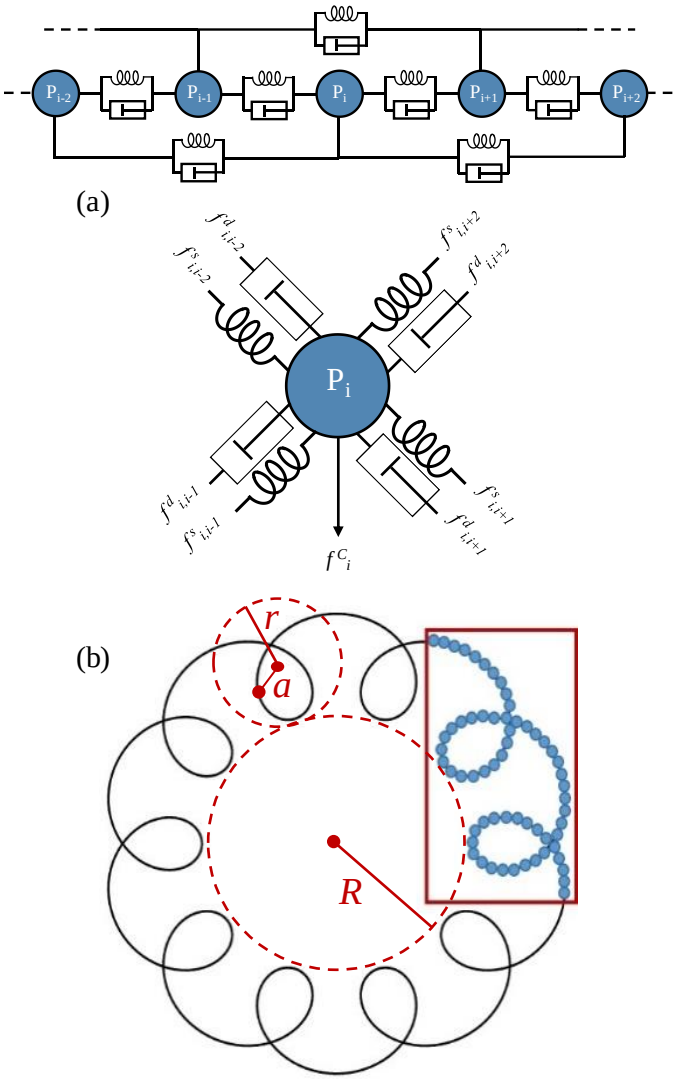


**Figure 3.4:** Our MSD model is shown in (a) [95]. The Spirograph profile is shown in (b) and it consists of a larger stationary circle, with a radius of *R*, and a smaller rolling circle, with a radius of *r*. The parameter *a* is shown in (b).

As mentioned earlier, the straight-fiber restriction is removed from the mat generation algorithm in the present work. This allows us to create 3-D microstructures that better resemble that of an electrospun mat comprised of curly fibers (e.g., the PCL fibers shown Figure 3.1). There are however many challenges involved in simulating a fibrous mat when the constituting fibers are not straight [143]. The first and foremost is the lack of any form of mathematical equations that

can describe the curvature of the fibers in mats like the one shown in Figure 3.1. In the absence of such information, one can only assume an arbitrary shape for the fibers, and hope that the end results (the average properties of the simulated mats agree with those obtained from measurements). To this end, we considered the Spirograph profile for the fibers based on an earlier suggestion [89]. Equations 3.2 and 3.3 represent the x and y positions of each point on the adopted Spirograph profile (Figure 3.4b), respectively.

$$x_i(t) = (R + r)\cos\left(\frac{r}{R}t\right) - a\cos\left(1 + \frac{r}{R}t\right) \tag{3.2}$$

$$y_i(t) = (R + r)\sin\left(\frac{r}{R}t\right) - a\sin\left(1 + \frac{r}{R}t\right) \tag{3.3}$$

The numerical values considered for Equations 3.2 and 3.3 will be discussed later in Section 3.4. Note that, while a more reasonable choice for R would have been a value closer to the actual x-y dimensions of the mats from experiments (i.e., 5–10 cm), that would have increased the size of the simulations (and so the simulation CPU time) by orders of magnitude for no clear gain, as the radius r would have still been an arbitrary value.

The dynamics of fibers depositing on top of one another (and bending at the fiber–fiber crossovers) can be simulated through solving a system of coupled differential equations similar to the one given below,

$$\frac{d}{dt}\begin{bmatrix} v_i \\ \vec{r}_i \end{bmatrix} = \begin{bmatrix} \vec{f}_i^{\Sigma}/m_i \\ v_i \end{bmatrix} \tag{3.4}$$

Stiffness for an ordinary differential equation is a time-consuming problem that occurs when some components of the solution decline much more rapidly than others [144], so the numerical method must take small steps and self-error check to obtain satisfactory results [145]. An in-house C++ computer code has been developed to solve the coupled Ordinary Differential Equations (ODE's).

'Odeint' library is used for numerically solving ODE's. The numerical algorithms are implemented in the code. The system of ODE's in Equation 3.4 is solved using the Runge-Kutta-Dopri5 (Dormand-Prince 5 algorithm) method with a time step of $2 \times 10^{-6}\ \mu s$ and it obtains from trial-and-error method to avoid the stiffness issue (Simulation is done for $2 \times 10^{-3}\ \mu s$ that did not converge). Runge-Kutta-Dopri5 is the standard method with error control [146]. The simulation for larger time steps does not converge and could not predict the collision. Our collision detection algorithm searches for a collision between the beads in a new incoming fiber and those of the deposited fibers in the mat. The distance could not be less than 0.001 μm. The incoming fiber gets affected by the collisions and bends and deforms as needed but the deposited fibers are immobile (do not move or deform regardless of the impact force exerted on them by the incoming fibers).

### 3.4 Results and Discussion

Starting with the results from electrospinning simulations, Figure 3.5a presents snapshots of our fiber formation simulations for an electrospun PCL fiber produced at the same spinning conditions as the experiments (a voltage of $V_0 = 14$ kV, a NCD of $H = 15\ cm$, and a PCL concentration of $C = 15\ wt\%$ , see Section 3.2). Figure 3.5b shows the filament's radial and axial velocity profiles (velocities across the length of the filament from the needle to the collector). Note the axial disposition velocity of the fiber (circled in the figure), as it will later be used in our mat simulation.

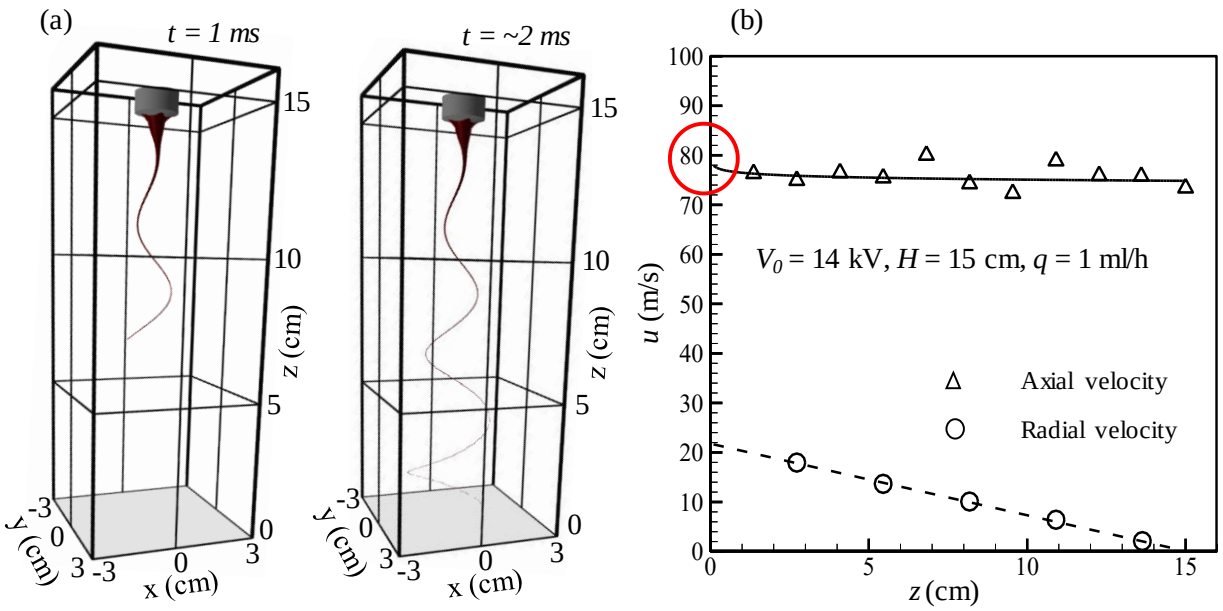


**Figure 3.5**: Examples of our PCL trajectory simulations is in (a) at two different simulation times. Filament's local velocity profiles (beads velocity) is given in (b).

Figure 3.6a shows the filament diameter as it travels from the needle to the collector. It can be seen that filament diameter reduces from about 70 μm to about 1 μm due to the combined effects of solvent evaporation and mechanical stress along the filament. The results shown in Figure 3.6a are in qualitative agreement with the work of Ref. 147 who modeled the polymer jet flow to study the effects of air flow on filament diameter. Figure 3.6b shows the effects of PCL concentration of the final filament diameter (diameter of the electrospun fibers). We have also included experimental data (from SEM images) obtained for PCL mats produced from solutions with different concentrations. Good general agreement can be seen between the predicted and measured fiber diameters. The increase in the fiber diameter as a result of increasing polymer concentration is in qualitative agreement with the experimental work of [124-126].

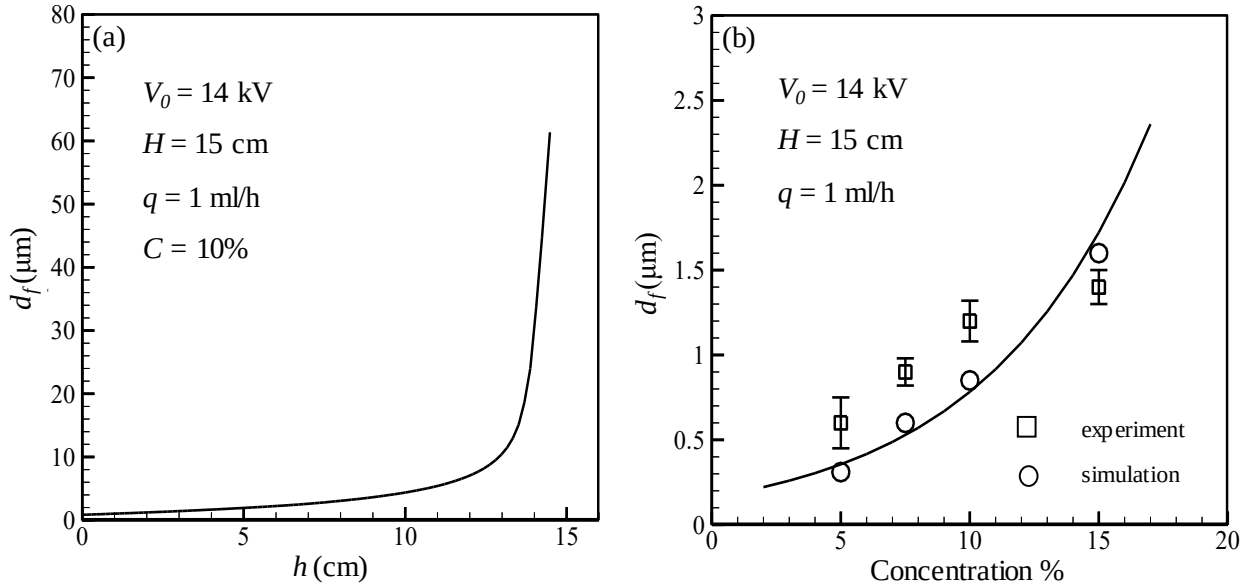


**Figure 3.6**: Filament's local diameter profiles (beads diameter) is given in (a). Average fiber diameter is shown versus PCL solutions concentration (b). Experimental data are also added from electrospinning PCL with flow rate of 1 ml/h, applied voltage of 14 kV, and a NCD of 15 cm.

The experimental data reported in [148] for the bending of a single PCL nanofiber, mounted on a TEM grid with a spacing of 10 μm (see force-deflection data in Figure 3.7a), are used here to calibrate the stiffness of the fibers in our model in this work. To do so, we considered a fiber with the exact same diameter (420 nm) as the one used in the experiment of [148], and fixed it between two rigid support 10 μm apart.

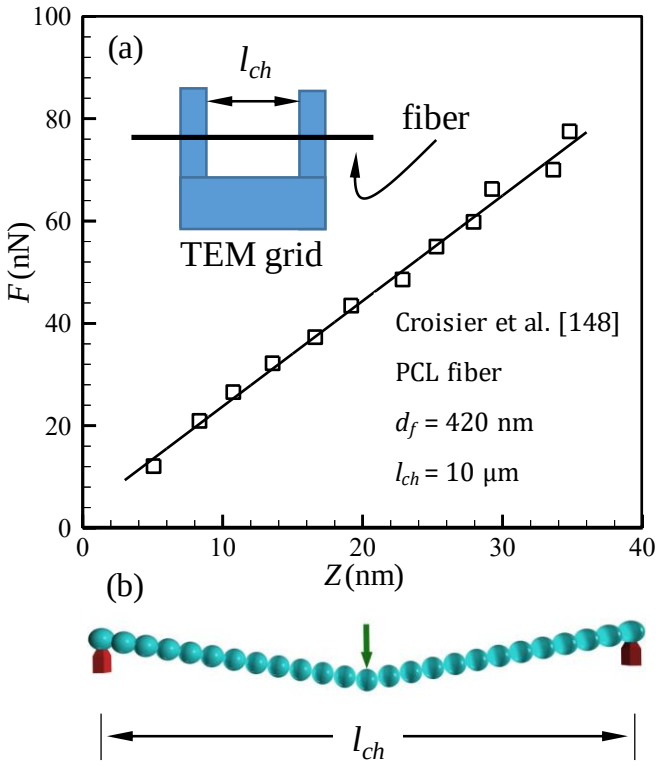


**Figure 3.7:** Force-deflection data taken from the single-fiber experiment of **[148]** are shown in (a). Our computational counterpart of this experiment is shown in (b).

To simulate the force applied to the fiber by the AFM microscope tip in [148], we applied a local downward force to the bead in the middle of the fiber (see Figure 3.7b). Considering three different damping constants but varying spring constants, we obtained different force-deflection data from our single-fiber simulations (see Figure 3.8). The damping $\kappa_d$ and spring $\kappa_s$ constant combination that resulted in the same force-deflection slope as the one measured experimentally, was considered in our simulations.

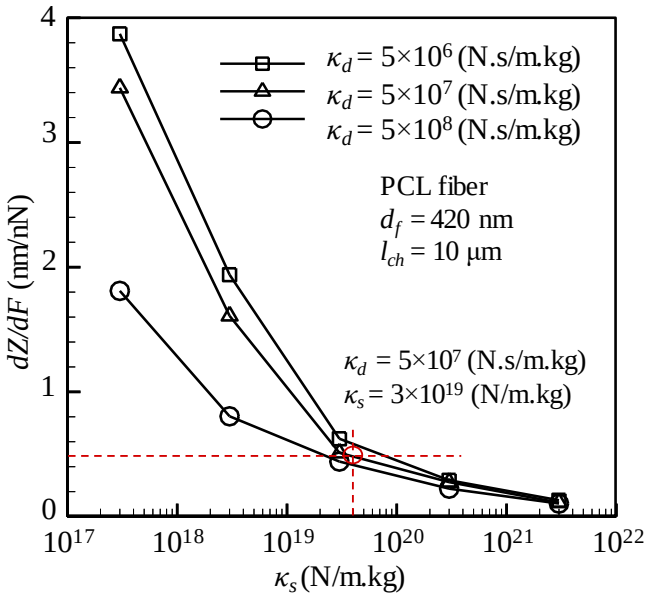


**Figure 3.8:** The damping and spring constants resulting in a force-deflection slope matching that from experiment of [148] are located with red dotted lines.

Figure 3.9a shows an $1mm \times 1mm$ example of our virtual mats with a basis weight of $2\,g/m^2$ comprised of curly PCL fibers with a fiber diameter of $d_f = 0.8\,\mu m$ (fibers deposition velocity and diameter were obtained from the fiber formation simulation of Figure 3.6). Using the relationship given in our previous work in [95], the spring and damping constants obtained in Figure 3.8 for a fiber with a diameter of 420 nm are scaled to $\kappa_s = 5 \times 10^{18}\,N/m.kg$, and $\kappa_d = 8 \times 10^6 N.s/m.kg$ for a fiber with a diameter of $d_f = 0.8\,\mu m$. An SEM image showing our PCL mats from a somewhat isometric view is also included in this figure to better show the roughness of the mat surface (Figure 3.9b). The average thickness and average porosity of the virtual PCL mat shown in this figure were found to be $28.8\,\mu m$ and 93%, respectively. Figure 3.9c also reports the dimensionless thickness (divided by basis weight, multiplied by PCL density of $\rho$ = 1145 kg/m$^3$) and porosity values for our simulated PCL mats versus fiber diameter. Experimental

thickness and porosity values are also added to this figure for comparison. Our results show that increasing fiber diameter decreases the porosity of the resulting mat but by a small amount. As mentioned earlier, in the absence of quantitative information about the shape and curvature of curly fibers in a PCL mat, one has to consider arbitrary values to be able to proceed.

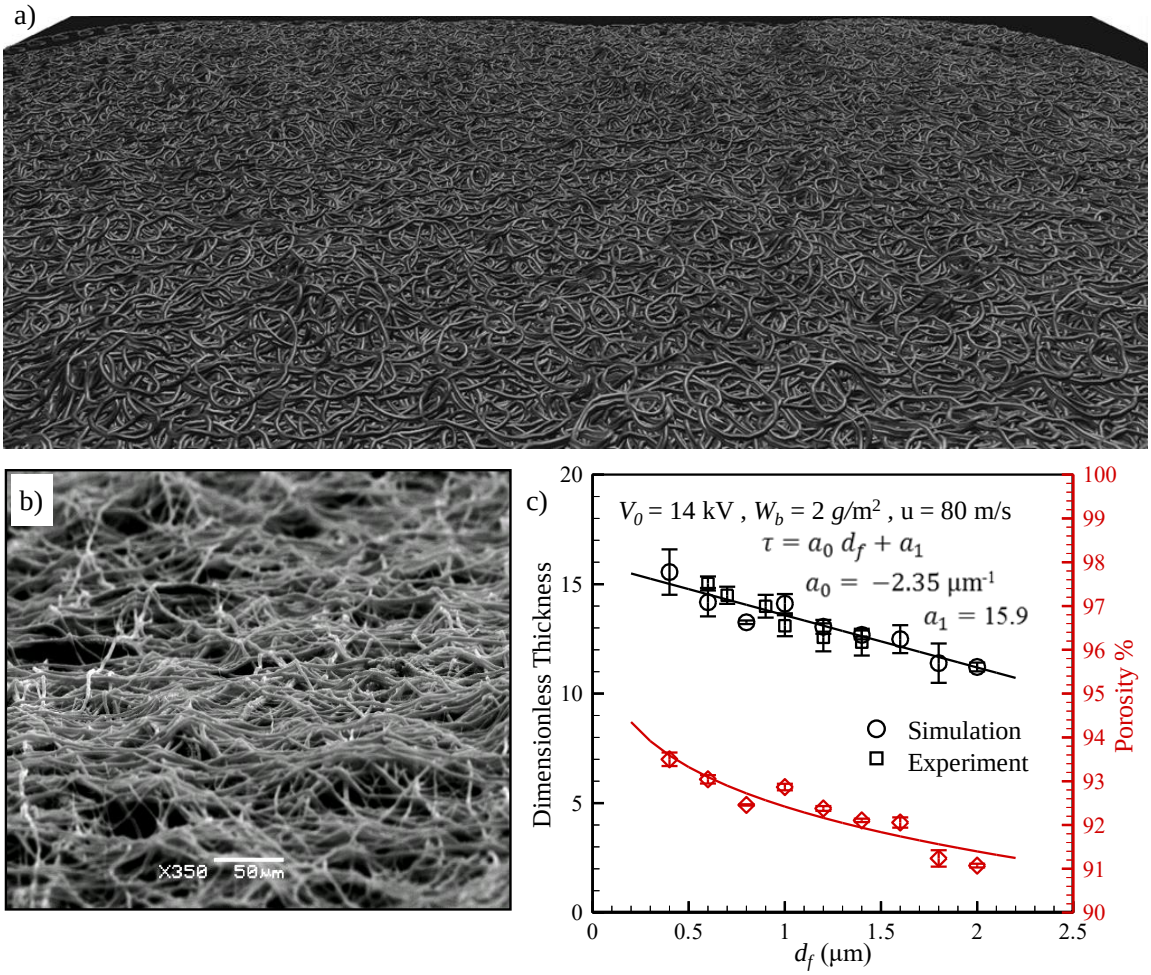


**Figure 3.9**: A sample virtual mat with a basis weight of 2 $g/m^2$ made of fibers with a diameter of 0.8 µm is shown in (a) along with an SEM image PCL mat electrospun with a voltage of 14 kV, NCD of 15 cm, and a flow rate of 1 ml/h in (b). Predictions of our calibrated code for the effects of fiber diameter on porosity and dimensionless thickness are given in (c), and are compared in their experimental counterparts.

In this work, we considered R = 60 μm, r = 10 μm, and a = 16 for our simulations as they provided matching agreement with experimental data (found through trial-and-error). Obviously, there can be many other combinations of *R*, *r*, and *a* (or even other fiber curly profiles) that can result in mats with the same average thickness or porosity. These values are only examples of such input values and considered to limit the CPU time required for the simulations (large *R* values require longer CPU times). Using these empirically-obtained parameters, we used our calibrated code to study the effects of voltage and NCD on mat porosity and thickness. To do so, we first calculated the effects of voltage and or NCD on the final fiber diameter and deposition velocity, and then used this information in the calibrated mat code to generate 3-D virtual mats and obtain their average porosities.

Our simulation indicates that increasing DC voltage from 10 kV to 25 kV increases the fiber diameter and deposition velocity by about 250% and 100%, respectively (Figure 3.10a). This seems to be due to reduction of the time of travel (leaving insufficient time for evaporation to further reduce the fiber diameter) as a result of increasing the attraction force on the fiber. Note that both the increase and decrease of fiber diameter with voltage have been reported in the literature for certain polymers (e.g., [48,116,125,135,137,149]).

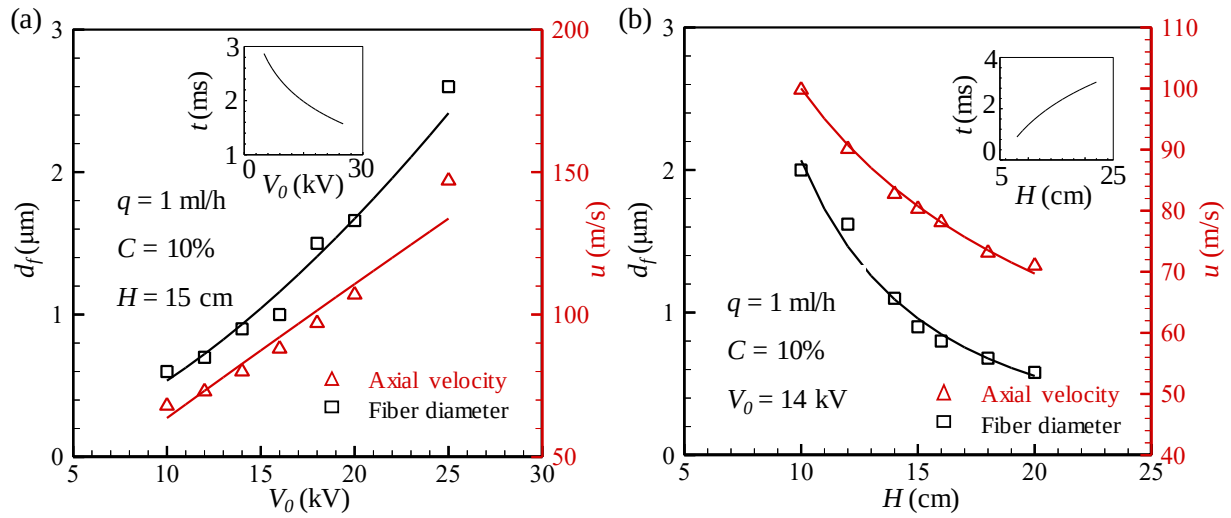


**Figure 3.10:** Fiber diameter and fiber deposition velocity obtained from simulating PCL fibers are shown in (a) and (b) versus voltage and NCD, respectively. The inset figures show the fiber's time of flight.

With regards to NCD, it has generally been reported that increasing the working distance would result in a decrease in the fiber diameter (and so an increase in the mat thickness) [48,116,125,135,137,149]. This has also been observed in our simulations (Figure 3.10b), and can be explained considering the extended time of travel (or solvent evaporation time).

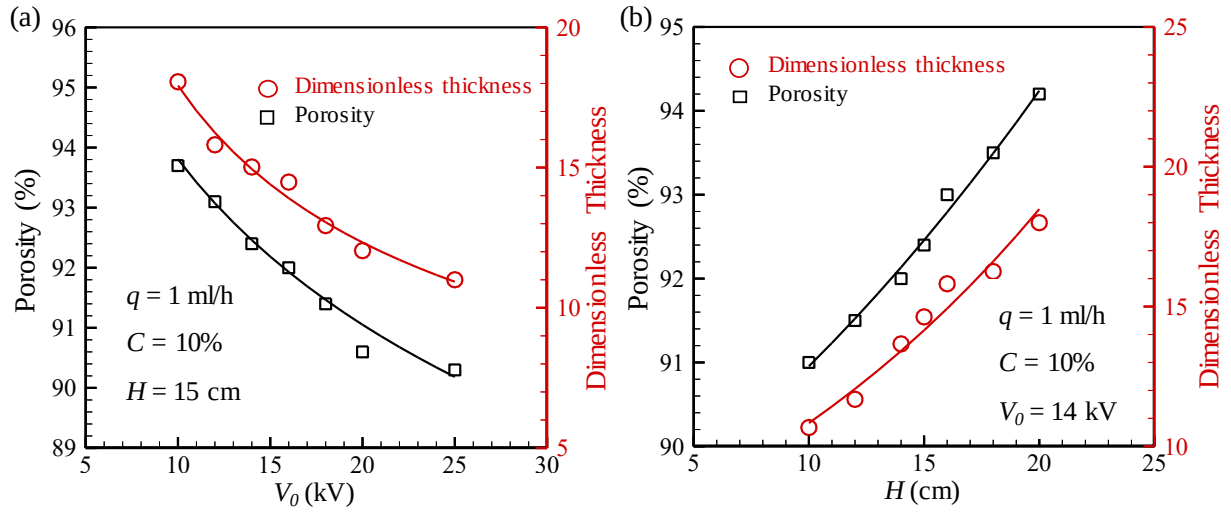


**Figure 3.11:** Porosity and dimensionless thickness are shown in (a) and (b) for the virtual PCL mats, using information shown in Figure 3.10, respectively.

Figures 3.11a and 3.11b show the effects of DC voltage and NCD on porosity and dimensionless thickness of PCL mats. It can be seen that mat porosity tends to decrease with increasing the voltage but increases with increasing NCD in accordance with the effects of these parameters on fiber diameter (Figures 3.10a, 3.10b, and 3.9).

### 3.5 Conclusions

Treating the fibers in an electrospun fibrous mat as an assembly of straight fibers is an acceptable approximation and it has been considered in many previous models aimed to simulate the 3-D microstructure of a fibrous material. In this work however, we have considered curly fibers in producing virtual fibrous media, for the first time. In the absence of a universal definition for the shape of a curly fiber, we have considered an epitrochoid-like profile based on [89]. With their deposition diameter and velocity obtained from simulating the electrospinning process, these curly fibers were stacked on top of one another to create non-penetrating 3-D fibrous mats with geometries that resembles the microstructure of an actual PCL nonwoven mat in many ways. The simulation method presented here allows one to study the effects of voltage, needle-to-collector distance, or polymer concentration on the morphology of the resulting electrospun PCL materials. Numerical results from our experimentally-calibrated simulations indicate that increasing the voltage or decreasing the needle-to-collector distance increases the diameter of the resulting fibers but decreases the porosity of the fiber-mats.

The structure generation method developed in this work allows one to create 3-D virtual fibrous geometries to simulate the flow of fluids or particles through fibrous membranes or to simulate their mechanical properties.

# Chapter 4. Modeling Electrospun Fibrous Structures with Embedded Spacer Particles: Application to Aerosol Filtration

## 4.1 Introduction

Electrospinning is a one-step method to produce a fibrous material by simply dissolving a polymer in a chemical solvent and electrifying the resulting solution through a needle **[**140,150**]**. An intriguing attribute of the electrospinning process is the possibility of varying the spinning conditions or the concentration of the polymer solution to produce a combination of fibers and beads through promoting or preventing the breakup of the electrified polymer jet (e.g., [72-74,151-155]). More specifically, one can often go from a fiber-only morphology to a fibers-and-beads or to a beads-only morphology by varying the polymer concentration, DC voltage, needle-to-collector distance (NCD), and/or polymer flow rate (see e.g., [72-74,151-155]). Electrospinning can also be used to embed external particles inside (e.g., **[**63,64,156,157**]**) or between (e.g., **[**158–159**]**) the fibers to incorporate additional functionalities in a fibrous material (the latter is often achieved via simultaneous electrospinning–electrospraying). The particles trapped between the fibers can also provide structural benefits to a fibrous material. These particles, for instance, can serve as "spacers" between the fibers and help to increase the porosity of an electrospun material, and thereby improve its performance in applications like tissue engineering **[**160**]**, particle or droplet filtration/separation **[**161**]**, or water desalination **[**162**]** among many others.

Generating virtual fibrous geometries that resemble the 3-D microstructure of a fibrous material has proven to be valuable in design and development of nonwoven media for applications like aerosol filtration [84,104,120], fluid transport [101,163,164], heat insulation [103,165], or modern textiles in general [96,166,167]. The current work is the first to report simulation of fibrous structures in presence of spacer particles. As will be discussed later in the chapter, this can only be accomplished with a simulation algorithm that allows a fiber to adjust its shape to the shape of the 3-D objects (e.g., fibers or particles) to which it is in contact, and in doing so, respects the fiber mechanical properties (e.g., stiffness). Needless to say that, the algorithm should detect and prevent any solid–solid interpenetration (obviously non-physical) to occur for the simulations to realistically and accurately represent the morphology of the material.

The remainder of this chapter is structured as follows. We first present our experimental work on electrospinning fibers and beads in Section 4.2, and then move on to discuss our numerical simulations in Section 4.3. In Section 4.4, we present a set of analytical equations that can be used to estimate the collection efficiency and pressure drop of a filtration media comprised of fibers and spacer particles. Our results and discussion are given in Section 4.5, where we present an example for the practical applications of the structure simulation algorithm developed in this work in the field of aerosol filtration. This is followed by our conclusions in Section 4.6.

### 4.2 Electrospinning Polystyrene Beads Embedded in Polyurethane Fibers

Polyurethane (PU) and polystyrene (PS) pallets (from Aldrich, Missouri) with average molecular weights of 550,000 and 350,000 g/mol, respectively, were dissolved in THF (HPLC grade from

Fisher Scientific, Fair Lawn, New Jersey). The solutions were stirred at room temperature overnight until they were macroscopically homogeneous and then were stored at 4°C. The PU and PS solutions were electrospun at a constant rate of 1 ml/h using a conventional electrospinning setup (see Figure 4.1) with a NCD of about 10 cm. The setup was comprised of a New Era syringe pump (Farmingdale, New York) having a stainless-steel needle with an inner diameter of 0.508 mm (Jensen Global, Santa Barbra, California) and a power supply (from Matsusada High Precision Inc., Shiga, Japan) set to a constant DC voltage of 12 kV.

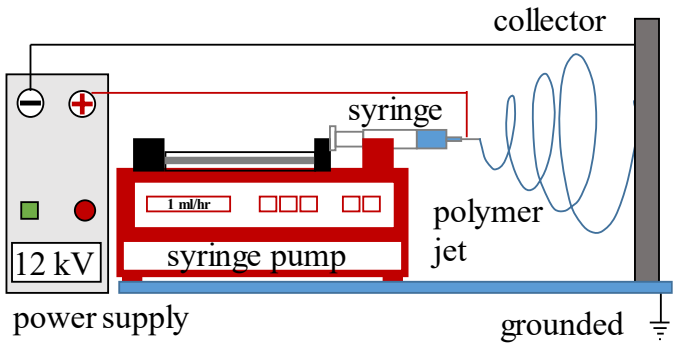


**Figure 4.1:** Schematic of the electrospinning setup used for our experiments.

A concentration of 5% was considered (obtained empirically) for the PU solution as it resulted in bead-free electrospun fibers with an average diameter of about 1 µm. To produce fiber-free PS beads, we used a PS concentration of less than 10%. We also varied the concentration of PS from 5 to 10% to produce PS beads with different average diameters ranging from about 10 µm to about 20 µm (bead diameters were measured from SEM images taken from a 10×10 mm central portion of the area covered by the beads). Alternating between PU and PS depositions, we produced composite bead-embedded fibrous structures comprised of five layers of PS beads embedded in six layers of PU fibers for a total electrospinning time of 40 minutes (30 minutes for the PU fibers

and 10 minutes for the PS beads), as can be seen in Figure 4.2. Note how the PS beads serve as spacer between the some of PU fibers (the SEM images on the left side of Figure 4.2 are from a solution with a PS concentration of 5% whereas those on the right are obtained using 10% PS concentration).

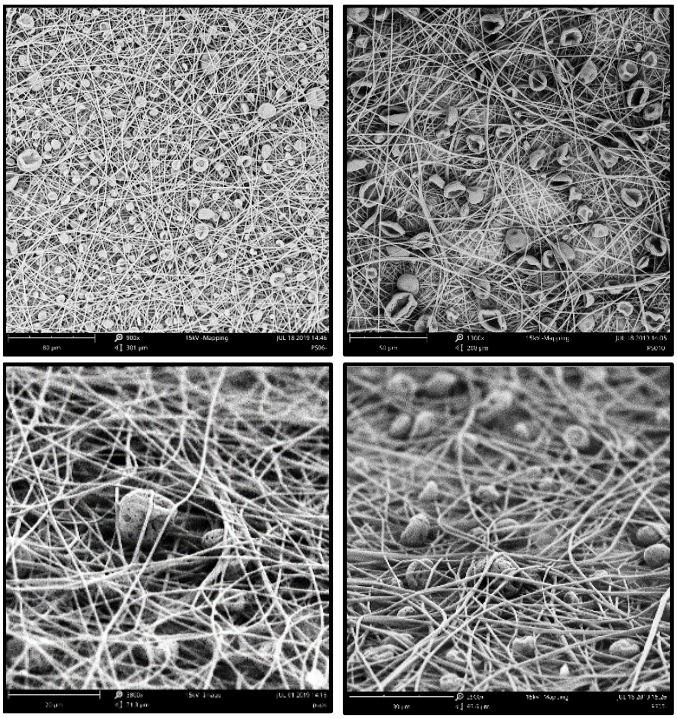

**Figure 4.2:** Selected SEM images of PU–PS mats produced via electrospinning. The mat on the left side are from a solution with a PS concentration of 5% whereas those on the right side are obtained using 10% PS concentration. Note how the PS beads are caged between the fibers.

With the spinning time for each polymer kept constant, we increased the concentration of PS from 5 to 10% (as it was shown to increase the diameter of the PS beads) to study how increasing bead diameter affects the overall thickness of the resulting composite media as can be seen in Figure 4.3. Thickness of the PS–PU composite structures were measured by cutting $7.5cm \times 2.5cm$ rectangular samples from the central portion of the deposition area. These samples were placed

between two microscope slides (with known thickness), and the thickness of the sandwich structure was measured at different locations using a micrometer (from Mitutoyo) to estimate the average thickness of the media. It can be seen that increasing the PS concentration increases the thickness of the media. It is important to note here that increase PS concentration also increases the overall basis weight of the media (results in more material deposition). However, it is not easy (though not impossible) to accurately determine the rate of increase of basis weight with PS concentration, due mostly to the variation of the spatial distribution of the beads in the mat with PS concentration (determining the mass fractions of PU and PS in a composited media requires a more controlled and dedicate set of experiments an is beyond the scope of this work).

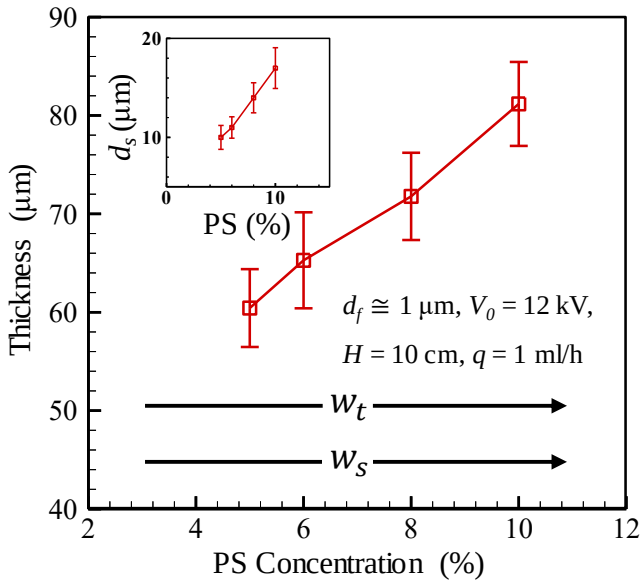


**Figure 4.3:** Thickness of the PU–PS mats vs. concentration of PS in THF (for a fixed PU concentration of 5% in THF). The inset figure shows beads average diameter vs. PS concentration.

### 4.3 Simulating Electrospun Fibers with Spacer Particles

Thanks to the wealth of knowledge in the electrospinning literature, it is now quite easy to setup a conventional electrospinning unit and produce nanofiber materials. However, unfortunately, it is

not easy to accurately predict the outcomes of an electrospinning experiment in terms of fiber diameter distribution or fiber spatial distribution (basis weight distribution) in an electrospun mat. This has served as the motivation for many computational studies, like the pioneering model of Reneker and Yarin **[**33,34**]** or the recent work of Refs. [43,46,47,50]. These models simulate the attenuation of the electrified polymer jet in electrospinning using a virtual array of charged solid spheres connected to one another via springs and dampers according to the Maxwell model (springs and dampers arranged in series to represent the viscoelasticity of the polymer jet). These models consider the mechanical (viscoelastic and surface tension) and electrical (Columbic and electrostatic) forces acting on each sphere (see Figure 4.4a) to produce a system of coupled ODE's each representing Newton's 2nd law for one of the spheres in the polymer jet. Solving this system of ODEs results in the position and velocity of the spheres constituting the jet during its travel from the needle to the collector as a function of time. Interested in knowing the diameter and velocity of the polymer jet (i.e., the fiber) at the moment of deposition on the collector, we implemented the model of Reneker and Yarin **[**33,34**]** in a computer program written in Python language (mathematical equations are not presented here for the sake of brevity, but they can be found in **[**33,34**]** or in our recent work on modeling electrospun Polystyrene **[**15**]**). With this information, we simulated the 3-D structure of electrospun PS and PCL (Polycaprolactone) fibrous mats using an in-house C++ computer program we developed according to the Kelvin–Voigt model (springs and dampers arranged in parallel positions to represent the viscoelasticity of the solid fibers, as shown in Figure 4.4b) **[**15,16,95**].** This model allows one to study the effects of electrospinning conditions or polymer properties on the 3-D morphology of the resulting fibrous materials (modeled as non-interpenetrating flexible fibers with their stiffness incorporated in the model based on their bending characteristics). In this work, we advance the state of art in modeling

electrospun fibrous materials by placing spacer particles of different diameters or populations in between the fibers and thereby studying their effects on the thickness and porosity of the resulting composite structures (equations for the mat generation algorithm are not presented here for the sake of brevity, but they can be found in **[**15,95**])**.

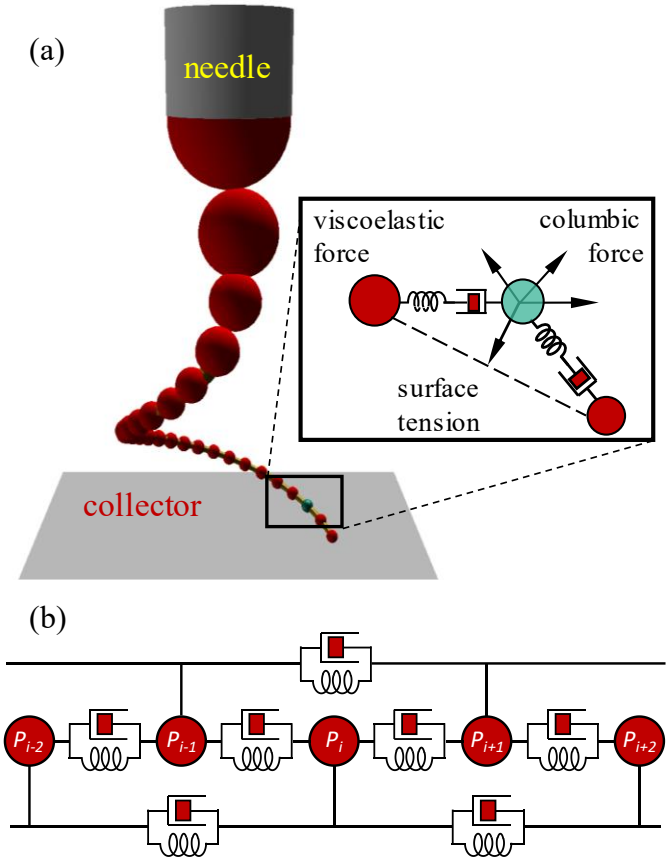


**Figure 4.4:** Mass–spring–damper models used for simulating polymer jet attenuation during electrospinning and for 3-D fibrous mat generation are shown in (a) and (b), respectively.

We start our simulations by first modeling the formation and travel of an electrospun polymer jet from the needle to the collector to obtain the final diameter and velocity of the resulting fiber. We then use this information to model the formation of a fibrous mat comprised of hundreds (or thousands) of such individual fibers deposited on top of one another sequentially. Spacer particles

of given diameters are released in the simulation domain from random locations throughout the fiber deposition process as needed. A major attribute of our mat simulation algorithm is that it allows for the freshly deposited fibers to bend and conform (depending on their stiffness) to the curvature of their underlying solid objects (i.e., previously deposited fibers or spheres). Solid–solid interpenetration is avoided by checking the distance between the spheres at each time step. To simplify an otherwise lengthy calculation, we have assumed the fibers and spacer particles to become un-deformable and unmovable as soon as they are deposited. The basis weight of the fibers and spacer particles are calculated after each deposition to check if the desired basis weights are achieved. Thickness of the virtual mats is estimated by averaging the heights of the top surface of the fibers and particles near the top of the structure. The length of the fibers is calculated by summing up the distance between consecutive spheres along the length of the fiber. The total number of deposited fiber and volume of deposited fiber are obtained in the mentioned domain.

Figure 4.5a shows an example of our trajectory predictions obtained for a PU polymer jet in an electrostatic field with a voltage of $V_0$ = 12 kV across an NCD of $h$ = 10 cm. A fiber deposition diameter of 1.2 μm and a deposition velocity of 30 m/s were obtained from this simulation and used in our mat-generation model to produce virtual electrospun PS–PU composite mats with different properties. Figure 4.5b shows a $1 \times 1mm$ example of our PS–PU electrospun media comprised of fiber with a diameter of 1.2 μm, spacer particles with a diameter of 10 μm, and a total basis weight of $W_t = 5\ g/m^2$ (with the basis weight of PU fibers $W_f = 4\ g/m^2$ and the basis weight of PS beads $W_s = 1\ g/m^2$). The dimensionless thickness (defined as thickness divided by total basis weight, multiplied by the average of the material densities of PS and PU) and solid volume fraction (SVF) of the mat shown in Figure 4.5b are 23.1 and 8.1%, respectively.

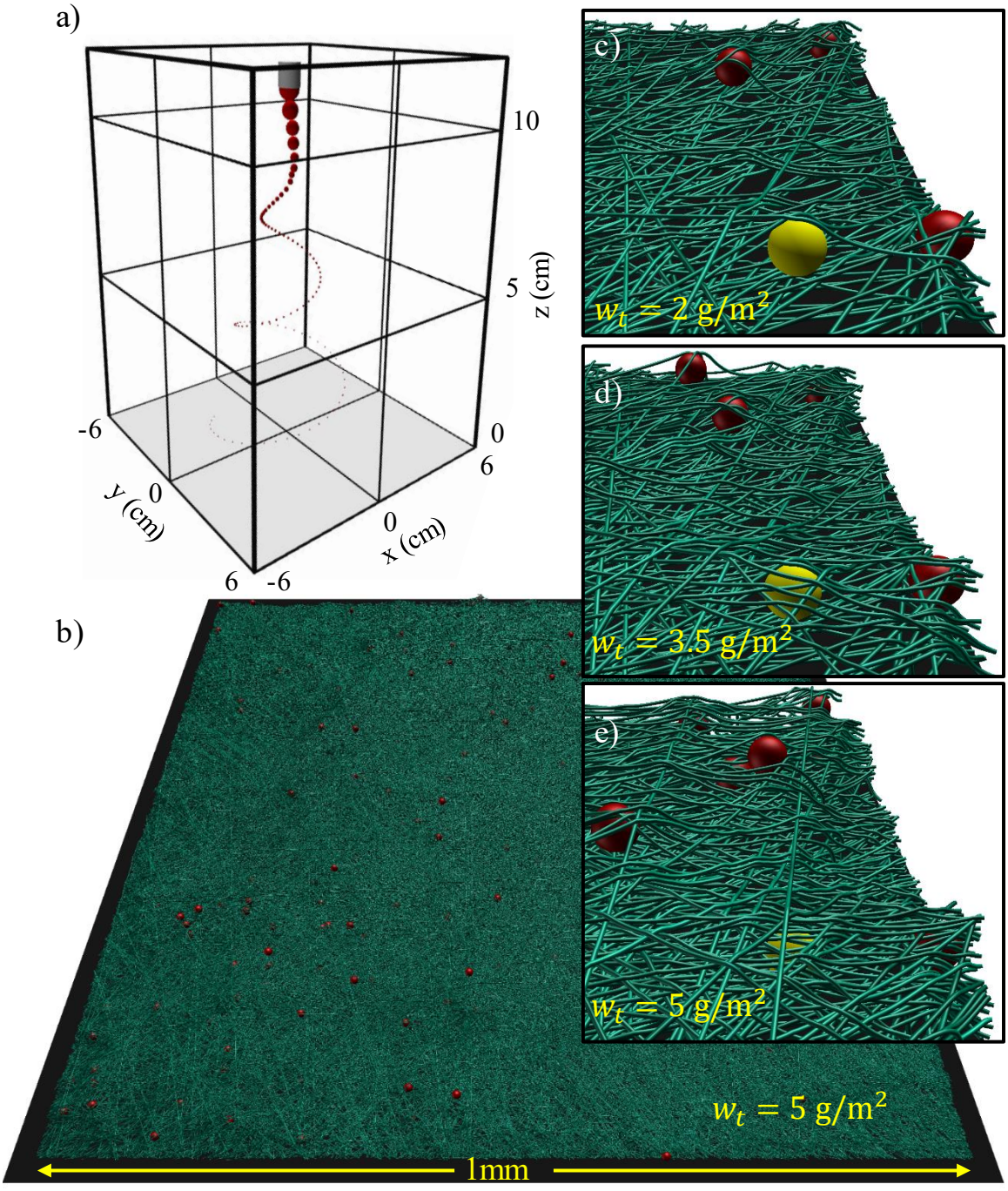


**Figure 4.5:** a) An example of PU jet attenuation simulation (from a solution with a concentration of 5%) is given in (a) for a DC voltage of 12 kV, a NCD of 10 cm, and a solution flow rate of 1 ml/h. An example of our virtual PU–PS spacer-embedded fibrous structures is shown in (b) with fibers having a diameter of 1 µm and a basis weight of 4 g/m$^2$ and beads having a diameter of 10 µm and a basis weight of 1 g/m$^2$. Figures (c), (d), and (e) show magnified views of the upper right corner of the mat shown in (b) during fiber deposition at different basis weights of 2, 3.5 and 5 g/m$^2$.

Figures 4.5c–4.5e show an arbitrary corner of the mat shown in Figure 4.5b at a higher magnification. For illustration purposes, these figures are produced at different basis weights to show how, for instance one, a spacer particle (shown in yellow) is being buried under the fibers as more fibers are added.

### 4.4 Modeling Filtration Performance of Spacer-Embedded Fibrous Media

To present an example for the applications that can benefit from the structure simulation method developed in this work, we study how embedding spacer particles can impact the filtration performance of an arbitrary electrospun filter media, for the first time. For the sake of simplicity, we only consider the initial performance of the filter i.e., the time-dependent effects of dust deposition on filter pressure drop and collection efficiency are not considered (see [168] for more information about modeling dust-loaded fibrous filters).

With the spacer particles having a much smaller total surface area (and number density) than the fibers (see Figure 4.5), it is reasonable to assume (and also confirmed in our preliminary calculations) that they themselves do not make any significant contribution to the collection efficiency or pressure drop of the filter but merely increase the porosity of the fibrous media (hence the name "spacer" not "collector"). Particle filtration efficiency of the filter (spacer-embedded fibrous media) can be estimated using the following expression from literature **[**169,170**]**:

$$E_f = 1 - P_f = 1 - exp\left[\frac{-4\alpha_f E_{\sum,f} t}{\pi(1-\alpha_f)d_f}\right] \quad (4.1)$$

where $\alpha_f$ is the solid volume fraction of filter (defined as the ratio of the volume of the fibers to that of the filter given here as $1mm \times 1mm \times t$). Diameter of the fibers is denoted by $d_f$, and filter thickness is denoted by $t$. ${E_\Sigma}^f$ represents the total single collector efficiency for the fibrous media, and it represents particle collection due to diffusion, interception, and inertial impaction, according to the expression given below [104],

$${E_\Sigma}^f = 1 - \left(1 - {E_D}^f\right)\left(1 - {E_R}^f\right)\left(1 - {E_l}^f\right) \quad (4.2)$$

where ${E_D}^f$, ${E_R}^f$ and ${E_l}^f$ are the single collector efficiencies due to diffusion, interception, and inertial impaction, respectively. There are a variety of expressions for particle collection due to different mechanisms. In this study, we use the equation of Stechkina **[**171**]** for single fiber efficiency due to Brownian diffusion, i.e.,

$${E_D}^f = 2.9Ku^{-1/3}{Pe_f}^{-2/3} + 0.62{Pe_f}^{-1} \quad (4.3)$$

where $Pe_f = \left(U_0 d_f\right)/D$ is the Peclet number and $Ku = -ln\left(\alpha_f\right)/2 - 3/4 + \alpha_f - {\alpha_f}^2/4$ is the Kuwabara hydrodynamic factor. Single fiber efficiency due to interception and inertial impaction is calculated here using the expression proposed by Lee and Liu **[**172**]** and that in ref. [173] given in Eqs. 4.4 and 4.5, respectively.

$${E_R}^f = 0.6\frac{1-\alpha_f}{Ku}\frac{{R_f}^2}{\left(1+R_f\right)} \quad (4.4)$$

$${E_l}^f = \frac{{Stk_f}^3}{{Stk_f}^3+0.77{Stk_f}^2+0.22} \quad (4.5)$$

where $R_f = d_p/d_f$ is the particle-to-fiber diameter ratio, and $Stk_f = \frac{\rho_p d_p^2 C^c U_0}{18\mu d_f}$ is the Stokes number defined using fiber diameter. The particle collection efficiency of a filter comprised on fibers and spacers can now be estimated using Eqs. 4.1–5 (see the next section).

Pressure drop of a spacer-embedded fibrous media is predominantly due to friction between the flow and the fibers. There are a variety of analytical or empirical expressions in the literature for the permeability of a fibrous media (see e.g., [84]). For the current study, we arbitrarily chose the following equation for our calculations

$$k_f(\alpha_f) = \frac{d_f^2}{16\alpha_f}\left[-\left(\frac{1}{2}\right) ln(\alpha_f) - 0.75 + (\alpha_f) - (\alpha_f)^2/4\right] \quad (4.6)$$

where $k_f$ represents the permeability of the fibrous media **[**79**]**. The filter pressure drop can be calculated as,

$$\Delta P = U_0 \frac{\mu}{k_f} t \quad (4.7)$$

**4.5 Results and Discussion**

In this section, we first investigate how addition of spacers with different diameters or number densities (basis weights) can influence the SVF and thickness of a fibrous structures. We then investigate how these effects translate to different filter pressure drop and aerosol collection efficiency values.

Figure 4.6a shows SVF and dimensionless thickness for spacer-embedded media with a constant total basis weight of $W_t = 8\, g/m^2$ having different spacer diameters and basis weights but a constant fiber diameter of $d_f = 3\ \mu m$. It can be seen that thickness of the media increases (and so its SVF decreases) with increasing the basis weight or diameter of the spacers (when the total basis

is kept constant). This is an interesting observation as it is in contrast to the case of bimodal fibrous media comprised of coarse and fine rigid (un-deformable) fibers, where increasing the basis weight of the coarse fibers (or increasing their diameter) decreases the thickness (and so increases the SVF) of the media **[**95**]**. This behavior is in fact similar to that of bimodal fibrous media made up of soft fibers **[**95**]**. This observation is also consistent with the experimental data reported in the literature regarding the effects of bead-to-fiber diameter ratio on SVF of materials produced by electrospinning fibers and electrospraying beads simultaneously **[**79**]** (although ref. [79] does not report much details about the individual basis weights for the beads or fibers). This Figure 4.6a also includes dimensionless thickness and SVF for a filter with no spacer particles (fibrous mat). It can be seen that a purely fibrous media is much thinner and much denser than its particle-embedded counterparts with the same total basis weight.

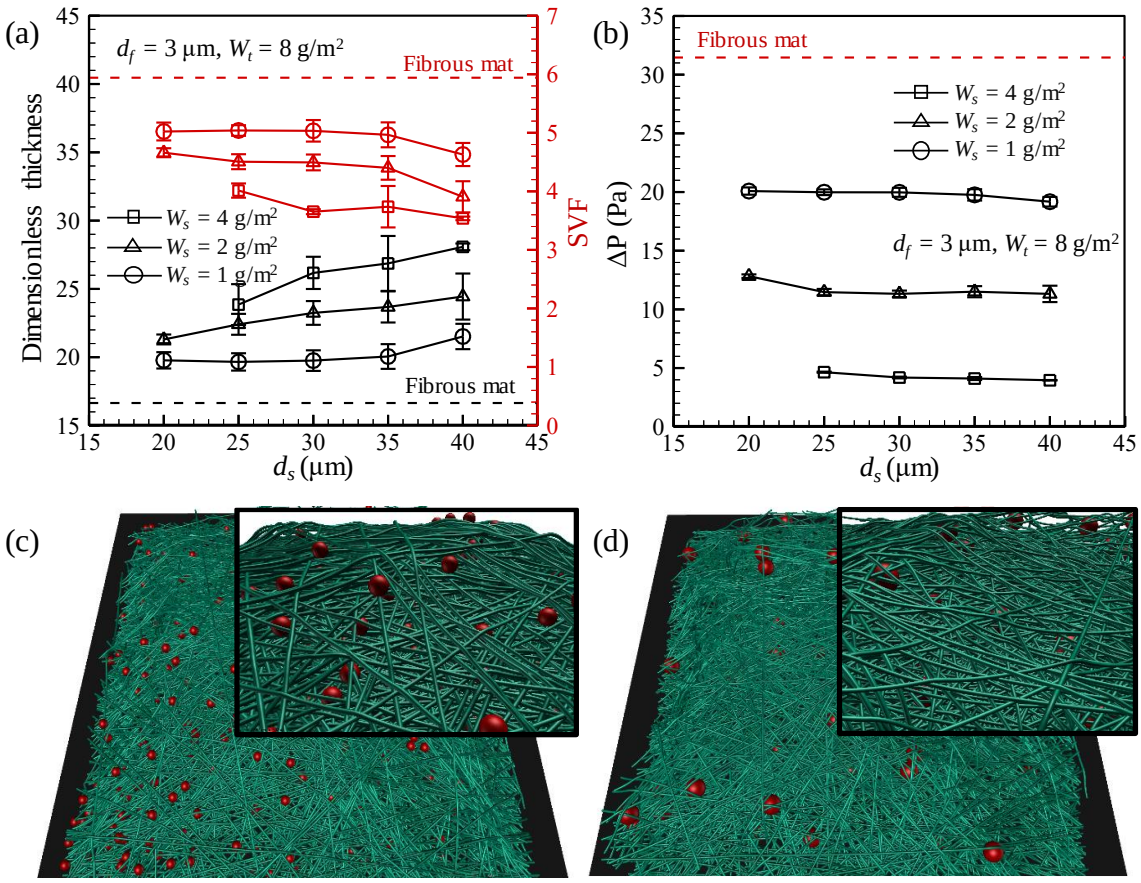


**Figure 4.6:** Dimensionless thickness and SVF are given vs. spacer diameter in (a) for composite filters with a total basis weight of 8 g/m² and a fiber diameter of 3 μm but varying spacer basis weights. Pressure drop values expected from the filters shown in (a) are given in (b) at an airflow velocity of 10 cm/s. Panels (c) and (d) show examples of the simulated PU–PS composite filters with different spacer diameters of 20 μm and 40 μm, respectively. The fiber diameter, total basis weight and spacers basis weight are 3 μm, 8 g/m², and 1 g/m², respectively, for both cases. Dimensionless thickness and SVF were calculated to be 19.4 and 5.1% for the case shown in (c) and 21.9 and 4.5% for that in (d), respectively.

Figure 4.6b shows the pressure drop values expected from the media presented in Figure 4.6a for a face velocity of 0.1 m/s. As can be seen in this figure, a lower pressure drop can be expected from media with a greater spacer basis weight. Likewise, increasing spacer's diameter, for a given spacer basis weight, tend to decrease media's pressure drop. The trends of variation of pressure

drop with spacer diameter and basis weight seem to follow those of SVF in Figure 4.6a. Also, note in this figure that the filter with no spacer particles has the highest pressure drop (as it is less porous). Figures 4.6c and 4.6d show examples of the above virtual media comprised of PS spacers with diameters of 20 and 40 μm, respectively, having a PS basis weight of $W_s = 1\ g/m^2$.

Figure 4.7a shows the collection efficiency of the above media when challenged with aerosol particles with diameters ranging from 10 nm to 5 μm. This figure compares the collection efficiencies of composite media with identical spacer basis weights but two different spacer diameters of 20 and 40 μm. Increasing the diameter of spacer particles, at a fixed spacer basis weight, seem to have a relatively weak effect on the collection efficiency of the resulting composite filter (consistent with how it affects SVF).

As pressure drop of a filter often increases simultaneously with its collection efficiency (but at different rates), it may be difficult to compare filters with different pressure drop and efficiency values. Figure of merit (FOM), also referred to as quality factor *Q*, is often used to gauge the rate of change of pressure drop ($\Delta P$) with that of collection efficiency (presented in terms of penetration, i.e., $1 - E$),

$$Q = \frac{-ln(1-E)}{\Delta P} \tag{4.8}$$

Figure 4.7b presents FOM for composite filters with a fix spacer diameter of $d_s = 40\mu m$ but different spacer basis weights of 0 $g/m^2$ (fibers only) to $4g/m^2$ challenged with aerosol particles with diameters ranging from 10 nm to 5 μm. It can clearly be seen that adding spacer particles

helps to increase the figure of merit of a filter (lowers the pressure more than it lowers the collection efficiency).

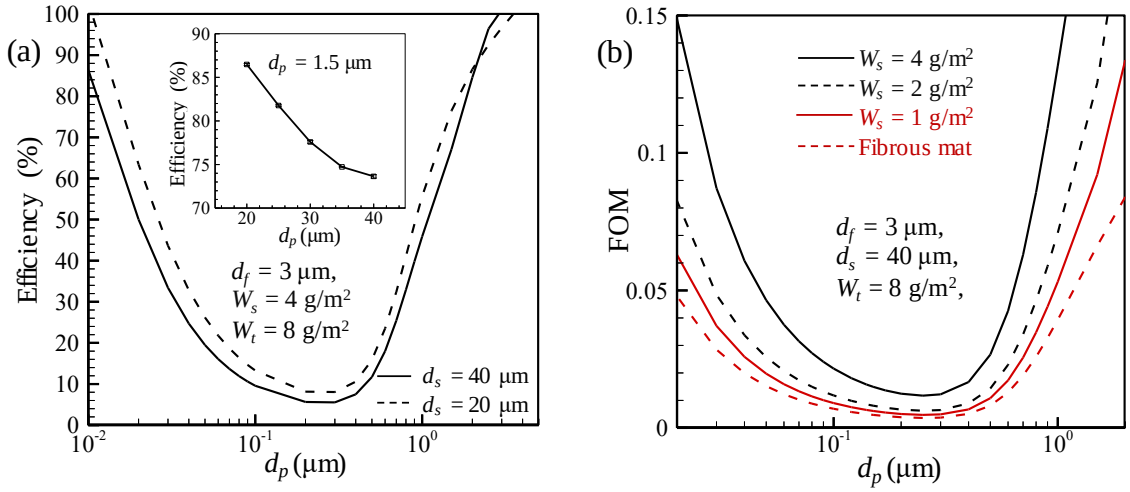


**Figure 4.7:** Collection efficiency predictions against aerosol particles with diameters ranging from 10 nm to 5 μm is given in (a) for media with identical spacer basis weights but two different spacer diameters. FOM for composite filters with a fix spacer diameter but different spacer basis weights is given in (b) vs. aerosol particle diameter.

Figures 4.8a and 4.8b consider virtual composite media having a fiber diameter of $d_f = 5\ \mu m$ but with spacer particles of different diameters and basis weights. The total basis weight for the media shown in Figure 4.8a is $16\ g/m^2$ and for those in Figure 4.8b is $8\ g/m^2$. Same as the case in Figure 4.7, increasing spacer diameter or basis weight in media with a fixed total basis weight and a fixed fiber diameter, tends to increase the thickness (and decrease the SVF) of the resulting media. Comparing the SVF and dimensionless thickness values reported for media with different total basis weights, it can be seen that the above effects are almost independent of the total basis weight of the media.

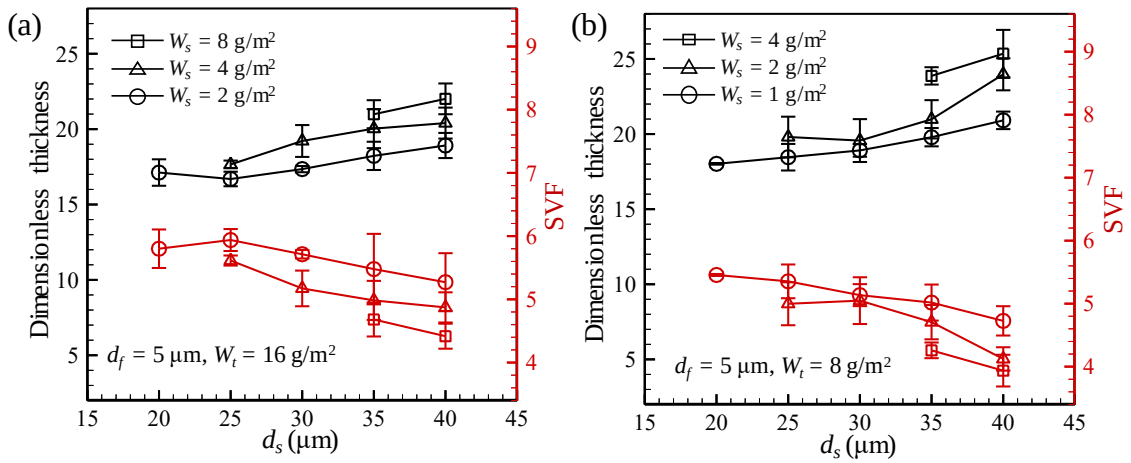


**Figure 4.8:** Dimensionless thickness and SVF are presented vs. spacer diameter for composite filters with different total basis weights of 16 g/m² and 8 g/m² in (a) and (b), respectively. Fiber diameter (5 μm) and spacer basis weight fractions ($W_s/W_t$) are the same in both figures.

Figure 4.9a presents collection efficiency predictions for the above composite filters (spacer basis weight in this figure is one fourth of the total basis weight for each case) against selected aerosol particle diameters of 20 nm (about the lowest end), 200 nm (about the size of most penetrating particles), and 1,500 nm (about the highest end) versus spacer diameter. It can again be seen that increasing the space diameter (or decreasing the overall basis weight of the filter) decreases the efficiency of the composite media. Effects of spacer diameter and basis weight on pressure drop are shown in Figure 4.9b for media with different total basis weights. Similar to the case shown in Figure 4.6b, pressure drop decreases rapidly with increasing the basis weight of the spacer particles but slowly when increasing their diameters (for a constant total basis weight).

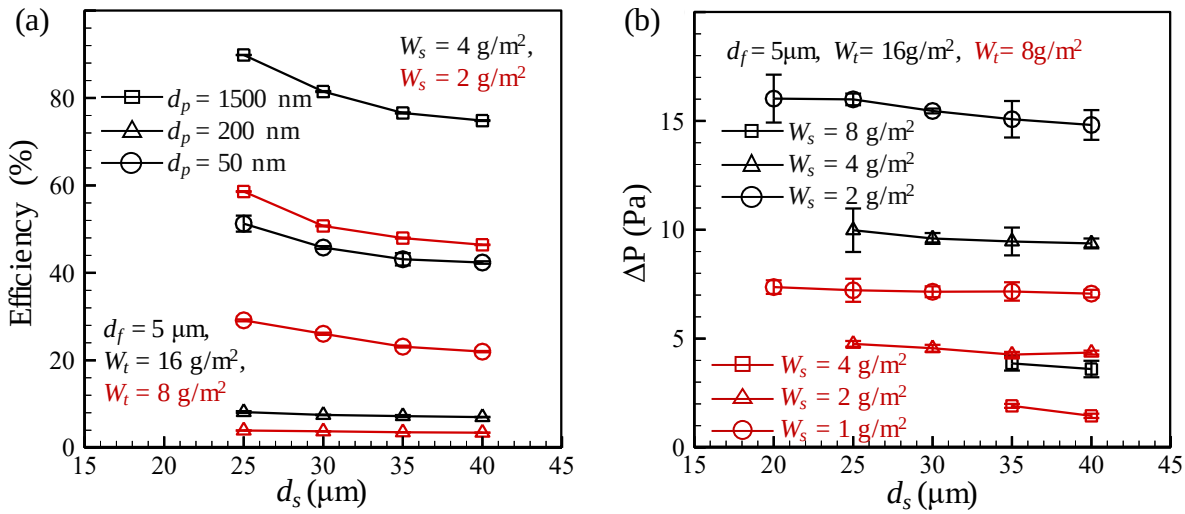


**Figure 4.9:** The effects of spacer diameter on collection efficiency against selected aerosol particle diameters for 2 different total basis weights are given in (c). Pressure drop values expected from the filters shown in (a) and (b) are given in (d) at an airflow velocity of 10 cm/s.

### 4.6 Conclusions

Using the electrospinning process as an example, we demonstrate that one can produce bead-embedded fibrous structures for applications like aerosol filtration, among many other applications. Using an in-house mass-spring damper model that can incorporate the bending rigidity of the fibers (and avoid solid–solid interpenetration), we simulated the 3-D microstructure of such composite media, for the first time. Using available expression in the filtration literature, we predicted the collection efficiency and pressure drop of our virtual spacer-embedded fibrous media. We observed that adding spacer particles (beads in the context of electrospinning, for instance) improves the performance of the resulting filter.

# Chapter 5. Modeling Dust Growth on a Flat Surface: Effects of Particle Shape on Porosity and Thickness

## 5.1 Introduction

Packing dust and particles are not only a fundamental physical and mathematical problem, but also widely involved in industry like filtration and granular membrane. Packing problems have been extensively studied to characterize the structure of material and the properties of particle packing, and arisen in numerous applications [175,187]. One of the concerns in dust packing is predicting of packing density that is a weak point in filtration industries because of increasing pressure drop. Packed dust is included different shape of particle that could have symmetric or complicated shape that have wide range of shapes in 2 different categories: spherical and non-spherical particle.

Numerous studies have been presented on spherical particles packing and characterizing sphere packing with different conditions, such as the binary [177-179] and polydisperse packing [179,180] with a large disparity of size distributions. The most of real particles in industrial applications are not spherical and it raised the idea of simulating the non-spherical particles. The packing investigations of non-spherical particles are more complicated in comparison with spherical objects due to the additional boundaries and complicated surfaces. Some limited works studied limited simple and basic objects, such as ellipsoid [181], spherocylinder [182,183], cylinder [184] and Platonic solids [185]. To characterize the more complicated objects packing, image processing techniques have been developed to predict 3-D packing from computed

tomography (CT) images of realistic particles [107,108]. Numerical simulation on the random packing of non-spherical particles with different sizes or shapes are even rare because of CPU time and computer technology limitations. A number of geometrical and analytical models has been applied in recent studies of limited range of shape and particle's packing [186]. Moreover, different shapes need different models, and no general applicable analytic model has been found. The proposed sphere assembly model is another kind of approximation numerical model for the non-spherical particle packing [186,187]. This model could detect the contacts between the particles more efficient in comparison with previous works but it does not have capability to consider the deformation of non-spherical particles and external body force effects on the packing density.

An accurate method which is able to build wide range of non-spherical particles with good approximation of the real particles is simulation with mass-spring-damper model [95]. These approaches have the ability to simulate particles of any shape. Thus, the collision detection in this model is converted the contacts between non-spherical particles to the penetrations between spheres (simple objects) and saves much time with higher efficiency on simulation of complex objects. Furthermore, the model makes it possible to investigate the external body force effects and the deformation of deformable non-spherical particles among rigid solid different shape of particles. The present study is motivated by a novel method based on mass-spring-damper (MSD) of fibrous structure simulation [15,16,55,95,96]. In previous works, MSD model applied to characterize electrospun mat with studying the viscoelasticity, electrospinning parameters and spherical spacer effects on fibrous structure properties (like thickness, porosity and filtration efficiency). Here, the computational in-house C++ computer program with mentioned MSD model is developed to simulate the 3-D structure of random dust formation for different shape, size and

basis weight of non-spherical particles. Based on the simulation results for different shapes and aspect ratio conditions, we characterize the geometric packing a wide range of non-spherical particles as a function of the shape and size of particles with different aspect ratio. The purpose of this work is to investigate the behavior of particle shape and size effects of the non-spherical particles on the dust formation, further to simulate the dust formation for the first time.

This chapter is organized as follows: we first explain how different non-spherical particles mathematically connected in this model (Section 5.2). Next step, the mass-spring-damoer model and the force balance equation in this model explained. The collision detection algorithm of MSD model explained in detail. Simulation of dust formation presented in Section 5.3. Then, our results and discussion for different parameters are given in Section 5.4 followed by the conclusions in Section 5.5.

**5.2 Non-Spherical Particle Geometry**

The mass-spring-damper (MSD) model to simulate the fibrous structure was firstly developed by Venkateshan et al. [95] to simulate the random deposition of fibers. The algorithm was improved to simulate the random deposition of straight and curly fibers by introducing spherical particles as a spacers [15,16,55]. Here, The MSD model is used in the simulations to model the non-spherical particle and detect the collision between particles. The MSD model of a non-spherical is constructed by a number of masses with center-to-center distances of mass's diameter (The distances between the neighbor masses) that connected with parallel spring and dampers with a direction of X-Y slope ($S_{x\text{-}y}$) and Z-direction ($S_z$) along a straight line. The diameters of all spheres

are arbitrary and to study the effect of size varied from 3 to 15 μm. Aspect ratio shows the ratio between the number of masses along the edge length of objects over by the diameter of one mass. The volume and surface area can be obtained easily from geometry calculation for different simulated non-spherical particles. The model is an excellent approximation to detect the connection and obtain the volume and mass weight of each objects. As an important parameter to describe differences of the particle shape, volume of each object is a function of dimensions and number of point masses and their diameter. The total volume of deposited non-spherical particle given by

$$V_p = N_f \pi {d_p}^2 (n d_p) \quad (5.1)$$

where $N_p$ is the number of deposited particles, $d_p$ diameter of each point mass, and $n$ is the number of point masses for different shapes. Because of the shape of brick, the total volume of deposited brick object given by

$$V_b = N_p \ \mathrm{AR}\ d_p \left(4\ {d_p}^2\right) \quad (5.2)$$

where AR is the aspect ratio of brick. For the simulated objects in this work, number of masses for different shape of particles varies from one to 19 (aspect ratio varied from 2.0 to 4.0). We followed different steps based on the shape of particles that explain in below.

### 5.2.1 Spherocylinder Shape

The spherocylinder particles are constructed by placing at least two point masses next to each other (for aspect ratio of two). Second one placed next to the first random positioned mass with center-to-center distance of diameter of masses. The straight line with the X-Y direction and Z-direction

slope is chosen randomly in the range of -1 to 1 to obtain the in-plane and Z position of neighbor mass. By adding another mass next to it, the aspect ratio of spherocylinder object could be increased. All the connections (straight lines) have a same slope. Figure 5.1 also shows examples of spherocylinder shape represented with aspect ratio of 4 (four point masses that are connected with straight line in an arbitrary direction). The surface of each mass point is obtained by knowing the center point $p_i(x, y, z)$ and the diameter of each point $d_p$. The MSD model and the connection of springs and dampers are presented for more complex shape (brick).

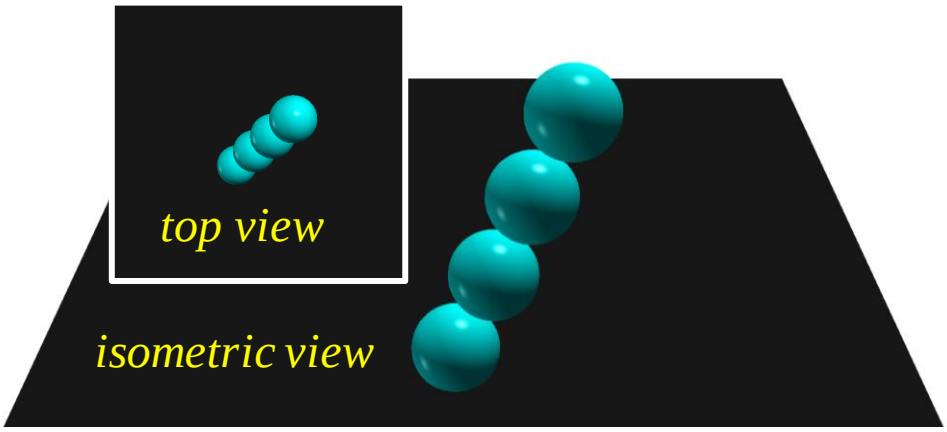


**Figure 5.1**: An example of spherocylinder particles is given for an aspect ratio of 4. Figure shows magnified views of top view and isometric view.

### 5.2.2 Brick Shape

The proposed mass-spring-damper-based (MSD) model provides a versatile description of particles with a broad range of shapes. So, it is also capable to model deformable object (which is not a focus of this study) with different aspect ratio (edge length divided by mass diameter). The capability to simulate solid brick attached the attention to this model. Figure 5.2.a shows the MSD

assembly models of a brick with an aspect ratio of 2.0 included springs and dampers that are connected in parallel order.

As presented in Figure 5.2.a, the number of point masses for the aspect ratio of 2 is 9. The position of first mass is chosen randomly in the computational domain and considered as a corner of cube. The X-Y direction and Z-direction slope are randomly chosen to find the neighbor point mass, next to the first point. $x_2, y_2, z_2$ are the coordinates of the second point at the local coordinate system, which is connected to the first point with straight (known X-Y direction ($S_{x-y}$) and Z-direction slope ($S_z$)) parallel spring and damper with a distance of point mass's diameter. Third point coordinate is obtained in a same way with the X-Y direction perpendicular to the $\overrightarrow{p_1p_2}$ ($-1/S_{x-y}$) with the same center-to-center distance and Z-direction slope. The $p_4$ coordinate is obtained from the known geometric parameters ($-S_{x-y}$, $S_z$ and $d_p$). The below face of cube is modeled from initial random parameters. The cross product of $\overrightarrow{p_1p_2}$ and $\overrightarrow{p_1p_4}$ helps to find the top face of cube. With the obtained vector, the location of 4 other point masses on the top face corner of cube is calculated with the known points on the below face and their cross product vector. To have the sustainable objects with balanced force, the last point placed at the center of cube. The other size of bricks with different aspect ratio could be modeled with adding more plane (4 points each plane) and increased the size of brick in the direction of cross product vector. Example of simulated brick with aspect ratio 2 (cube) is shown in Figure 5.2.b as an example.

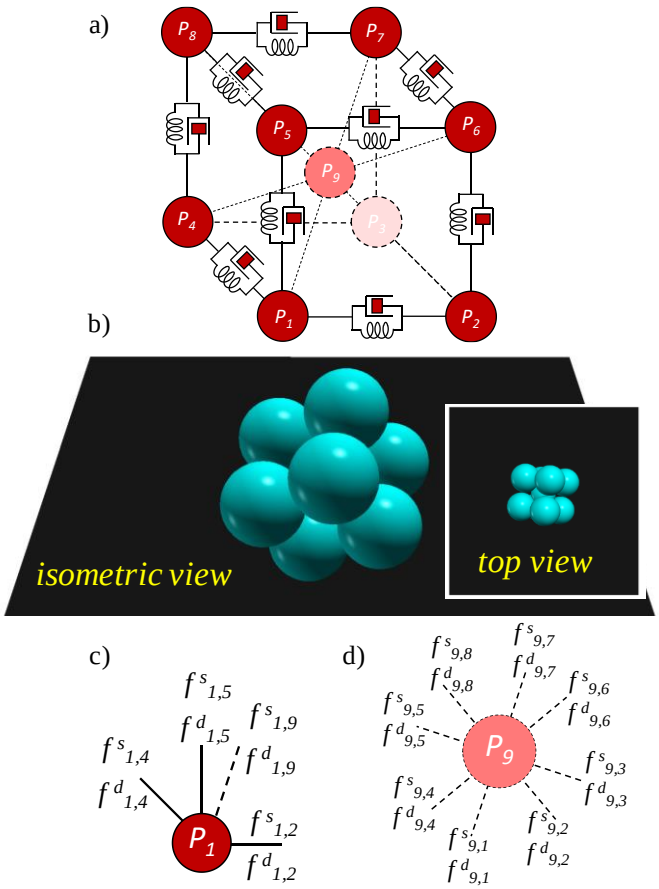


**Figure 5.2**: a) The mass-spring-damper model representation of a brick with aspect ratio of 2 (cube), b) an example of cube. Figure shows magnified views of top view and isometric view, c) free body diagram of a point-mass, $P_1$ (the corner of cube), d) free body diagram of a point-mass, $P_9$ (the center of cube).

### 5.2.2.1 Force Balance Equations for Cube

MSD modeling approach is used here to keep all the non-spherical shapes sustainable. In the current study, we have assumed the particles to be made up of number of masses connected to one another by springs and dampers in a straight line (see Figure 5.2.a). Our approach to simulate a non-spherical shape here is to treat the objects as solid dust. The most common model for solid phase material (the case here) is the Kelvin-Voigt viscoelastic model, where springs and dampers

are connected in parallel [15,16,55,95]. For the high value of spring and damping coefficient the bending and deformation neglected. This model allows an efficient representation of a solid objects through solving the balance of mechanical forces acting on each mass $p_i$. These forces are due to the springs and dampers (neglecting gravitational forces), as shown in the Figure 5.2.c and Figure 5.2.d. The external body forces (packing and hydraulic) are included in our simulations and applied to the all masses. The position and velocity of each mass after several time can be obtained by solving Newton's second law. For a cube with 9 mass, this leads to a coupled system of 2nd order ordinary differential equations (ODEs). From a free body diagram showing the force acting on mass on the corner by the masses to which it is connected, one obtains (Figure 5.2.c),

$$\vec{f}_1^{\Sigma} = \vec{f}_{1,2}^{s} + \vec{f}_{1,4}^{s} + \vec{f}_{1,5}^{s} + \vec{f}_{1,9}^{s} + \vec{f}_{1,2}^{d} + \vec{f}_{1,4}^{d} + \vec{f}_{1,5}^{d} + \vec{f}_{1,9}^{d} + \vec{f}_1^{P} \quad (5.3)$$

In this equation, $\vec{f}^{s}$ and $\vec{f}^{d}$ represent spring and damper forces, respectively, i.e. The last term on the right-hand side of Equation 5.3 is the packing force applied on each mass, and it can be described in packing dust formation. All forces acting on the other points (the corner of cube) could be calculated in a same way. To balance the forces, the center point of cube is connected to all other masses (Figure 5.2.a), the spring and damping force for that one could be obtained from Equation 5.4 (See Figure 5.2.d).

$$\vec{f}_9^{\Sigma} = \vec{f}_{9,1}^{s} + \vec{f}_{9,2}^{s} + \vec{f}_{9,3}^{s} + \vec{f}_{9,4}^{s} + \vec{f}_{9,5}^{s} + \vec{f}_{9,6}^{s} + \vec{f}_{9,7}^{s} + \vec{f}_{9,8}^{s} + \vec{f}_{9,1}^{d} + \vec{f}_{9,2}^{d} + \vec{f}_{9,3}^{d} + \vec{f}_{9,4}^{d} + \vec{f}_{9,5}^{d} +$$

$$\vec{f}_{9,6}^{d} + \vec{f}_{9,7}^{d} + \vec{f}_{9,8}^{d} + \vec{f}_9^{P} \quad (5.4)$$

The system of ODEs in Equation 5.5 is solved using the Runge–Kutta 4th order method with a time step of 0.003 μs.

$$\frac{d}{dt}\begin{bmatrix} v_i \\ \vec{p}_i \end{bmatrix} = \begin{bmatrix} \vec{f}_i^{\Sigma}/m_i \\ v_i \end{bmatrix} \quad (5.5)$$

### 5.2.3 Dandelion Shape

In general, 2 different type of dandelion with different aspect ratio have been simulated here that they have 4 variables in total (number of legs, length of legs, the size and direction of each legs) for modeling an arbitrary dandelion object. Some preprocessing should be done first to obtain a position of masses for dandelion particles with these variables. As be explained in previous section, the first point can be placed with a random $x_1, y_1, z_1$ coordinate in computational domain. The other points, based on the length of dandelion legs would be placed same as making spherocylinder objects (next to the first points with a known parameter's directions and diameter). It's necessary to mention this point that the direction of other legs would be obtained from the first leg direction. The second leg is placed perpendicular to the first leg (The X-Y direction slope of second one is perpendicular $-1/S_{xy}$ and the Z-direction slope is same $S_z$). The point's coordinates on the second legs obtained same as the first one. To simulate the dandelion with 3 legs, the X-Y direction and Z-direction slope of third leg obtained from cross product of the first and second one's directions. The coordinate of points on 3rd one would be obtained as be explained earlier with the known directions and center-to-center distance. Figure 5.3, shows example of the simulated dandelion with 3 legs and the aspect ratio of 3 (length of legs from the center to the end divided by the mass diameter) with the mass diameter of 6 μm.

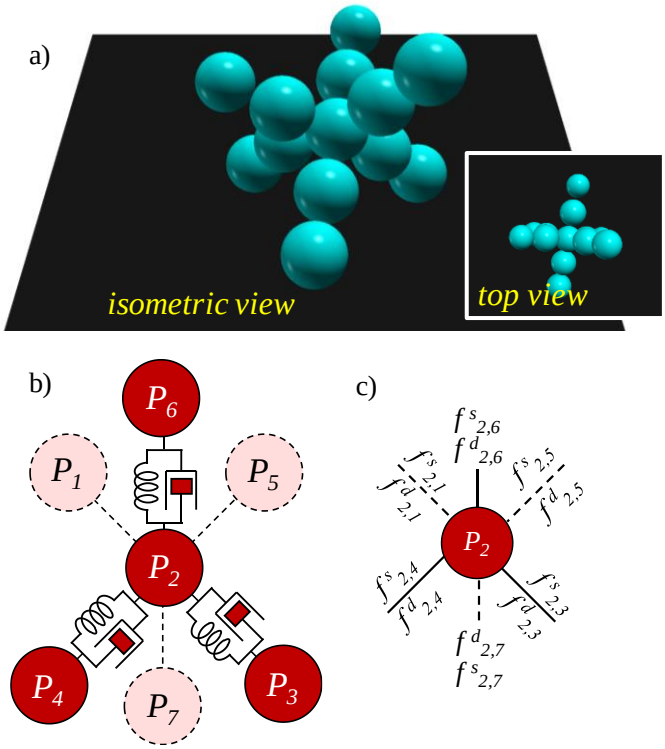


**Figure 5.3**: a) an example of dandelion is given for an aspect ratio of 3. Figure shows magnified views of top view and isometric view, b) The mass-spring-damper model representation of a dandelion with aspect ratio of 2, c) free body diagram of a point-mass, $P_2$.

From a free body diagram showing the force acting on mass $P_2$ by the masses to which it is connected, one obtains (Figure 5.3.c),

$$\vec{f}_1^{\Sigma} = \vec{f}^{s}_{2,1} + \vec{f}^{s}_{2,3} + \vec{f}^{s}_{2,4} + \vec{f}^{s}_{2,5} + \vec{f}^{s}_{2,6} + \vec{f}^{s}_{2,7} + \vec{f}^{d}_{2,1} + \vec{f}^{d}_{2,3} + \vec{f}^{d}_{2,4} + \vec{f}^{d}_{2,5} + \vec{f}^{d}_{2,6} + \vec{f}^{d}_{2,7} + \vec{f}_1^{P} \qquad (5.6)$$

All forces acting on the other points could be calculated in a simple way that presented in previous parts.

### 5.3 Numerical Simulations

The mass-spring-damper method has been implemented in an in-house computer C++ program to simulate different shape of non-spherical particles. In this section, dust packing simulation are

presented to demonstrate the shape of the proposed particles in conjunction with the collision detection algorithm in solving problems relevant to dust formation. First the algorithm for dust packing explained, then the collision detection of our simulation presented in detail.

### 5.3.1 Dust Packing of Non-Spherical Particles

Random packing of dust formation has many useful engineering and industrial applications. A packing of dust growth can be simulated for different shapes, for example, spherical, brick and dandelion. A simulation of dust formation with different shape of particles through free falling without gravity (because of dust size, the mass is negligible) on a substrate is performed using the proposed method in previous sections. In the simulation, number of particles with random orientations are introduced to the media sequentially one-by-one from the highest point of deposited dust, where the x-y of particle shape are randomly selected in the range of as $x \in [-200,200]$, $y \in [-200,200]$ for the mass diameter of $3\,\mu m$ (based on the size of particles the size of collector varies). The material properties of particles are set as follows: the material density is set to $1000\,g/m^3$, the normalized spring and damping coefficient are set to $3 \times 10^{20}\,N/m.kg$ and $3 \times 10^{12} N.s/m.kg$, respectively, and the deposition velocity of particles is set to $10\,m/s$ [15,16]. During the simulation, a time step of $0.003\,\mu s$ are considered. Note that the aforementioned substrate size do matter for the large size of non-spherical particles and dust formation, which deserve a calibration and one should increase the substrate size to reduce the sample size errors on solid volume fraction values. However, the focus is placed on the removing the size errors by increasing computation domain size and also the proposed approach to simulate the wide range of non-spherical shapes with different aspect ratio and collision detection algorithm. Thus, the chosen values of sample size have been based on number of simulations.

Figure 5.4 shows the simulation after introducing 6000 ($10\ g/m^2$), 12000 ($20\ g/m^2$), and 24000 cube with the aspect ratio of 2 and diameter of 6 $\mu m$ to reach basis weight of $40\ g/m^2$. The solid volume fraction and mean thickness are $13.55\%$ and $292.197\ \mu m$, respectively, for the final basis weight of $40\ g/m^2$ and the mass diameter of $6\ \mu m$. The magnified image in Figure 5.4c shows the cube sitting on top of each other. Figure 5.5 also shows the simulation after introducing 4500 ($10\ g/m^2$), 9000 ($20\ g/m^2$), and 18000 dandelion particles with the aspect ratio of 4 and diameter of 6 $\mu m$ to reach basis weight of $40\ g/m^2$. The solid volume fraction and mean thickness are $6.11\%$ and $651.7\ \mu m$, respectively, for the final basis weight of $40\ g/m^2$ and the mass diameter of $6\ \mu m$. As you seen in these two figures, the packed structure of cube is denser in comparison with dandelion one (dandelion packed structure is more porous). During the introducing the particles to the simulation media with initial deposition velocity and external body force are constant. The variation of the number of masses for different shapes of particles is presented in result and discussion section, where the number of masses varied from two (spherocylinder) to 19 (brick with aspect ratio of 4).

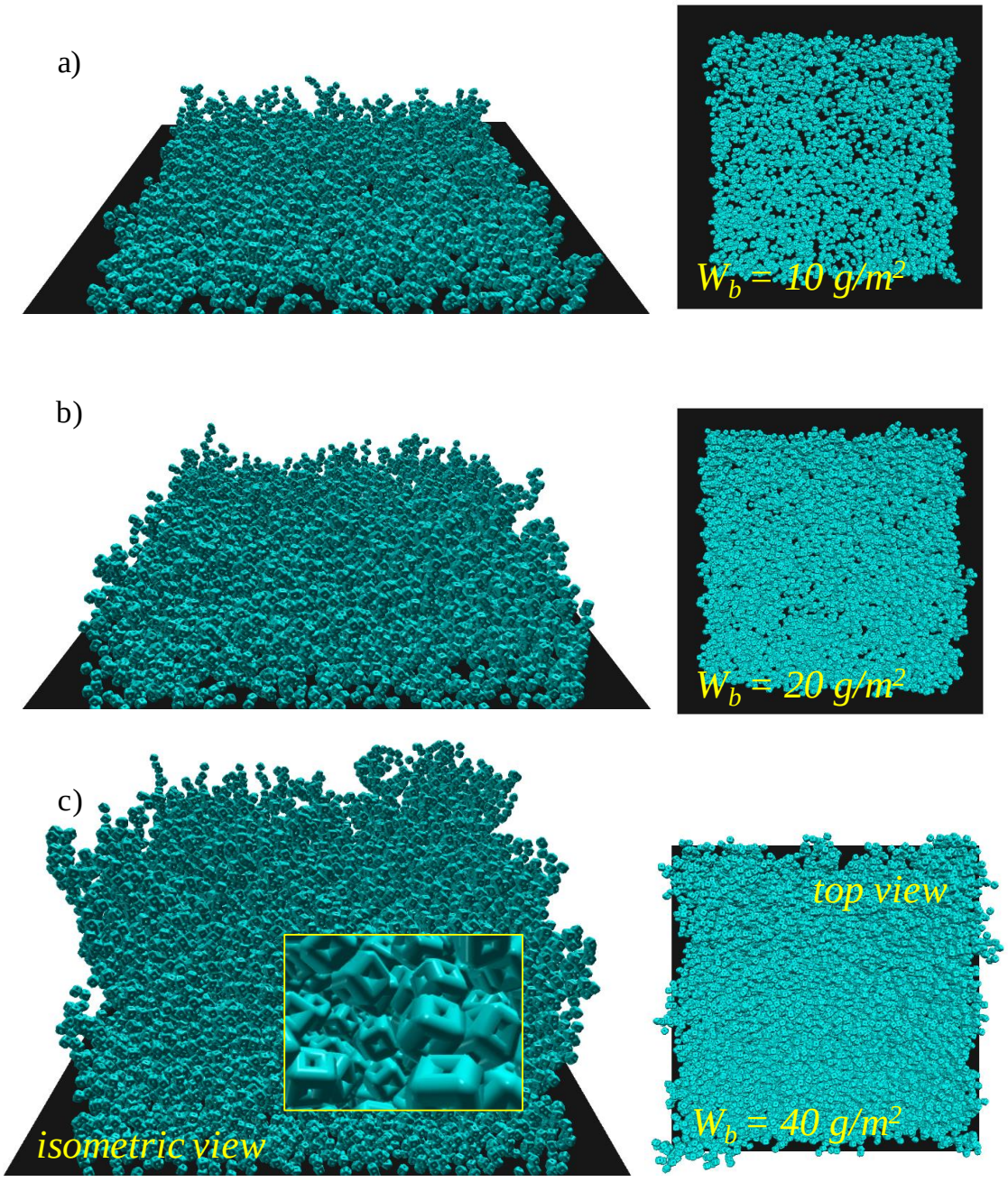


**Figure 5.4:** An example of our virtual packed cube structures is shown with cube having a diameter mass of 6 µm and a basis weight of 10 g/m$^2$ in (a). Figures (b), and (c), show 3-D structure of packed dust (left) and the top view (right) during cube deposition at different basis weights of 20, and 40 g/m$^2$, respectively. Figure (c) is shown the final structure along with a magnified image showing the cube interaction.

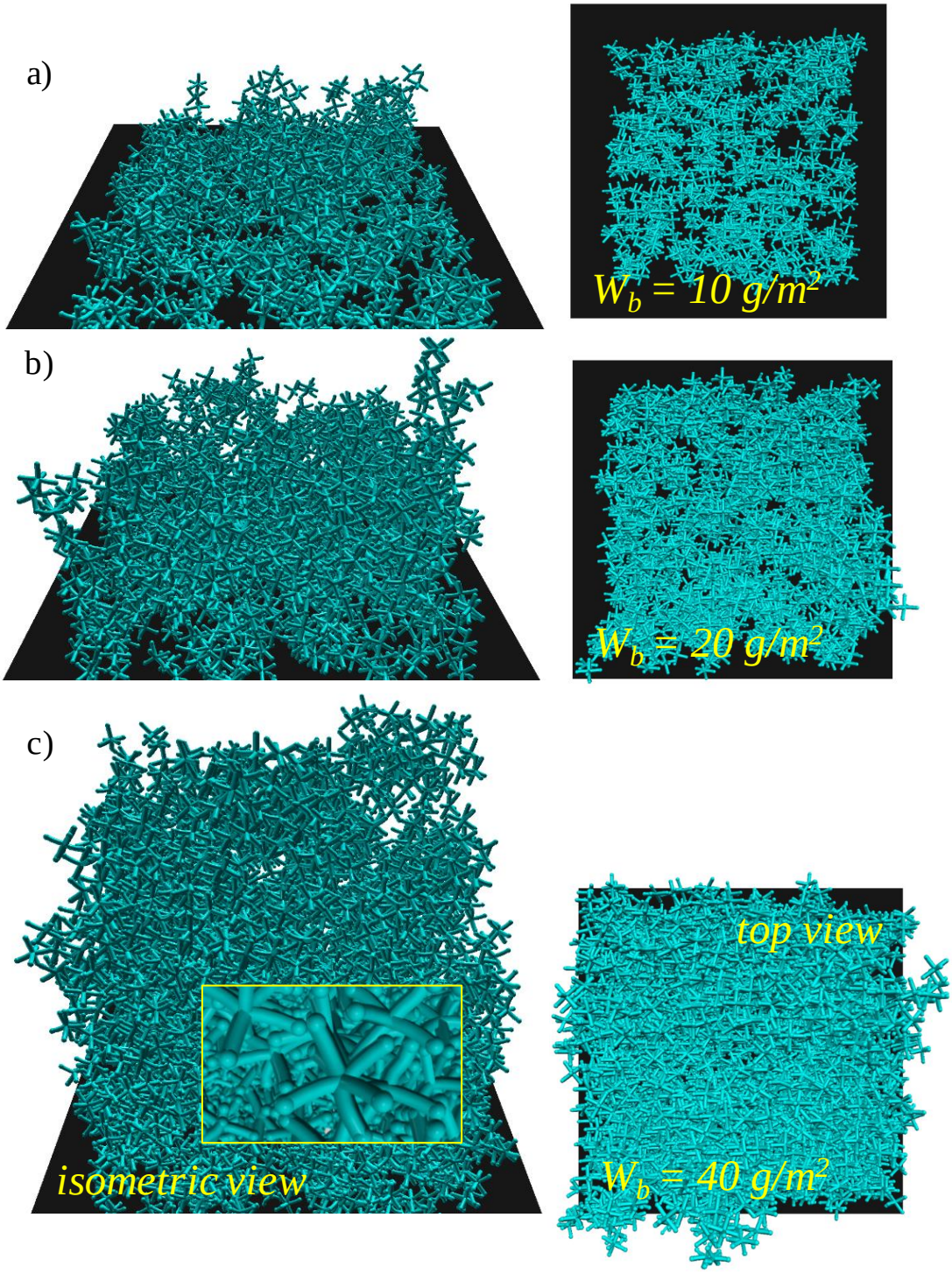


**Figure 5.5:** An example of our virtual packed dandelion structures is shown with dandelion having a diameter mass of 6 μm and a basis weight of 10 $g/m^2$ in (a). Figures (b), and (c), show 3-D structure of packed dust (left) and the top view (right) during dandelion deposition at different basis weights of 20, and 40 $g/m^2$, respectively.

All numerical parameters keep the same values for different shapes simulation. First, non-spherical objects with different size are generated and starts falling from random position on top of the substrate with adequate space till touching the next solid surface. Unreasonable intersections and penetration between particles in the particle packing are the challenging task that can directly affect the solid volume fraction of simulated structure. This issue would be handled by collision detection algorithm. The particles introduced to the media one-by-one to place on top of each other to formed dust.

### 5.3.2 Collision Detection (Particle-Particle Contact)

The contacts detection used in our simulation to prevent the penetration of non-spherical particles to other ones with detection the distance of point masses, which is used to simulate the non-spherical particles of arbitrary shape. As be discussed earlier in the previous section, we produce non-spherical particles comprised of number of masses that can move in Z-direction till touch the next solid surface (generally deposited dust or substrate). Here, for general contact detection (also called collision detection) of non-spherical particles, two sequential steps are done simultaneously: depositing the dust formation (falling down) and detecting its distance with deposited particles or solid surfaces (substrate). For the first steps as presented in previous section the point mass's positions of falling particle updated in every time steps as presented in force balance section. For the second steps of collision detection, this study adopts the position of 2 particles when they touch each other and freeze both as detailed below.

In each time steps the introduced particle moves down till the center-to-center distance of coming particle and deposited particle is equal to the point mass's diameter. Next, the coming particle

stops and prevents the collisions with the deposited particles. After freezing the coming particle, particle velocity is reset to 0 and the position of this particle considered as a deposited particle to avoid moving due to possible others penetrations and collisions. The algorithm checks whether or not a collision has occurred between the point masses of a coming particles and those of the already deposited particles (as well as among the point masses of the same objects). Particles interpenetration is avoided by monitoring the distance between the masses at each time step to ensure that no masses can come closer to one another by a distance less than a mass diameter. If two masses are interpenetrating, the distance between these beads at that time step is corrected (moved apart in the direction of the vector connecting them) to become equal to the mass diameter. Once the deposition and collision detection processes are completed, the dusts are assumed to be rigid. Therefore, the masses in the formed dust do not move every time a new object is deposited. This allows our collision detection algorithm to search for a collision between the masses of a new particles and those of the deposited particles. The number of masses affects the computing time of the algorithm because of increasing the number of contacts. Obviously, the simulations slow down as additional particles enter the simulation domain. To summarize, in our dust growth simulations, we allow the non-spherical particles to fall down horizontally until they reach next surface, and we then stop them from moving.

### 5.4 Results and Discussion

The 3-D structure of dust packing including non-spherical particles are not easy to simulate for the industrial researches. These packed particles have been discussed based on defect in filtration industries and are critical to characterize the formed dust. In fact, we proposed an accurate model to simulate the packing particles that have a good visual agreement with the formed dust in pleated

filters. The non-spherical particles used in our simulation covered a wider range of shapes in comparison with those of presented in literature [177,185]. In contrast with other works in literature, we developed a new approach to model formation and growth of dust-cakes comprised of non-overlapping non-spherical particles, for the first time. We start section by first presenting a visual comparison between packing different shapes of particle obtained from simulation. We then move on to compare simulation results for different parameters. We study the effect of mechanical properties of particles (shape and size) on thickness or porosity (SVF) of the packed particle.

In this work, we simulate the random packing of different particles with the aspect ratio varied from 2 to 4. The basis weight of deposited particle is equal to number of deposited particle multiple by volume of each particle (See Equation 5.1) and density of dust divided by the covered area on in-plan computational domain size. 3-D structure of non-spherical particle packs are presented in Figures 5.6-5.8. It can be seen that 3-D structure for a larger aspect ratio makes structure more porous for same shape with same size. Based on the results given in Figures 5.6-5.8, the changes in 3-D structures is significantly for spherocylinder particles in compare with brick one. We believe the 3-D structure of different shapes for the aspect ratio of 2 in Figures 5.6-5.8 is more uniform and dense than larger aspect ratio. Furthermore, comparing the 3-D structure given in Figures 5.6-5.8, one can see that the solid volume fraction is lower for the higher aspect ratio of dandelion and the spherocylinder with aspect ratio of 2 has the highest solid volume fraction. Figures in the below show the magnified image of isometric view to present the particles interaction. Here, we considered point masses with a diameter of $d_p = 9\,\mu m$, total basis weight of $W_b = 40\ g/m^2$ and aspect ratio varied from 2 to 4.

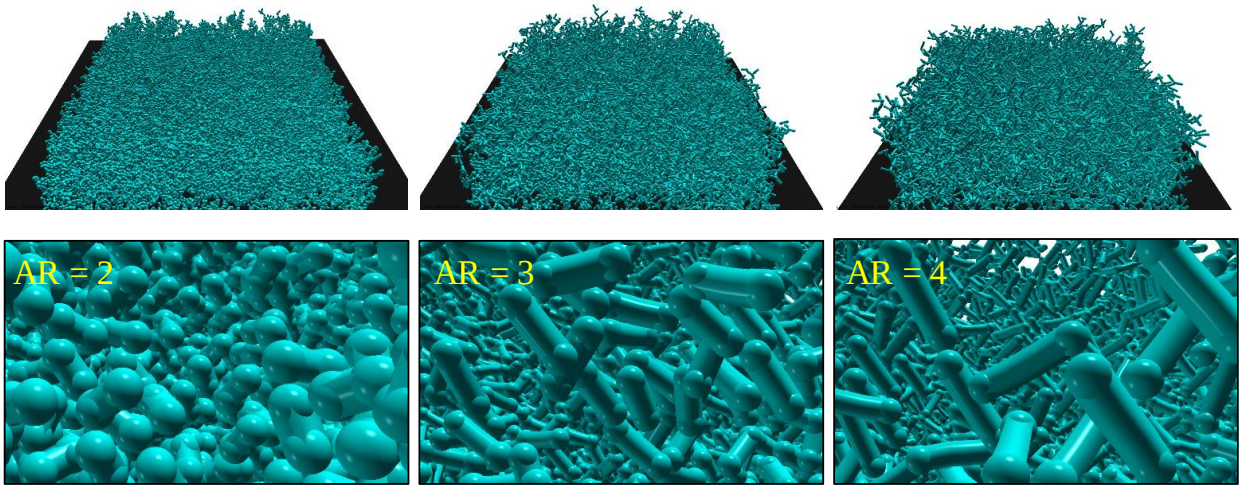


**Figure 5.6:** An example of our virtual packed spherocylinder structures is given for 3 different aspect ratio (2, 3, and 4). Figures are shown the structure with spherocylinder having a diameter mass of 9 μm and a basis weight of 40 $g/m^2$ along with a magnified image showing the spherocylinder interaction on below.

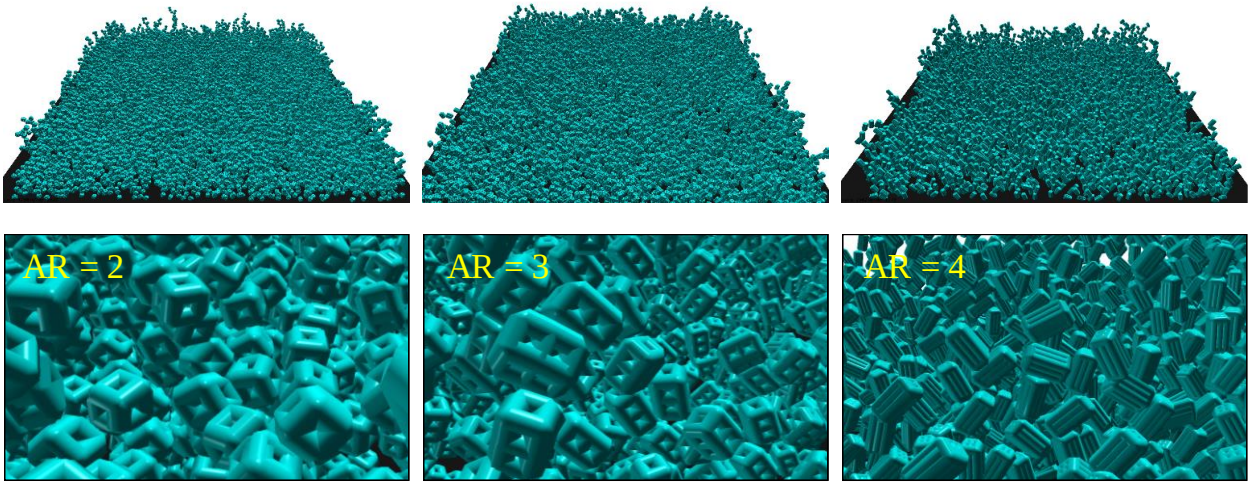


**Figure 5.7:** An example of our virtual packed brick structures is given for 3 different aspect ratio (2, 3, and 4). Figures are shown the structure with brick having a diameter mass of 9 μm and a basis weight of 40 $g/m^2$ along with a magnified image showing the brick interaction on below.

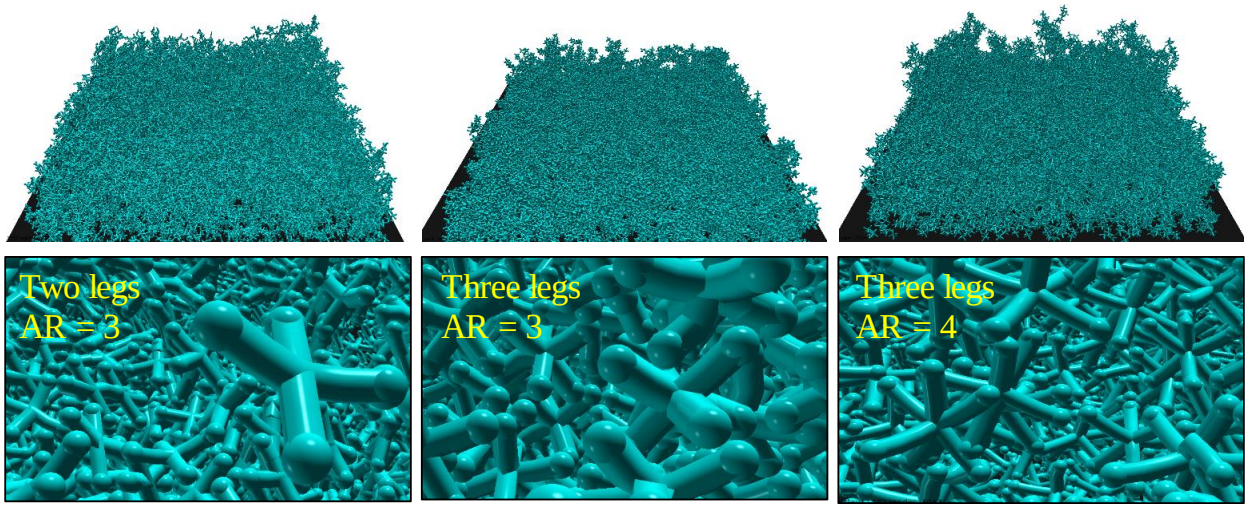


**Figure 5.8:** An example of our virtual packed dandelion structures is given for 2 different aspect ratio (3, and 4) and 2 different number of legs (2, and 3). Figures are shown the structure with dandelion having a diameter mass of 9 μm and a basis weight of 40 $g/m^2$ along with a magnified image showing the dandelion interaction on below.

Figures 5.9-5.11 are showing the dimensionless thickness and solid volume fraction, respectively, for constant total basis weight $40\ g/m^2$ at different mass diameter for different shapes. Figures 5.9, 5.10, and 5.11 show the results for the dust packing with an external body force of 0.040 N/kg for the brick, spherocylinder, and dandelion, respectively. Increasing the mass diameter reveals the reduction in SVF (Figures 5.9a-5.11a). The structure for small number of aspect ratio are denser and have the higher SVF. Furthermore, comparing the results given in Figures 5.9b-5.11b, one can see that the dimensionless thickness is higher for smaller diameter. Figures 5.9b-5.11b also show that thickness increases with increasing aspect ratio of particles. Interestingly, he SVF value for dandelion with 2 legs and aspect ratio of 4 is close to dandelion with 3 legs and aspect ratio of 3. It seems adding more legs have the same effect on mechanical properties like increasing the aspect ratio.

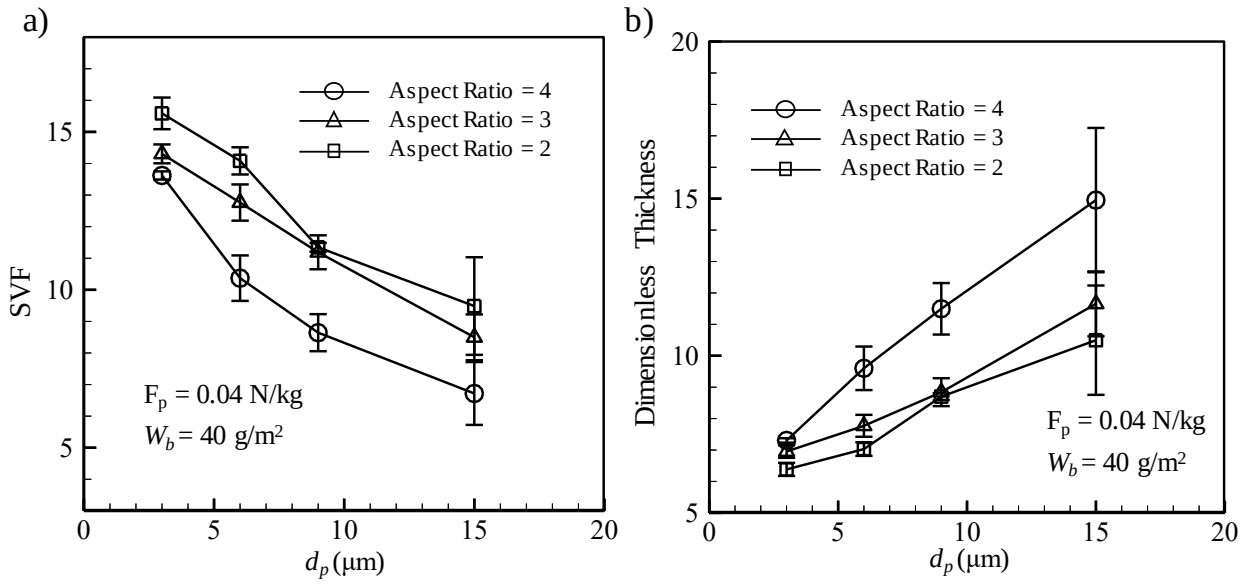


**Figure 5.9:** A comparison between SVF and dimensionless thickness of dust packed for brick with total basis weigh of 40 g/m$^2$ and external body force of 0.04 N/kg, are shown in (a) and (b), respectively.

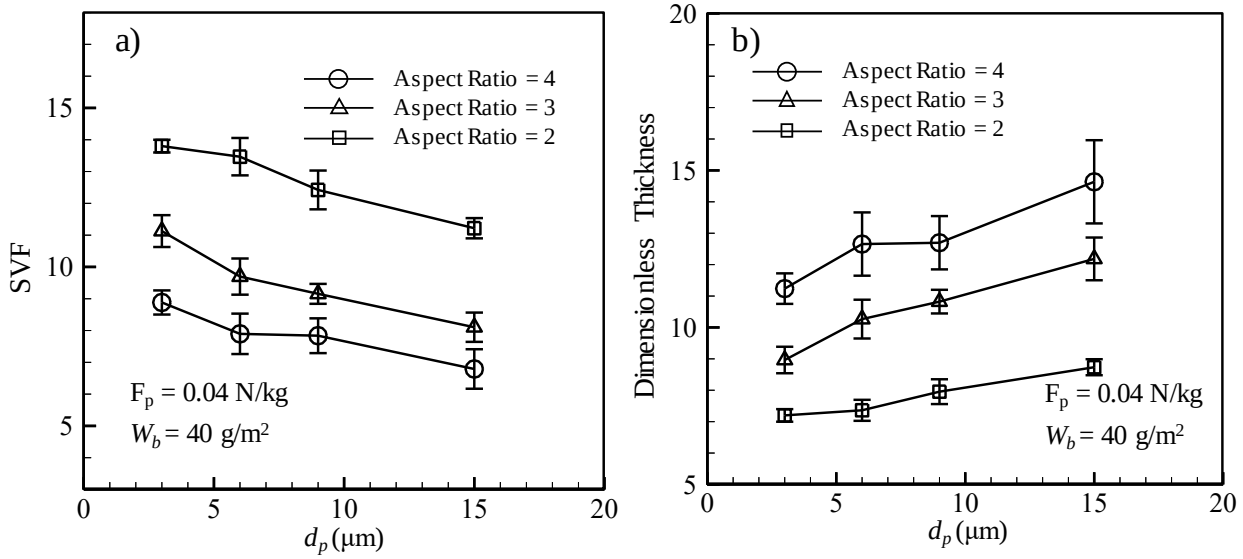


**Figure 5.10:** A comparison between SVF and dimensionless thickness of dust packed for spherocylinder with total basis weigh of 40 g/m$^2$ and external body force of 0.04 N/kg, are shown in (a) and (b), respectively.

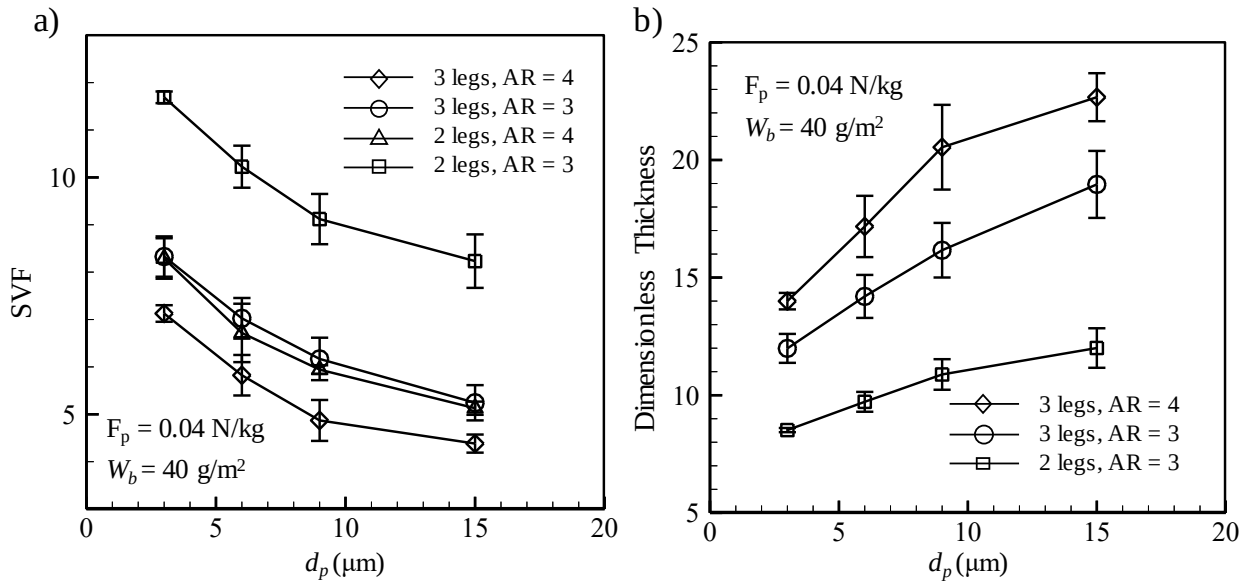


**Figure 5.11:** A comparison between SVF and dimensionless thickness of dust packed for dandelion with total basis weigh of 40 g/m$^2$ and external body force of 0.04 N/kg, are shown in (a) and (b), respectively.

Figure 5.12 shows a computational investigation on the effects of different non-spherical particles (keeping the same external body force and aspect ratio) on SVF and dimensionless thickness of 3-D structure of dust. The basis weight is 40 $g/m^2$. The effect of shape on the SVF is not negligible and for the dandelion particles, the SVF is the lower than others. Also, it is shown that the dimensionless thickness depends on the shapes and it reduced for the compact symmetric shapes and more for dandelion particles. As the three-dimensional structure of different shapes (dandelion, cube and Spherocylinder) are simulated and showed in Figures 5.9-5.11. It can be expected that 3-D structure for a larger aspect ratio of particle becomes less dense for same diameter size. Results show that the structure of dust formation for the particles with a symmetric shape (cube) is more uniform than dandelion particles.

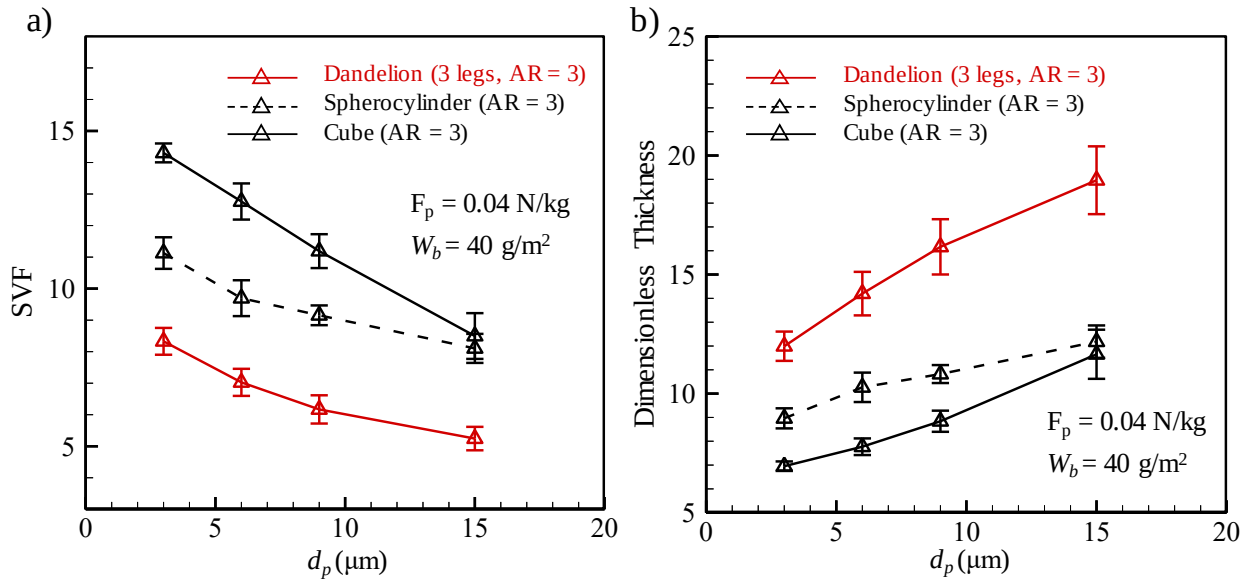


**Figure 5.12:** A comparison between SVF and dimensionless thickness of dust packed for three different shapes with the same total basis weigh of 40 g/m$^2$ and external body force of 0.04 N/kg, are shown in (a) and (b), respectively.

In our simulation, a constant external body force is applied to all the included masses in different objects. To study the effect of external forces effects on packing density, the proposed model is capable to simulate 3-D structure of packed dust for different packing force in the absence of gravity. Then the simulation repeated for other shape of particles. In a pioneering study, the particle packing was done to obtain the packing density of different simple shapes [177-187]. Our unique approach allowed the investigator to deposit the known shape with known mechanical properties of dust to form a pack of dust and to characterize the formed 3-D structure for objects in terms of objects shape, size, and aspect ratio in the presence of external forces.

## 5.5 Conclusions

The study presented here is the first to develop an in-house mass-spring-damper model to simulate the non-spherical dust formation in terms of the shape and size. In this method, each object in the media is treated as an array of mass with a same diameter, and connected to one another by a series of spring and dampers. This helps simulations to model different complex particles and deposit them on top of each other without collision that has never been reported previously. The effects of size, aspect ratio variation in dust formation are simulated in this work. It was found that porosity and thickness of formed dust with constant basis weight increases with increasing the mass diameter and aspect ratio. Our simulations also indicated that porosity is higher for the non-spherical particles with non-uniform shapes with high value of aspect ratio. This new simulation approach can be used to study the morphology of a dust-cake and how it impacts, for instance, the filtration efficiency of a dust-loaded filter, among many other applications.

## Chapter 6. Overall Conclusions

A series of investigations on characterizing the 3-D structure of porous media has been presented in this thesis. Computational simulations and experiments were developed to find the effects of polymer properties on the resulting electrospun mat and deposited fibers. Our work on electrospinning process simulation was focused on the electrospinning condition and polymer properties effects on deposited fibers. It was found that fiber diameter decreases with decreasing polymer concentration (for solution of polystyrene and polycaprolactone). Moreover, fiber diameter was found to reduce with increasing needle to collector distance but the deposition velocity increased by increasing the applied DC voltage.

The modeling filament formation in electrospinning process is combined with the structure generation algorithm to develop in-house C++ computer program for electrospun mat simulation. We focused on calibrating the model in two ways: 1) producing a large set of experimental data for polystyrene (PS) mats to be used in developing a representative mat-thickness vs. fiber-diameter curve fit, and 2) using single-fiber force-deflection experimental data reported in the literature for polycaprolactone (PCL) fibers. The model accepts inputs like diameter, basis weight, deposition velocity, and bending properties for the fibers as well as diameter and basis weight for the spacer particles. The model then predicts morphological parameters like filter porosity and filter thickness, as a function of polymer properties and electrospinning conditions.

Following the established knowledge for the effect of electrospinning condition on the diameter of fiber, we computed the effects of electrospinning process on the electrospun thickness (corresponding to empirical correlation) reasonable for the electrospun mats comprised of polystyrene and olycaprolactone fiber. The results show that parameters as distance from nozzle

to collector, fiber diameter, and applied voltage have the moderate influence on the resulting electrospun thickness. It was found that solid volume fraction increases with fiber diameter, however the effect becomes less when increasing the concentration of polymer. In particular, it was shown that applied voltage and needle to collector increases the tendency of electrospun mat to reduce its thickness.

The work presented here is the first to report the effects of spacer particles with different diameters or basis weights on the thickness and solid volume fraction of spacer-embedded fibrous media. Such morphological information is then used for collection efficiency and pressure drop predictions when challenged with aerosol particles in the particle diameter range of 20 nm to 5 μm at a face velocity of 10 cm/s. Our results indicate that adding spacer particles to a fibrous filter can lower its collection efficiency and pressure drop, but the reduction in the pressure drop will be at a higher rate resulting in better filters, i.e., filters with better quality factors.

This study presents a new approach for mass-spring-damper method (MSD) modeling of non-spherical particles to form the dust packed. A uniform approach to obtain a position and number of mass is employed to represent a realistic 3-D structure of packed non-spherical particle, which is shown to be versatile and effective in reproducing a wide range of shape features including aspect ratio for real particles in nature. The simulation results prove this point that the symmetric particles (like cube and short fibers) with the small aspect ratio and small size have the highest solid volume fraction (packing density) in comparison with other non-spherical particle.

In addition to serving as a characterization tool for porous structure, the computational model developed in this work can be used to create accurate representations of the surface morphology or the internal geometry of fibrous materials and packed dust used in variety of applications such as particle filtration or droplet separation.

## Chapter 7. References


[1] Z. Ma, M. Kotaki, R. Inai, S. Ramakrishna, Potential of nanofiber matrix as tissue-engineering scaffolds. *Tissue engineering*, *11*(1-2) (2005) 101-109.

[2] S. Agarwal, J. H. Wendorff, A. Greiner, Use of electrospinning technique for biomedical applications. *Polymer*, *49*(26) (2008) 5603-5621.

[3] R. S. Barhate, S. Ramakrishna, Nanofibrous filtering media: filtration problems and solutions from tiny materials. *Journal of membrane science*, *296*(1-2) (2007) 1-8.

[4] R. Gopal, S. Kaur, Z. Ma, C. Chan, S. Ramakrishna, T. Matsuura, Electrospun nanofibrous filtration membrane. *Journal of Membrane Science*, *281*(1-2) (2006) 581-586.

[5] S. U. Patel, G. G. Chase, Separation of water droplets from water-in-diesel dispersion using superhydrophobic polypropylene fibrous membranes. *Separation and Purification Technology*, *126* (2014) 62-68.

[6] S. Zhang, H. Liu, X. Yin, J. Yu, B. Ding, Anti-deformed polyacrylonitrile/polysulfone composite membrane with binary structures for effective air filtration. *ACS applied materials & interfaces*, *8*(12) (2016) 8086-8095.

[7] A. C. Patel, S. Li, C. Wang, W. Zhang, Y. Wei, Electrospinning of porous silica nanofibers containing silver nanoparticles for catalytic applications. *Chemistry of materials*, *19*(6) (2007) 1231-1238.

[8] Y. Liao, C. H. Loh, R. Wang, A. G. Fane, Electrospun superhydrophobic membranes with unique structures for membrane distillation. *ACS applied materials & interfaces*, *6*(18) (2014) 16035-16048.

[9] H. Aziz, M. M. Amrei, A. Dotivala, C. Tang, H. V. Tafreshi, Modeling Cassie droplets on superhydrophobic coatings with orthogonal fibrous structures. *Colloids and Surfaces A: Physicochemical and Engineering Aspects*, *512* (2017) 61-70.

[10] M. Jamali, A. Moghadam, H. V. Tafreshi, B. Pourdeyhimi, Droplet adhesion to hydrophobic fibrous surfaces. *Applied Surface Science*, *456* (2018) 626-636.

[11] E. R. Kenawy, G. L. Bowlin, K. Mansfield, J. Layman, D. G. Simpson, E. H. Sanders, G. E. Wnek, Release of tetracycline hydrochloride from electrospun poly (ethylene-co-vinylacetate), poly (lactic acid), and a blend. *Journal of controlled release*, *81*(1-2) (2002) 57-64.

[12] D. Liang, B. S. Hsiao, B. Chu, Functional electrospun nanofibrous scaffolds for biomedical applications. *Advanced drug delivery reviews*, *59*(14) (2007) 1392-1412.

[13] X. Wang, B. Ding, J. Yu, M. Wang, F. Pan, A highly sensitive humidity sensor based on a nanofibrous membrane coated quartz crystal microbalance. *Nanotechnology*, *21*(5) (2009) 055502.

[14] B. Ding, M. Wang, J. Yu, G. Sun, Gas sensors based on electrospun nanofibers. *Sensors*, *9*(3) (2009) 1609-1624.

[15] S. H. Yousefi, D. G. Venkateshan, C. Tang, H. V. Tafreshi, B. Pourdeyhimi, Effects of electrospinning conditions on microstructural properties of polystyrene fibrous materials. *Journal of Applied Physics*, *124*(23) (2018) 235307.

[16] S. H. Yousefi, C. Tang, H. V. Tafreshi, B. Pourdeyhimi, Empirical model to simulate morphology of electrospun polycaprolactone mats. *Journal of Applied Polymer Science*, *136*(46) (2019) 48242.

[17] T. Subbiah, G. S. Bhat, R. W. Tock, S. Parameswaran, S. S. Ramkumar, Electrospinning of nanofibers. *Journal of applied polymer science*, *96*(2) (2005) 557-569.

[18] J. J. Qin, M. H. Oo, K. A. Kekre, F. Knops, P. Miller, Reservoir water treatment using hybrid coagulation–ultrafiltration. *Desalination*, *193*(1-3) (2006) 344-349.

[19] X. Wei, H. Zhou, F. Chen, H. Wang, Z. Ji, T. Lin, High-Efficiency Low-Resistance Oil-Mist Coalescence Filtration Using Fibrous Filters with Thickness-Direction Asymmetric Wettability. *Advanced Functional Materials*, *29*(1) (2019) 1806302.

[20] C. Wolf, M. Tscherner, S. Köstler, Ultra-fast opto-chemical sensors by using electrospun nanofibers as sensing layers. *Sensors and Actuators B: Chemical*, *209* (2015) 1064-1069.

[21] M. I. Hassan, T. Sun, N. Sultana, Fabrication of nanohydroxyapatite/poly (caprolactone) composite microfibers using electrospinning technique for tissue engineering applications. *Journal of Nanomaterials*, *2014* (2014) 65.

[22] S. C. Baker, N. Atkin, P. A. Gunning, N. Granville, K. Wilson, D. Wilson, J. Southgate, Characterisation of electrospun polystyrene scaffolds for three-dimensional in vitro biological studies. *Biomaterials*, *27*(16) (2006) 3136-3146.

[23] F. Guo, A. Servi, A. Liu, K. K. Gleason, G. C. Rutledge, Desalination by membrane distillation using electrospun polyamide fiber membranes with surface fluorination by chemical vapor deposition. *ACS applied materials & interfaces*, *7*(15) (2015) 8225-8232.

[24] L. T. S. Choong, Y. M. Lin, G. C. Rutledge, Separation of oil-in-water emulsions using electrospun fiber membranes and modeling of the fouling mechanism. *Journal of membrane science*, *486* (2015) 229-238.

[25] F. Zhu, Q. Xin, Q. Feng, Y. Zhou, R. Liu, Novel poly (vinylidene fluoride)/thermoplastic polyester elastomer composite membrane prepared by the electrospinning of nanofibers onto a dense membrane substrate for protective textiles. *Journal of Applied Polymer Science*, *132*(26) (2015).

[26] S. Michielsen, H. J. Lee, Design of a superhydrophobic surface using woven structures. *Langmuir*, *23*(11) (2007) 6004-6010.

[27] D. Chen, L. Tan, H. Liu, J. Hu, Y. Li, F. Tang, Fabricating superhydrophilic wool fabrics. *Langmuir*, *26*(7) (2009) 4675-4679.

[28] D. A. Baker, P. J. Brown, Production of cross-linked PET fibrous substrates via electrospinning (2006) 173-187.

[29] B. M. Baker, A. O. Gee, R. B. Metter, A. S. Nathan, R. A. Marklein, J. A. Burdick, R. L. Mauck,

The potential to improve cell infiltration in composite fiber-aligned electrospun scaffolds by the selective removal of sacrificial fibers. *Biomaterials*, *29*(15) (2008) 2348-2358.

[30] J. Zheng, A. He, J. Li, J. Xu, C. C. Han, Studies on the controlled morphology and wettability of polystyrene surfaces by electrospinning or electrospraying. *Polymer*, *47*(20) (2006) 7095-7102.

[31] K. H. Lee, H. Y. Kim, Y. J. Ryu, K. W. Kim, S. W. Choi, Mechanical behavior of electrospun fiber mats of poly (vinyl chloride)/polyurethane polyblends. *Journal of Polymer Science Part B: Polymer Physics*, *41*(11) (2003) 1256-1262.

[32] M. Shafiei, N. Ojaghlou, S. G. Zamfir, D. Bratko, A. Luzar, Modulation of structure and dynamics of water under alternating electric field and the role of hydrogen bonding. *Molecular Physics*, (2019) 1-15.

[33] D. H. Reneker, A. L. Yarin, H. Fong, S. Koombhongse, Bending instability of electrically charged liquid jets of polymer solutions in electrospinning. *Journal of Applied physics*, *87*(9) (2000) 4531-4547.

[34] A. L. Yarin, S. Koombhongse, D. H. Reneker, Bending instability in electrospinning of nanofibers. *Journal of applied physics*, 89(5) (2001) 3018-3026.

[35] A. L. Yarin, E. Zussman, Upward needleless electrospinning of multiple nanofibers. *Polymer*, *45*(9) (2004) 2977-2980.

[36] D. H. Reneker, A. L. Yarin, Electrospinning jets and polymer nanofibers. *Polymer*, *49*(10) (2008) 2387-2425.

[37] W. E. Teo, S. Ramakrishna, A review on electrospinning design and nanofibre assemblies. *Nanotechnology*, 17(14) (2006) R89.

[38] S. Rafiei, S. Maghsoodloo, B. Noroozi, V. Mottaghitalab, A. K. Haghi, Mathematical modeling in electrospinning process of nanofibers: a detailed review. *Cellul Chem Technol*, *47* (2013) 323-338.

[39] N. M. Farhan, H. Aziz, H. V. Tafreshi, Simple Method To Measuring Intrinsic Contact Angle of a Fiber with Liquids, *Experiments in Fluids*, 60 (2019) 87.

[40] N. Ojaghlou, H. V. Tafreshi, D. Bratko, A. Luzar, Dynamical insights into the mechanism of a droplet detachment from a fiber. *Soft matter*, 14(44) (2018) 8924-8934.

[41] S. A. Theron, E. Zussman, A. L. Yarin, Experimental investigation of the governing parameters in the electrospinning of polymer solutions. *Polymer*, 45 (2004) 2017–2030.

[42] S. A. Theron, A. L. Yarin, E. Zussman, E. Kroll, Multiple jets in electrospinning: experiment and modeling. *Polymer*, 46(9) (2005) 2889-2899.

[43] M. Lauricella, G. Pontrelli, I. Coluzza, D. Pisignano, S. Succi, JETSPIN: A specific-purpose open-source software for simulations of nanofiber electrospinning. *Computer Physics Communications*, *197* (2015) 227-238.

[44] M. Lauricella, D. Pisignano, S. Succi, Effects of nanoparticles on the dynamic morphology of electrified jets. *EPL (Europhysics Letters)*, *119*(4) (2017) 44001.

[45] M. Lauricella, D. Pisignano, S. Succi, Three-dimensional model for electrospinning processes in controlled gas counterflow. *The Journal of Physical Chemistry A*, *120*(27) (2016) 4884-4892.

[46] M. Lauricella, F. Cipolletta, G. Pontrelli, D. Pisignano, S. Succi, Effects of orthogonal rotating electric fields on electrospinning process. *Physics of Fluids*, *29*(8) (2017) 082003.

[47] P. Valipour, S. E. Ghasemi, Effect of non-Newtonian rheology on electrified jets of polymer nanofibers in electrospinning process based on bead–spring model. *The International Journal of Advanced Manufacturing Technology*, *91*(9-12) (2017) 3535-3550.

[48] C. J. Thompson, G. G. Chase, A. L. Yarin, D. H. Reneker, Effects of parameters on nanofiber diameter determined from electrospinning model. *Polymer*, *48*(23) (2007) 6913-6922.

[49] D. Borzacchiello, S. Vermiglio, F. Chinesta, S. Nabat, K. Lafdi, Numerical simulation of electrified jets: An application to electrospinning. In *AIP Conference Proceedings* (Vol. 1769, No. 1, p. 050004) (2016, October) AIP Publishing.

[50] M. Šimko, D. Lukáš, Mathematical modeling of a whipping instability of an electrically charged liquid jet. *Applied Mathematical Modelling*, *40*(21-22) (2016) 9565-9583.

[51] S. Gadkari, Influence of polymer relaxation time on the electrospinning process: Numerical investigation. *Polymers*, *9*(10) (2017) 501.

[52] G. Pontrelli, D. Gentili, I. Coluzza, D. Pisignano, S. Succi, Effects of non-linear rheology on electrospinning process: A model study. *Mechanics Research Communications*, *61* (2014) 41-46.

[53] M. Lauricella, G. Pontrelli, I. Coluzza, D. Pisignano, S. Succi, Different regimes of the uniaxial elongation of electrically charged viscoelastic jets due to dissipative air drag. *Mechanics Research Communications*, *69* (2015) 97-102.

[54] G. T. Kim, Y. J. Hwang, Y. C. Ahn, H. S. Shin, J. K. Lee, C. M. Sung, The morphology of electrospun polystyrene fibers. *Korean Journal of Chemical Engineering*, *22*(1) (2005) 147-153.

[55] S. H. Yousefi, H. V. Tafreshi, Modeling electrospun fibrous structures with embedded spacer particles: Application to aerosol filtration. *Separation and Purification Technology*, *235* (2020) 116184.

[56] L. M. Hansen, D. J. Smith, D. H. Reneker, W. Kataphinan, Water absorption and mechanical properties of electrospun structured hydrogels. *Journal of Applied Polymer Science*, *95*(2) (2005) 427-434.

[57] C. Shin, G. G. Chase, D. H. Reneker, The effect of nanofibers on liquid–liquid coalescence filter performance. *AIChE journal*, *51*(12) (2005) 3109-3113.

[58] J. Lannutti, D. Reneker, T. Ma, D. Tomasko, D. Farson, Electrospinning for tissue engineering scaffolds. *Materials Science and Engineering: C*, 27(3) (2007) 504-509.

[59] V. Thavasi, G. Singh, S. Ramakrishna, Electrospun nanofibers in energy and environmental applications. *Energy & Environmental Science*, 1(2) (2008) 205-221.

[60] D. Lolla, M. Lolla, A. Abutaleb, H. Shin, D. Reneker, G. Chase, Fabrication, polarization of electrospun polyvinylidene fluoride electret fibers and effect on capturing nanoscale solid aerosols. *Materials*, 9(8) (2016) 671.

[61] J. Xu, C. Liu, P. C. Hsu, K. Liu, R. Zhang, Y. Liu, Y. Cui, Roll-to-roll transfer of electrospun nanofiber film for high-efficiency transparent air filter. *Nano letters*, 16(2) (2016) 1270-1275.

[62] Y. M. Lin, G. C. Rutledge, Separation of oil-in-water emulsions stabilized by different types of surfactants using electrospun fiber membranes. *Journal of membrane science*, 563 (2018) 247-258.

[63] M. M. Munir, A. B. Suryamas, F. Iskandar, K. Okuyama, Scaling law on particle-to-fiber formation during electrospinning. *Polymer*, 50(20) (2009) 4935-4943.

[64] B. K. Brettmann, S. Tsang, K. M. Forward, G. C. Rutledge, A. S. Myerson, B. L. Trout, Free surface electrospinning of fibers containing microparticles. *Langmuir*, 28(25) (2012) 9714-9721.

[65] C. Shin, G. G. Chase, D. H. Reneker, Recycled expanded polystyrene nanofibers applied in filter media. *Colloids and Surfaces A: Physicochemical and Engineering Aspects*, 262(1-3) (2005) 211-215.

[66] M. S. Oliveira, G. H. McKinley, Iterated stretching and multiple beads-on-a-string phenomena in dilute solutions of highly extensible flexible polymers. *Physics of fluids*, *17*(7) (2005) 071704.

[67] P. P. Bhat, S. Appathurai, M. T. Harris, M. Pasquali, G. H. McKinley, O. A. Basaran, Formation of beads-on-a-string structures during break-up of viscoelastic filaments. *Nature Physics*, *6*(8) (2010) 625.

[68] C. Huang, S. Chen, C. Lai, D. H. Reneker, H. Qiu, Y. Ye, H. Hou, Electrospun polymer nanofibres with small diameters. *Nanotechnology*, 17(6) (2006) 1558.

[69] M. Wang, J. H. Yu, A. J. Hsieh, G. C. Rutledge, Effect of tethering chemistry of cationic surfactants on clay exfoliation, electrospinning and diameter of PMMA/clay nanocomposite fibers. *Polymer*, 51(26) (2010) 6295-6302.

[70] D. Zhang, A. B. Karki, D. Rutman, D. P. Young, A. Wang, D. Cocke, T. H. Ho, Z. Guo, Electrospun polyacrylonitrile nanocomposite fibers reinforced with Fe3O4 nanoparticles: Fabrication and property analysis. *Polymer*, *50*(17) (2009) 4189-4198.

[71] A. Ghosal, S. Sinha-Ray, A. L. Yarin, B. Pourdeyhimi, Numerical prediction of the effect of uptake velocity on three-dimensional structure, porosity and permeability of meltblown nonwoven laydown.

*Polymer*, 85 (2016) 19-27.

[72] H. Fong, I. Chun, D. H. Reneker, Beaded nanofibers formed during electrospinning. *Polymer*, *40*(16) (1999) 4585-4592.

[73] K. H. Lee, H. Y. Kim, H. J. Bang, Y. H. Jung, S. G. Lee, The change of bead morphology formed on electrospun polystyrene fibers. *Polymer*, 44(14) (2003) 4029-4034.

[74] C. M. Hsu, S. Shivkumar, Nano-sized beads and porous fiber constructs of poly (ε-caprolactone) produced by electrospinning. *Journal of Materials Science*, 39(9) (2004) 3003-3013.

[75] G. A. Valaskovic, J. P. Murphy, M. S. Lee, Automated orthogonal control system for electrospray ionization. *Journal of the American Society for Mass Spectrometry*, 15(8) (2004) 1201-1215.

[76] A. T. S. A. Jaworek, A. T. Sobczyk, Electrospraying route to nanotechnology: An overview. *Journal of Electrostatics*, 66(3-4) (2008) 197-219.

[77] T. Czech, S. Ramakrishna, S. Sundarrajan, Electrospinning and electrospraying techniques for nanocomposite non-woven fabric production. *Fibres Text. East. Eur*, 17 (2009) 77-81.

[78] S. Sinha-Ray, S. Sinha-Ray, A. L. Yarin, B. Pourdeyhimi, Application of solution-blown 20–50 nm nanofibers in filtration of nanoparticles: The efficient van der Waals collectors. *Journal of Membrane Science*, 485 (2015) 132-150.

[79] H. Gao, Y. Yang, O. Akampumuza, J. Hou, H. Zhang, X. Qin, A low filtration resistance three-dimensional composite membrane fabricated via free surface electrospinning for effective PM 2.5 capture. *Environmental Science: Nano*, 4(4) (2017) 864-875.

[80] M. D. Kok, J. T. Gostick, Transport properties of electrospun fibrous membranes with controlled anisotropy. *Journal of Membrane Science*, *473* (2015) 237-244.

[81] N. Mao, S. J. Russell, Modeling permeability in homogeneous three-dimensional nonwoven fabrics. *Textile Research Journal*, *73*(11) (2003) 939-944.

[82] J. Payen, P. Vroman, M. Lewandowski, A. Perwuelz, S. Calle-Chazelet, D. Thomas, Influence of fiber diameter, fiber combinations and solid volume fraction on air filtration properties in nonwovens. *Textile Research Journal*, *82*(19) (2012) 1948-1959.

[83] C. Stark, J. Fricke, Improved heat-transfer models for fibrous insulations. *International Journal of Heat and Mass Transfer*, *36*(3) (1993) 617-625.

[84] S. A. Hosseini, H. V. Tafreshi, Modeling permeability of 3-D nanofiber media in slip flow regime. *Chemical Engineering Science*, *65*(6) (2010) 2249-2254.

[85] B. Maze, H. V. Tafreshi, Q. Wang, B. Pourdeyhimi, A simulation of unsteady-state filtration via

nanofiber media at reduced operating pressures. *Journal of Aerosol Science*, *38*(5) (2007) 550-571.

[86] K. G. Kornev, Electrospinning: Distribution of charges in liquid jets. *Journal of Applied Physics*, *110*(12) (2011) 124910.

[87] M. A. Samaha, H. V. Tafreshi, M. Gad-el-Hak, Novel method to characterize superhydrophobic coatings. *Journal of Colloid and Interface Science, 395* (2013) 315-321.

[88] M. Zündel, E. Mazza, A. E. Ehret, A 2.5 D approach to the mechanics of electrospun fibre mats. *Soft Matter*, *13*(37) (2017) 6407-6421.

[89] Y. Feng, R. Sun, M. Chen, C. Liu, Q. Wang, Simulation of the morphological structures of electrospun membranes. *Journal of Applied Polymer Science*, *135*(1) (2018) 45653.

[90] P. Danwanichakul, D. Danwanichakul, Two-dimensional simulation of electrospun nanofibrous structures: connection of experimental and simulated results. *Journal of Chemistry*, *2014*.

[91] H. Kim, D. Kim, M, Seo, K. Cho, J. Haw, A simulation method for modeling the morphology and characteristics of electrospun polymeric nanowebs, *Macromolecular Research* 13, (2015) 107-113.

[92] M. Ziabari, V. Mottaghitalab, A. Haghi, Evaluation of electrospun nanofiber pore structure parameters, *Korean Journal of Chemical Engineering 25*, (2008) 923-932.

[93] M. Ziabari, V. Mottaghitalab, A. Haghi, Application of direct tracking method for measuring electrospunnanofiber diameter, *Brazilian Journal of Chemical Engineering 25*, (2009) 1678.

[94] L. Choong, P. Yi, G. Rutledge, Three-dimensional imaging of electrospun fiber mats using confocal laser scanning microscopy and digital image analysis, *Journal of Materials Science 50*, (2015) 3014-3030.

[95] D. G. Venkateshan, M. A. Tahir, H. V. Tafreshi, B. Pourdeyhimi, Modeling effects of fiber rigidity on thickness and porosity of virtual electrospun mats, *Materials and Design 96*, (2016) 27-35.

[96] A. Moghadam, S. H. Yousefi, H. V. Tafreshi, B. Pourdeyhimi,. Characterizing nonwoven materials via realistic microstructural modeling. *Separation and Purification Technology*, *211* (2019) 602-609.

[97] B. Maze, H. V. Tafreshi, B. Pourdeyhimi, Geometrical modeling of fibrous materials under compression, *Journal of Applied Physics* (2007) 073533.

[98] Q. Wang, B. Maze, H. V. Tafreshi, B. Pourdeyhimi, Simulating through-plane permeability of fibrous materials with different fiber lengths, *Modelling and Simulation in Materials Science and Engineering*, 15(8) (2007) 855–868.

[99] H. V. Tafreshi, M. S. A. Rahman, S. Jaganathan, Q. Wang, B. Pourdeyhimi, Analytical expressions for predicting permeability of bimodal fibrous porous media, *Chemical Engineering Science*, *64*(6)

(2009) 1154-1159.

[100] S. Fotovati, H. V. Tafreshi, B. Pourdeyhimi, Influence of fiber orientation distribution on performance of aerosol filtration media, *Chemical Engineering Science*, 65 (2010) 5285–5293.

[101] T. M. Bucher, B. Emami, H. V. Tafreshi, M. Gad-el-Hak, G. C. Tepper, Resistance of nanofibrous superhydrophobic coatings to hydrostatic pressure: the role of microstructure, *Physics of Fluids*, 24 (2012) 022109.

[102] B. Emami, H. V. Tafreshi, M. Gad-el-Hak, G. C. Tepper, Effect of fiber orientation on shape and stability of air–water interface on submerged superhydrophobic electrospun thin coatings, *Journal of Applied Physics* 111 (2012) 064325.

[103] R. Arambakam, H. V. Tafreshi, B. Pourdeyhimi, A simple simulation method for designing fibrous insulation materials, *Materials & Design* (2013) 44, 99.

[104] A. M. Saleh, S. A. Hosseini, H. V. Tafreshi, B. Pourdeyhimi, 3-D Microscale simulation of dust-loading in thin flat-sheet filters: a comparison with 1-d macroscale simulations, *Chemical Engineering Science*, (2013) 99, 284.

[105] H. Aziz, N. Farhan, H. V. Tafreshi, Effects of fiber wettability and size on droplet detachment residue, *Experiment in Fluids 59* (7) (2018) 122.

[106] N. M. Farhan, H. Vahedi Tafreshi, Universal expression for droplet–fiber detachment force. *Journal of Applied Physics*, 124(7) (2018) 075301.

[107] H. Aziz, H. V. Tafreshi, Competing Forces on a Liquid Bridge between Parallel and Orthogonal Dissimilar Fibers, *Soft Matter* 15, (2019) 6967.

[108] N. M. Farhan, H. V. Tafreshi, Using Magnetic Field to Measure Detachment Force between a Nonmagnetic Droplet and Fibers. *Langmuir* (2019).

[109] Z. Nie, X. Wang, Z. Liang, J. Gong, Quantitative analysis of the three-dimensional roundness of granular particles. *Powder Technology* 336 (2018) 584-593.

[110] Q. Sun, J. Zheng, H. He, Z. Li, Particulate material fabric characterization from volumetric images by computational geometry. *Powder Technology 344* (2019) 804-813.

[111] A. Jaworek, Electrospray droplet sources for thin film deposition. *Journal of Materials Science*, 42(1) (2007) 266-297.

[112] I. Sas, R. E. Gorga, J. A. Joines, K. A. Thoney, Literature review on superhydrophobic self-cleaning surfaces produced by electrospinning. *Journal of Polymer Science Part B: Polymer Physics*, *50*(12) (2012) 824-845.

[113] R. Asmatulu, M. Ceylan, N. Nuraje, Study of superhydrophobic electrospun nanocomposite fibers for energy systems. *Langmuir*, *27*(2) (2010) 504-507.

[114] M. A. Samaha, H. V. Tafreshi, M. Gad-el-Hak, Superhydrophobic surfaces: From the lotus leaf to the submarine. *Comptes Rendus Mecanique*, *340*(1-2) (2012) 18-34.

[115] D. Li, Y. Xia, Electrospinning of nanofibers: reinventing the wheel?. *Advanced Materials*, *16*(14) (2004) 1151-1170.

[116] N. Ismail, F. J. Maksoud, N. Ghaddar, K. Ghali, A. Tehrani-Bagha, A mathematical model to predict the effect of electrospinning processing parameters on the morphological characteristic of nano-fibrous web and associated filtration efficiency. *Journal of Aerosol Science*, *113* (2017) 227-241.

[117] H. Altendorf, D. Jeulin, Random-walk-based stochastic modeling of three-dimensional fiber systems. *Physical Review E*, 83(4) (2011) 041804.

[118] Q. Liu, Z. Lu, Z. Hu, J. Li, Finite element analysis on tensile behaviour of 3D random fibrous materials: Model description and meso-level approach. *Materials Science and Engineering: A*, *587* (2013) 36-45.

[119] K. Rezk, J. Forsberg, L. Nilsson, J. Berghel, Characterizing flow resistance in 3-dimensional disordered fibrous structures based on forchheimer coefficients for a wide range of reynolds numbers. *Applied Mathematical Modelling*, *40*(21-22) (2016) 8898-8911.

[120] S. Abishek, A. J. C. King, R. Mead-Hunter, V. Golkarfard, W. Heikamp, B. J. Mullins, Generation and validation of virtual nonwoven, foam and knitted filter (separator/coalescer) geometries for CFD simulations. *Separation and Purification Technology*, *188* (2017) 493-507.

[121] A. Karakoç, E. Hiltunen, J. Paltakari, Geometrical and spatial effects on fiber network connectivity. *Composite Structures*, *168* (2017) 335-344.

[122] K. Nakamura, T. Suda, K. Matsumoto, Characterization of pore size distribution of non-woven fibrous filter by inscribed sphere within 3D filter model. *Separation and Purification Technology*, *197* (2018) 289-294.

[123] G. H. West, Relaxation times of polystyrene. *Polymer*, *10* (1969) 751-758.

[124] M. M. Demir, I. Yilgor, E. E. A. Yilgor, B. Erman, Electrospinning of polyurethane fibers. *Polymer*, *43*(11) (2002) 3303-3309.

[125] T. J. Sill, H. A. von Recum, Electrospinning: applications in drug delivery and tissue engineering. *Biomaterials*, *29*(13) (2008) 1989-2006.

[126] M. Vong, E. Speirs, C. Klomkliang, I. Akinwumi, W. Nuansing, N. Radacsi, Controlled three-dimensional polystyrene micro-and nano-structures fabricated by three-dimensional

electrospinning. *RSC advances*, *8*(28) (2018) 15501-15512.

[127] R. Mead-Hunter, A. J. King, G. Kasper, B. J. Mullins, Computational fluid dynamics (CFD) simulation of liquid aerosol coalescing filters. *Journal of Aerosol Science*, *61* (2013) 36-49.

[128] A. Moghadam, M. Jamali, D. G. Venkateshan, H. V. Tafreshi, B. Pourdeyhimi, A new approach to modeling liquid intrusion in hydrophobic fibrous membranes with heterogeneous wettabilities. *Colloids and Surfaces A: Physicochemical and Engineering Aspects*, *558* (2018) 154-163.

[129] H. Aziz, H. V. Tafreshi, Role of particles spatial distribution in drag reduction performance of superhydrophobic granular coatings. *International Journal of Multiphase Flow*, *98* (2018) 128-138.

[130] M. Jamali, H. V. Tafreshi, B. Pourdeyhimi, Droplet mobility on hydrophobic fibrous coatings comprising orthogonal fibers. *Langmuir*, *34*(41) (2018) 12488-12499.

[131] M. Jamali, H. Vahedi Tafreshi, B. Pourdeyhimi, Easy-to-use correlations to estimate droplet mobility on hydrophobic fibrous coatings, *Colloids and Surfaces A: Physicochemical and Engineering Aspects* 582 (2019), 123867.

[132] L. Hao, P. Cheng, Lattice Boltzmann simulations of water transport in gas diffusion layer of a polymer electrolyte membrane fuel cell. *Journal of Power Sources*, *195*(12) (2010) 3870-3881.

[133] F. Arbabi, H. Montazeri, R. Abouatallah, R. Wang, A. Bazylak, Three-dimensional computational fluid dynamics modelling of oxygen bubble transport in polymer electrolyte membrane electrolyzer porous transport layers. *Journal of The Electrochemical Society*, *163*(11) (2016) 3062-3069.

[134] K. H. Lee, H. Y. Kim, H. J. Bang, Y. H. Jung, S. G. Lee, The change of bead morphology formed on electrospun polystyrene fibers. *Polymer*, *44*(14) (2003) 4029-4034.

[135] S. Zhao, X. Wu, L. Wang, Y. Huang, Electrospinning of ethyl–cyanoethyl cellulose/tetrahydrofuran solutions. *Journal of Applied Polymer Science*, *91*(1) (2004) 242-246.

[136] C. Zhang, X. Yuan, L. Wu, Y. Han, J. Sheng, Study on morphology of electrospun poly (vinyl alcohol) mats. *European Polymer Journal*, *41*(3) (2005) 423-432.

[137] G. Eda, S. Shivkumar, Bead-to-fiber transition in electrospun polystyrene. *Journal of Applied Polymer Science*, *106*(1) (2007) 475-487.

[138] X. Yuan, Y. Zhang, C. Dong, J. Sheng, Morphology of ultrafine polysulfone fibers prepared by electrospinning. *Polymer International*, *53*(11) (2004) 1704-1710.

[139] H. W. Tong, M. Wang, Electrospinning of fibrous polymer scaffolds using positive voltage or negative voltage: a comparative study. *Biomedical Materials*, *5*(5) (2010) 054110.

[140] A. L. Yarin, B. Pourdeyhimi, S. Ramakrishna, Fundamentals and applications of micro-and nanofibers. Cambridge University Press (2014).

[141] M. Ma, R. M. Hill, G. C. Rutledge, A review of recent results on superhydrophobic materials based on micro-and nanofibers. *Journal of Adhesion Science and Technology*, 22(15) (2008) 1799-1817.

[142] J. P. Vassal, L. Orgéas, D. Favier, Modelling microstructure effects on the conduction in fibrous materials with fibre–fibre interface barriers. *Modelling and Simulation in Materials Science and Engineering*, 16(3) (2008) 035007.

[143] F. Battocchio, M. P. F. Sutcliffe, Modelling fibre laydown and web uniformity in nonwoven fabric. *Modelling and Simulation in Materials Science and Engineering*, 25(3) (2017) 035006.

[144] https://www.boost.org/doc/libs/1_65_1/libs/numeric/odeint/doc/html/index.html

[145] G. G. Dahlquist, A special stability problem for linear multistep methods. *BIT Numerical Mathematics*, 3(1) (1963) 27-43.

[146] https://www.mathworks.com/company/newsletters/articles/stiff-differential-equations.html

[147] T. Chen, X. Huang, Air drawing of polymers in the melt blowing nonwoven process: mathematical modelling. *Modelling and Simulation in Materials Science and Engineering*, 12(3) (2004) 381.

[148] F. Croisier, A. S. Duwez, C. Jérôme, A. F. Léonard, K. O. Van Der Werf, P. J. Dijkstra, M. L. Bennink, Mechanical testing of electrospun PCL fibers. *Acta Biomaterialia*, 8(1) (2012) 218-224.

[149] X. Li, F. Bian, J. Lin, Y. Zeng, Effect of electric field on the morphology and mechanical properties of electrospun fibers. *RSC Advances*, 6(56) (2016) 50666-50672.

[150] S. Ramakrishna, An introduction to electrospinning and nanofibers. World Scientific (2005).

[151] C. Drew, X. Wang, L. A. Samuelson, J. Kumar, The effect of viscosity and filler on electrospun fiber morphology. *Journal of Macromolecular Science, Part A*, *40*(12) (2003) 1415-1422.

[152] H. Y. Jian, S. V. Fridrikh, G. C. Rutledge, The role of elasticity in the formation of electrospun fibers, *Polymer* 47(13) (2006) 4789-4797.

[153] K. Nartetamrongsutt, G. G. Chase, The influence of salt and solvent concentrations on electrospun polyvinylpyrrolidone fiber diameters and bead formation, *Polymer 54*(8) (2013) 2166-2173.

[154] E. Ewaldz, R. Patel, M. Banerjee, B. K. Brettmann, Material selection in electrospinning microparticles, *Polymer* 153 (2018) 529-537.

[155] T. Lin, H. Wang, H. Wang, X. Wang, The charge effect of cationic surfactants on the elimination of fibre beads in the electrospinning of polystyrene, *Nanotechnology 15*(9) (2004) 1375-1381.

[156] M. Wang, H. Singh, T. A. Hatton, G. C. Rutledge, Field responsive superparamagnetic composite nanofibers by electrospinning, *Polymer 45* (2004) 5505-5514.

[157] S. Kedem, J. Schmidt, Y. Paz, Y. Cohen, Composite polymer nanofibers with carbon nanotubes and titanium dioxide particles, *Langmuir 21* (2005) 5600-5604.

[158] A. Jaworek, A. Krupa, M. Lackowski, A. T. Sobczyk, T. Czech, S. Ramakrishna, S. Sundarrajan, D. Pliszka, Nanocomposite fabric formation by electrospinning and electrospraying technologies. *Journal of Electrostatics*, *67*(2-3) (2009) 435-438.

[159] H. Bae, J. Lee, Assembly of particle-fiber composites by electrohydrodynamic jetting using counter-charged nozzles: Independent release control. *Journal of Industrial and Engineering Chemistry*, *40* (2016) 99-105.

[160] V. N. Chamundeswari, Y. J. Chuah, S. C. J. Loo, Multidrug-eluting bi-layered microparticle-mesh scaffolds for musculoskeletal tissue regeneration. *Journal of Materials Chemistry B*, *6*(20) (2018) 3340-3347.

[161] V. Kadam, I. L. Kyratzis, Y. B. Truong, J. Schutz, L. Wang, R. Padhye, Electrospun bilayer nanomembrane with hierarchical placement of bead-on-string and fibers for low resistance respiratory air filtration. *Separation and Purification Technology*, 224 (2019) 247-254.

[162] H. Attia, D. J. Johnson, C. J. Wright, N. Hilal, Robust superhydrophobic electrospun membrane fabricated by combination of electrospinning and electrospraying techniques for air gap membrane distillation, *Desalination* 446 (2018) 70–82.

[163] V. P. Schulz, J. Becker, A. Wiegmann, P. P. Mukherjee, C. Y. Wang, Modeling of two-phase behavior in the gas diffusion medium of PEFCs via full morphology approach. *Journal of the Electrochemical Society*, 154(4) (2007) 419-426.

[164] A. Ashari, T. M. Bucher, H. V. Tafreshi, M. A. Tahir, M. S. A. Rahman, Modeling fluid spread in thin fibrous sheets: Effects of fiber orientation. *International Journal of Heat and Mass Transfer*, 53(9-10) (2010) 1750-1758.

[165] M. A. Tahir, H. V. Tafreshi, S. A. Hosseini, B. Pourdeyhimi, Modeling the role of microstructural parameters in radiative heat transfer through disordered fibrous media. *International Journal of Heat and Mass Transfer*, 53(21-22) (2010) 4629-4637.

[166] X. Hou, M. Acar, V. V. Silberschmidt, Finite element simulation of low-density thermally bonded nonwoven materials: Effects of orientation distribution function and arrangement of bond points. *Computational Materials Science*, 50(4) (2011) 1292-1298.

[167] B. Sabuncuoglu, M. Acar, V. V. Silberschmidt, Finite element modelling of fibrous networks: Analysis of strain distribution in fibres under tensile load. *Computational Materials Science*, 79 (2013) 143-158.

[168] A. M. Saleh, H. V. Tafreshi, B. Pourdeyhimi, An analytical approach to predict pressure drop and collection efficiency of dust-load pleated filters. *Separation and Purification Technology*, 161 (2016) 80-87.

[169] Y. Doganoglu, V. Jog, K. V. Thambimuthu, R. Clift, Removal of fine particles from gases in fluidized beds. *TRANSACTIONS OF THE INSTITUTION OF CHEMICAL ENGINEERS*, *56*(4) (1978) 239-248.

[170] C. Tien, (2012). *Principles of filtration*. Elsevier.

[171] I. B. Stechkina, Diffusion precipitation of aerosols in fiber filters, Dokl. Acad. Nauk. SSSR 167 (1966) 1327.

[172] K. W. Lee, B. Y. H. Liu, Theoretical study of aerosol filtration by fibrous filters. *Aerosol Science and Technology*, *1*(2) (1982) 147-161.

[173] R. C. Brown, Air filtration, Pergamon Press, New York, (1993).

[174] F. A. L. Dullien, Porous media fluid transport and pore structure, 2nd.,Academic Press, Inc., San Diego, California, USA, (1992).

[175] F. Nicot, H. Xiong, A. Wautier, J. Lerbet, F. Darve, Force chain collapse as grain column buckling in granular materials. *Granular Matter*, *19*(2) (2017) 18.

[176] A. Sufian, A. R. Russell, A. J. Whittle, Anisotropy of contact networks in granular media and its influence on mobilised internal friction. *Géotechnique*, *67*(12) (2017) 1067-1080.

[177] A. L. Hiddessen, D. A. Weitz, D. A. Hammer, Rheology of binary colloidal structures assembled via specific biological cross-linking. *Langmuir*, 20(16) (2004) 6788-6795.

[178] A. B. Hopkins, Y. Jiao, F. H. Stillinger, S. Torquato, Phase diagram and structural diversity of the densest binary sphere packings. *Physical Review Letters*, 107(12) (2011) 125501.

[179] A. R. Kansal, S. Torquato, F. H. Stillinger, Computer generation of dense polydisperse sphere packings. *The Journal of Chemical Physics*, 117(18) (2002) 8212-8218.

[180] E. Santiso, E. A. Müller, Dense packing of binary and polydisperse hard spheres. *Molecular Physics*, 100(15) (2002) 2461-2469.

[181] A. Donev, I. Cisse, D. Sachs, E. A. Variano, F. H. Stillinger, R. Connelly, S. Torquato, P. M. Chaikin, Improving the density of jammed disordered packings using ellipsoids. *Science*, 303(5660)

(2004) 990-993.

[182] A. V. Kyrylyuk, A. Wouterse, A. P. Philipse, Random Packings Of Rod-Sphere Mixtures Simulated By Mechanical Contraction. *In AIP Conference Proceedings* 1145(1) (2009) 211-214.

[183] J. Zhao, S. Li, R. Zou, A. Yu, Dense random packings of spherocylinders. *Soft Matter*, 8(4) (2012) 1003-1009.

[184] R. Caulkin, A. Ahmad, M. Fairweather, X. Jia, R. A. Williams, Digital predictions of complex cylinder packed columns. *Computers & Chemical Engineering*, 33(1) (2009) 10-21.

[185] Y. Jiao, S. Torquato, Maximally random jammed packings of Platonic solids: Hyperuniform long-range correlations and isostaticity. *Physical Review E*, 84(4) (2011) 041309.

[186] L. Meng, P. Lu, S. Li, J. Zhao, T. Li, Shape and size effects on the packing density of binary spherocylinders. *Powder Technology*, 228 (2012) 284-294.

[187] A. Baule, R. Mari, L. Bo, L. Portal, H. A. Makse, Mean-field theory of random close packings of axisymmetric particles. *Nature Communications*, 4 (2013) 2194.

## Appendix A: Vita

Sina H. Yousefi
Phone: +1(323)-354-9627 | Email: hassanpouryos@vcu.edu
LinkedIn: http://www.linkedin.com/in/sina-yousefi/

Education

PhD, Mechanical Engineering,
*Virginia Commonwealth University (VCU)*, Richmond, VA **December 2019**

- **Dissertation**: Modeling electrospun fibrous materials
- **Advisor:** Dr. Houman V. Tafreshi

MSc, Mechanical Engineering,
*Iran University of Science and Technology (IUST)*, Tehran, Iran **January 2015**

- **Dissertation**: Analytical modelling of flame propagation
- **Advisor:** Dr. Mehdi Bidabadi

BSc, Mechanical Engineering,
*K. N. Toosi University of Technology (KNTU)*, Tehran, Iran **August 2012**

- **Dissertation**: Optimization of PEMFC-TEC cogeneration plant
- **Advisor:** Dr. Farschad Torabi

RESEARCH INTEREST

- Numerical and experimental investigation of electrospinning.
- Fluid heat and particle transport through porous media and fibrous structure.
- Separation and filtration science.
- Liquid absorption and Porous media
- Modeling interfacial phenomena and superhydrophobicity.

PUBLICATIONS

**Journals**

1. **S. H. Yousefi**, H.V. Tafreshi, Modeling Electrospun Fibrous Structures with Embedded Spacer Particles: Application to Aerosol Filtration, ”Separation and Purification Technology”, (2019)
2. **S. H. Yousefi**, D. G. Venkateshan, C. Tang, H. V. Tafreshi, B. Pourdeyhimi, Effect of Electrospinning Conditions on Microstructural Properties of PS Fibrous Materials, ”Journal of Applied Physics”, (2019)
3. **S. H. Yousefi**, C. Tang, H. V. Tafreshi, B. Pourdeyhimi, Empirical Model to Simulate Morphology of Electrospun PCL Mats, ”Journal of Applied Polymer Science”, (2019)
4. Moghadam, **S. H. Yousefi**, H. V. Tafreshi, B. Pourdeyhimi, Characterizing Nonwoven Materials via Realistic Microstructural Modeling, ”Separation and Purification Technology”, (2018)
5. M. Bidabadi, **S. H. Yousefi**, A. Khoini Poorfar, M. Hajilou, S. Zadsirjan, Modelling Combustion of Magnesium Dust Cloud in Heterogeneous Media, ”Combustion Explosion and Shock Waves”, (2014)
6. M. Bidabadi, M. Hajilou, A. Khoini Poorfar, **S. H. Yousefi**, S. Zadsirjan,, Modeling Flame Propagation of Micron-sized Iron Dust Particles in Media with Spatially Discrete Sources, ”Fire Safety Journal”,(2014)

**Conferences**

1. **S. H. Yousefi**, H.V. Tafreshi, B. Pourdeyhimi, Effect of electrospinning Conditions on Microstructural Properties of Fibrous Materials, "American Filtration & Separations Society (AFS)", Cherry Hill, NJ, (2019)
2. A. H. Haddadi, A. Ghomian, **S. H. Yousefi**, F. Torabi, Thermoeconomic and Exergetic Analysis of a PEMFC-TEC Cogeneration Plant based on Organic Rankin Cycle, "ISME 2013", (2013)
3. A. H. Haddadi, A. Ghomian, **S. H. Yousefi**, F. Torabi, Design and Thermoeconomic Analysis of a PEMFC-TEC Cogeneration Plant, "The 2nd Conference on Hydrogen and Fuel Cell", (2012)

**Posters**

1. **S. H. Yousefi**, H.V. Tafreshi, B. Pourdeyhimi, The First Predictive Theory to Estimate the Thickness and Porosity of Nanofiber Mats, "IDEA", Boston, MA, (2016)
2. D.G Venkateshan, **S. H. Yousefi**, M.A. Tahir, H.V. Tafreshi, B. Pourdeyhimi, Influence of Fiber Rigidity During Deposition on the Characteristics of Electrospun Mats, "Nanofibers, Applications and Related Technologies (NART)", Raleigh, NC, (2016)

---

RESEARCH / WORK EXPERIENCE

Graduate Research Assistant,

*Virginia Commonwealth University*, Richmond, VA **January 2016 – Present**

- Developed a first ever predictive models to characterize fibrous materials, resulting in over 90% validation accuracy with experimental results (C++ and Python programming).
- Simulated the most realistic 3-D structure of nanofibers by developing an in-house C++ computer program in a fibrous filter media (electrospun polymer mats).
- Evaluated filtration performance and nonwoven polymer mat specifications (95% accuracy) via novel design of calibrated experiment approaches.
- Introduced the realistic model of fibrous media which helped for particle filtration and droplet separation via computer simulation, analytical formulation, and experimental set up.
- Conducted and evaluated the simulated polymer nanocomposites in lab set-up and proved simulation and real result match.
- Established a more efficient CPU time computational methods in comparison with previous works via Python to model the electrospinning jet flow.
- Published 4 of original works in peer-reviewed journals and delivered 3 presentations at scientific conferences. Selected by American Filtration Society (AFS) for poster competition at FiltCon 2019.

Researcher,

*NWI - The Nonwoven Institute*, Raleigh, NC **January 2016 – November 2017**

- Innovated research on creating accurate representations of fibrous materials for an industry-sponsored project through the Nonwoven Institute at NC State University, Raleigh, NC.
- Expressed computational/experimental results such as thickness and porosity of fibrous structure in the form of easy-to-use modules for filtration industry (C++, MATLAB and Python programming).
- Presented 4 technical presentation to groups of 150+ technical specialists and managers of filtration and nonwoven industries on a semi-annual meeting basics over a 2-years period.

Senior Mechanical Engineer,

*Luman Sanaat Company*, Tehran **May 2015 – December 2015**

- Removed 65% of the suspended solids, resulting in a 5% improvement in efficiency with redesigning and troubleshooting of wastewater treatment systems.
- Reduced package construction costs totaling 30% in wastewater treatment processes by optimizing and refining documentation system via SolidWorks in EPC (Engineering, Procurement and Construction) project.
- Created mechanical design calculations, P&ID, PFD, and engineering documents for EPC project that include technical specification, mechanical design engineering, installation and detail engineering product design (3D CAD prototype).
- Led selection, manufacturing, and technical evaluation, and installation of rotary machines in EPC projects.
- Developed wastewater package and inspection testing design package to the plant.

Graduate Research Assistant,

*IUST*, Tehran **September 2012 – January 2015**

- Developed a MATLAB code to simulate flame propagation.
- Implemented theoretical research of dust clouds including discrete and random combustion that enabled to predict the flame propagation in different media.
- Scientific research and collaboration resulted in publishing 3 peer-reviewed publications as a master student.

Research and Development Engineer (R&D),

*RAL Offshore*, Tehran **January 2013 – December 2013**

- Calculated the buckling analysis of mechanical support equipment of pipeline via MathCad.
- Improved time efficiency (30% faster) of sizing pipeline in EPC Project via fluid flow simulation.
- Converted stress analysis knowledge to applicable program and mechanical documentation for company.

## TECHNICAL SKILLS

- **Simulation Tools:** SolidWorks (CSWA certificate), AutoCAD, Catia, Ansys, Piping Systems Fluid Flow.
- **Programming:** MATLAB, Python, C/C++, Fortran, Mathematica, Engineering Equation Solver (EES).
- **Experimental:** Nonwoven Fabrication, SEM, Electrospinning, Nonwoven Porosity Measuring.
- **General Skills:** LaTeX, MS Office, Corel Draw, Tecplot, Linux

## SELECTED HONORS AND AWARDS

- School of Engineering Dissertation Fellowship Award, fall 2019, VCU, Richmond, VA.
- 3rd place student poster competition, American Filtration and Separation Society, Annual Conference, May 9-12 2019, Philadelphia, NJ.